Study of newly discovered two dimensional cobalt based perovskite compounds doped with various rare earth elements

Qi Wen Yao
University of Wollongong

Study of newly discovered two dimensional cobalt based perovskite compounds doped with various rare earth elements

A thesis submitted in fulfillment of the requirement for the award of the degree

Doctor of Philosophy (PhD)

from

University of Wollongong

by

Qi Wen Yao,

B.S. (UNSW)

M.E. (Mat. Eng. UOW)

Institute for Superconducting and Electronic Materials

Faculty of Engineering

2008

Declaration

I, Qi Wen Yao, declare that this thesis, submitted in fulfilment of the requirements for the award of Doctor of Philosophy, in the Institute for Superconducting and Electronic Materials, in the Faculty of Engineering, University of Wollongong, is wholly original work unless otherwise referenced or acknowledged. This thesis has not been submitted for qualifications at any other academic institution.

Qi Wen Yao

Wollongong

November 2008

ACKNOWLEDGMENTS

I would like to express my gratitude towards my supervisor, Professor Xiao Lin Wang, for his enormous help and the effort that he devoted to teaching me and helping me to gain knowledge of this field in my years of study and research at the University of Wollongong. I would also like to thank my co-supervisors, Professor Shi Xue Dou and Dr. Zhenxiang Cheng, for their important help with my research.

I also want to thank Dr. Germans Peleckis and Mr. Dapeng Chen for their helpful advice and discussions on my thesis. Finally, I would like to thank Dr. Tania Silver for her careful editing work on my thesis.

ABSTRACT

This thesis focuses on the study of a newly discovered two-dimensional CoO_2 layer structured peroskite compound, Sr_2CoO_4. To explore doping effects on the physical properties of the new compound, a systematic and detailed experimental study has been carried out, relating to the aspects of synthesis, structure, transport and magneto-transport behaviour, magnetism, and dielectricity. Theoretical investigations have also been carried out for both crystal and electronic band structures, using Rietveld refinement and first-principles band structure calculations.

Various rare earth element doped Sr_2CoO_4 polycrystalline compounds ($Sr_{2-x}RE_xCoO_4$, where x = 0.25 – 1.5 and RE = Pr, La, Gd, Eu, and Nd) were studied systematically. It has been found that the size and valence, as well as the doping level of the rare elements, control the physical properties of the Sr_2CoO_4. Ferromagnetic behaviour is found to exist in some of the doped compounds and to have interesting properties. It was observed that the lattice parameter *a* reminds relatively stable, with values around 3.7 to 3.8 Å for x = 1 for various RE doped compounds of $Sr_{2-x}RE_xCoO_4$. The Co-O(2) in-plane bond lengths were also not sensitive to different RE dopants for the x = 1 doping level. In contrast, lattice parameter *c,* as well as the out-of-plane bond length Co-O(1), varies with different RE dopants in the compound for the doping level of x = 1, and consequently, the unit cell volume also changes, depending on the RE dopant. It was found that Sr_2CoO_4 is the most tolerant to Pr as a dopant. For x values from 0.5 to 1.5, single phase Sr_2CoO_4 structured samples were achieved. La doping was compatible with single phase compounds for x = 1 – 1.25, and for Eu doping, single phase compounds

were formed for x = 0.75 – 1. For both Gd and Nd doping, near single phases are formed for all the tested x values (x = 0.5 – 1.25),

Our results show that some of the Pr-doped and La-doped single phase samples have large coercive fields, and hence, they have good potential industrial applications (permanent magnets in electric motors, magnetic recording media, etc.), while Eu-doped samples can have high magnetoresistance (MR) values, making the Eu-doped compound a good candidate for application as a colossal magnetic resistance (CMR) material.

For the Pr-doped $Sr_{2-x}Pr_xCoO_4$, the lattice parameter *c* decreased with the Pr doping level x. The Curie temperature (T_C) was found to be 200 K for $Sr_{1.5}Pr_{0.5}CoO_4$. The resistivities were found to increase with doping level x. A large coercive field of about 1 Tesla (T) was found for the sample with x = 0.75. The values of the dielectric constant (ε) were over 2000 at low frequencies of less than 1 kHz (not shown here) and gradually decreased with increasing frequencies. The ε of the x = 1 sample is greater than that of the x = 0.75 sample, indicating that the charge induced capacitance in the x = 1 sample is greater than that of the x = 0.75 sample. This is in agreement with the trend of their resistivity measurements.

For the Eu-doped compounds of Sr_2CoO_4, single 214 phase was achieved for x = 0.75 - 1. The lattice parameter *c* decreased with the Eu doping level. The Curie temperatures were found to be around 160-200 K for samples with x = 0.75 and 1. An antiferromagnetic transition is observed at 35 K for the x = 0.75 sample. Magnetic

semiconductor characteristics were observed for all the Eu-doped samples. The existence of unusually high magnetoresistance in these compounds makes them stands out from the rest of the RE doped compounds in this regard. For example, the sample with x = 1.25 showed a MR value of about 46% at 8 Tesla at 100 K.

For the La-doped Sr_2CoO_4 compounds, the temperature dependence of the resistivity shows a semiconductor-like behavior over a wide range of temperatures, a metal-insulator transition at 240 K, and an upturn at 160 K for the x =1 , 1.25, and 0.75 samples. The coercive field was about 1 T for the sample with x = 0.75, while it is about 0.05 T for the x = 0.75 and 0.1 T for the x = 1.25 sample. A negative field hysteresis in the magnetoresistance in close correlation with the coercive field has been observed and can be explained by the grain boundary tunneling effect. First-principles band structure calculations were carried out for $Sr_{1.5}La_{0.5}CoO_4$, and the results indicate that the system is metallic, with a high spin polarization which is responsible for the observed large magnetoresistance. The phonon density of states (PDOS) reveals that the Co 3d electrons and planar oxygen electrons are responsible for the high spin polarization at the Fermi surface in the compound.

The Gd-doped Sr_2CoO_4 compounds were found to be paramagnetic semiconductors with MR values of only around 3 to 5%. Their transport properties can be described by the hopping model for semiconductors. Band structure calculations indicate that the spin polarization is high in the Gd-doped Sr_2CoO_4.

Nd-doped compounds were found to be ferromagnetic semiconductors at temperatures of about 250 and 170 K for the x = 1 and 0.75 samples, respectively. Their MR valves were about 5 %, similar to those of the Gd-doped samples. The Nd doping raised the Curie temperature of Sr_2CoO_4, so that it reached 210 K for doping with Nd at levels up to x = 0.5.

Table of Contents

List of Figures

List of Tables

INTRODUCTION

Spintronics or spin electronics is a new emerging research field. It involves the study of the active control and manipulation of spin degrees of freedom in solid-state systems. Apart from adding an extra degree of freedom for controlling material properties compared to conventional charge based solid-state systems, control of spin polarization, spin dynamics, and spin-polarized transport in semiconductor-like materials differs from control of charge transport in that spin is a non-conserved quantity in solids due to spin-orbit and hyperfine coupling. As a result, spintronics provides much more complexity, as well as raising issues of considerable interest to the research community. Spintronic research in recent years has in fact attracted considerable attention from researchers around the world [1-26]. Over the past few decades, the restless exponential growth of the amount of information that can be processed, stored, and transferred per unit time per unit area of spintronic relevant devices can be clearly seen. The rapid development of spin electronics has its roots in the conviction that the progress that is being achieved by miniaturization of active elements (transistors and memory cells) cannot continue without limit. Therefore, the invention of new information technologies is needed, and that requires new ideas concerning the design of both devices and system architecture. The main goal of spintronics is to gain knowledge on spin dependent materials (hence spin dependent devices) and to exploit them for new functionalities for practical applications. One major concern has been that the magnetic fields present in the ambient environment are significantly weaker than the electric fields. Just because of this very reason, magnetic memories are non-volatile, while memories based on accumulated electric charge (dynamic random access memory, known as DRAM) require frequent refreshing. The current research on spintronics involves virtually all material families, the most studied and consequently the most mature area being the magnetic metal multi-

layers, in which spin-dependent scattering and tunneling are being successfully applied in practical use. As a result, the reading heads of high-density hard disks and magnetic random access memories (MRAM) have experienced rapid progress in recent years. However, in the context of spintronics, particularly promising advances relate to ferromagnetic semiconductors, which combine complementary functionalities of ferromagnetic and semiconductor material systems, but much further study is required before they are suitable for more advanced applications.

Finding novel ferromagnetic materials showing negative magnetoresistance and studies of polarized spin dependent tunneling magnetoresistance are hot topics within spintronics[1,2]. So far, several magnetoresistance (MR) oxide systems have been found and extensively investigated: 1).The perovskite ferromagnetic manganites in the form of $RE_{1-x}A_xMnO_3$, with RE standing for a rare earth and A for a divalent ion such as Ca, Sr, or Ba, exhibit the well known type of colossal magnetoresistance (CMR) in fields of several Tesla[3]. 2). Pyrochlore type $Tl_2Mn_2O_7$ shows large MR near the Curie temperature of 140 K[4]. The double-perovskite ferromagnets Sr_2FeMoO_6 and Sr_2FeReO_6 exhibit large low-field MR below their high Curie temperatures, T_C, of about 400 K[5]. MR is also present in simple oxides, such as CrO_2 and Fe_3O_4. CrO_2 crystallizes in the rutile structure and exhibits giant tunneling MR at low temperatures[6]. Fe_3O_4 is a good candidate for room temperature device applications[7] because it has a very high T_C of 858 K. Analogous to the perovskite manganites, giant magnetoresistance is also observed in the cobalt based perovskite compounds, $RE_{1-x}A_xCoO_3$[8,9], as well as in oxygen deficient $LnBaCo_2O_5$ (Ln = Eu and Gd) compounds[10]. When the dimensionality is reduced from three to two dimensions, the MnO_2 or CoO_2 network is confined to the *ab*-plane. Spin-related property changes are also expected, and their correlation with anisotropy is of great interest. Layered perovskite manganites, defined

as the Ruddlesden-Popper family of compounds, $(RE,A)_{n+1}Mn_nO_{3n+1}$, consist of n layers of MnO_6 octahedra separated by n layers of REO_2[11].

[1]See for instance: MRS Bulletin, October 2003; .M. Ziese and M.J. Thornton (eds.), Spin Electronics (Heidelberg: Springer, 2001).

[2]M. Ziese, Rep. Prog. Phys., 65 (2002) 143.

[3]R. von Helmont, J. Wecker, B. Holzapfel, L. Schultz, K. Samwer, Phys. Rev. Lett., 71 (1993) 2331.

[4]Y. Shimakawa, Y. Kubo, T. Manako, Nature 379 (1996) 53.

[5]K.-I.Kobayashi, T. Kimura, H. Sawada, K. Terakura, Y. Tokura, Nature 395(1998) 677.

[6]H.Y. Hwang and S.-W. Cheong, Science 278 (1997) 1607.

[7]R.A. de Groot et al., Phys. Rev. Lett., 50 (1983) 2024.

[8]G. Briceno, H. Chang, X.D. Sun, P. G. Schultz, X.-D. Xiang, Science 270 (1995) 273.

[9]I.O. Troyanchuk, N. V. Kasper, D. D. Khalyavin, H. Szymczak, R. Szymczak, M. Baran, Phys. Rev. Lett., 80 (1998) 3380.

[10]C. Martin, A. Maignan, D. Pelloquin, N. Nguyen, B. Raveau, Appl. Phys. Lett., 71 (1997) 1421.

[11]Y. Moritomo, A. Asamitsu, H. Kuwahara, Y. Tokura , Nature 380 (1996) 141.

[12]J. Matsuno Y. Okimoto, Z. Fang, X. Z. Yu, Y. Matsui, N. Nagaosa, M. Kawasaki, Y. Tokura, Phys. Rev. Lett., 93 (2004) 167202.

[13]X.L.Wang and E. Takayama-Muromauchi, Phys. Rev. B., 72 (2005) 064401.

[14]K.W. Lee and W.E. Pickett, Phys. Rev. B 73 (2006) 174428.

Compounds with the K_2NiF_4-typ structure are a frequently studied topic in spintronics [27-31]. Such compounds are well known to exhibit various intriguing physical phenomena, such as high-temperature superconductivity in cuprates, spin-triplet superconductivity in ruthenates, and spin/charge stripes in nickelates and manganites. The discovery of superconductivity in $Na_xCoO_2*H_2O$ [32] has generated great interest in the study of two-dimensional (2D) CoO_2 layer structured compounds. Fig. 1.1 shows a structural view, indicating how K. Takada et al. turned $Na_{0.7}CoO_2$ compound into a superconducting compound, $Na_xCoO_2 \cdot yH_2O$, with a critical temperature, T_c, of about 5 K, through a chemical oxidation process. This result was published in Nature in 2003 [32].

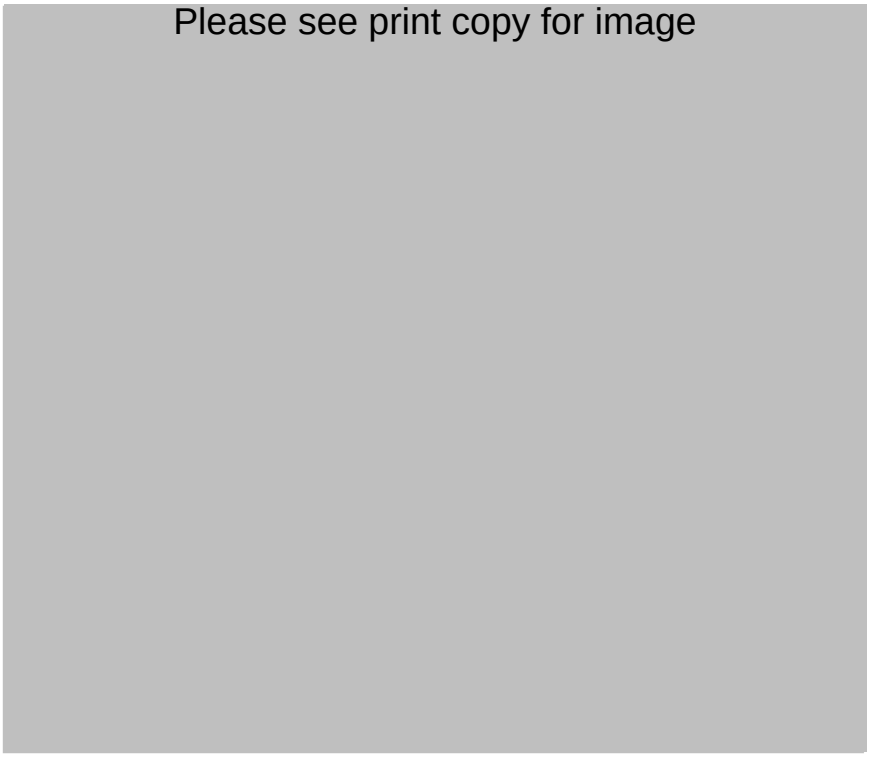

Fig. 1 Structural views of $Na_{0.7}CoO_2$ (left) and $NaxCoO_2 \cdot yH_2O$ (right) [32].

Note: In Fig. 1.1, Na and H_2O sites are partially occupied. $Na_{0.7}CoO_2$ was prepared from Na_2CO_3 (99.99%) and Co_3O_4 (99.9%) by solid-state reaction at 800 ^oC for 8 h under oxygen gas flow. A fivefold excess of Br_2 regarding the Na content was dissolved in acetonitrile (CH_3CN). A well pulverized powder of $Na_{0.7}CoO_2$ was immersed in the Br_2/CH_3CN solution for 5 days to deintercalate Na^+ ions; then the product was filtered, washed with CH_3CN and distilled water, and finally dried in an ambient atmosphere. No impurities were detected by energy dispersive X-ray analysis (ED).

Very recently, metallic ferromagnetism with a Curie temperature T_C of 250-255 K has been discovered in the K_2NiF_4 type two-dimensional layered perovskite Sr_2CoO_4 in the form of single crystalline films fabricated by pulsed laser deposition (PLD)[12] and bulks produced by a high pressure and high temperature technique[13]. A metal insulator transition with large negative MR values was observed in the vicinity of T_C. The MR increases at low temperatures and reaches a maximum at the coercive field H_c[12,13]. Y^{3+} doping into Sr^{2+} gradually changes the Sr_2CoO_4 compound from a ferromagnetic metal to an antiferromagnetic semiconductor[13]. Band structure calculations by Lee and Pickett[14] revealed that the Sr_2CoO_4 can be either a ferromagnetic metal for the thin film samples or a half metal for the high pressure phase samples. They pointed out that the newly discovered Sr_2CoO_4, in the forms of bulks fabricated by the high pressure technique and thin films made by pulsed laser deposition (PLD), introduces new transition metal oxide physics that may be useful in spin electronics devices[14]. In addition, it should be mentioned that the MR is only about -7.5 % at 7 T at 5 K for the high pressure phase Sr_2CoO_4[13] polycrystalline samples. It would be interesting to see how the physical properties, such as the MR values and Curie temperatures, as well as the electronic structures of the Sr_2CoO_4 family, can be changed or improved by doping

with other rare earth elements, in particular, with those having large magnetic moments or no magnetic moments.

K_2NiF_4-type Sr_2CoO_4 consists of CoO_2 planes separated by rock-salt-type SrO planes as shown in Fig. 1.2.

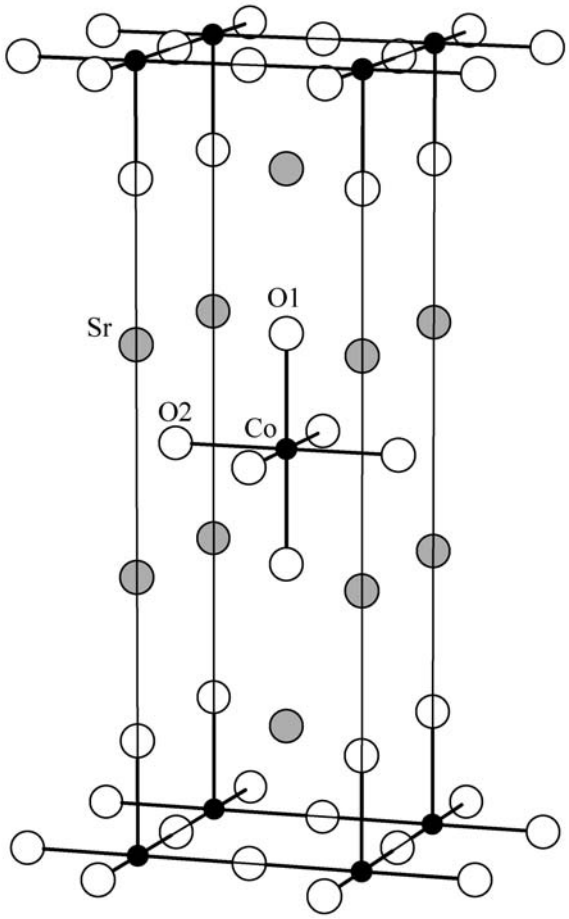

Fig. 2 Crystal structure of Sr_2CoO_4.

It has been reported that Sr_2CoO_4 single-crystalline thin films and polycrystalline samples are metallic ferromagnets with a fairly high Curie temperature (T_C) of 255 K, appreciable magnetic anisotropy, and quasi two-dimensional transport properties [1, 33]. It has been proposed that the CoO_2 layers can act as a stage for spintronic functionality as well as superconductivity [33]. The valence of the Co is 4+ in Sr_2CoO_4, which makes the CoO_2 layer very conductive in the same way as in the $SrCoO_3$ three-dimensional

(3D) perovskite compounds. When the Sr is totally replaced by rare earth elements (namely the rare earth based RE_2CoO_4 system), the compound still retains the K_2NiF_4 structure with 2D CoO_2 layers. In this case, the Co becomes 2+ and makes the system insulating or semiconducting, as well as paramagnetic. This has been reflected in studies of Y-doped $Sr_{2-y}Y_yCoO_4$ synthesized under high pressure [1] (see Fig. 1.3). The Y doping effect caused the T_C to decrease from 255 K for y = 0 to 150 K for y = 0.5, and ferromagnetism was not observed for $y \geq 0.67$ [1] (see Fig. 1.4). Large coercive fields were observed for these compounds (Fig. 1.5).

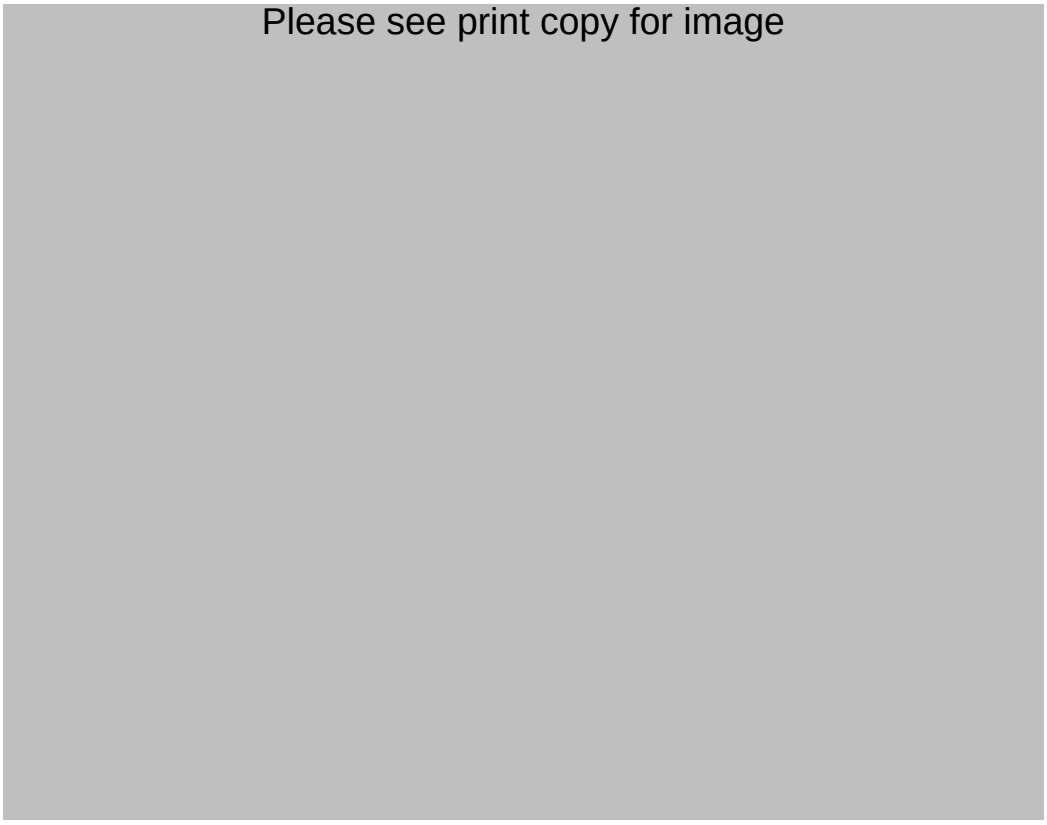

Fig. 3 Temperature dependence of the resistivity for the $Sr_{2-y}Y_yCoO_4$ system. Inset shows the activation energy, E_a (reproduced from [1]).

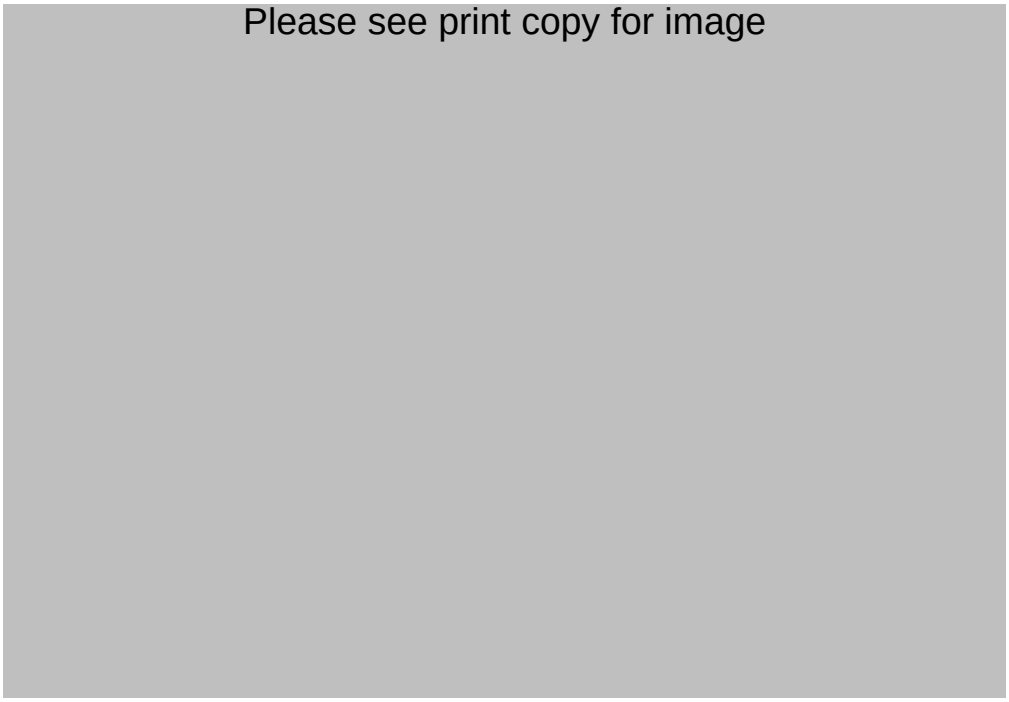

Fig. 4 Temperature dependence of the field cooled dc magnetization, measured at a magnetic field of 20 Oe (reproduced from [1]).

Compared with other types of K_2NiF_4-type compounds, polycrystalline Sr_2CoO_4 as a novel metallic ferromagnet has not been thoroughly studied to date when doped with rare earth elements. Only a few reports on thin films have been seen so far [1, 34, 90]. As mentioned earlier, ferromagnetic and semiconductor material systems have great potential in advanced material applications. We have found that when Sr_2CoO_4 polycrystalline compound is doped with rare earth ions, ferromagnetic semiconducting behaviour is often observed. It would be very useful to know how the physical properties of the layer structured K_2NiF_4-type polycrystalline Sr_2CoO_4 compounds can be changed, as well as be enhanced by rare earth element (RE) doping while maintaining an industrially achievable and economically practical method of sample fabrication.

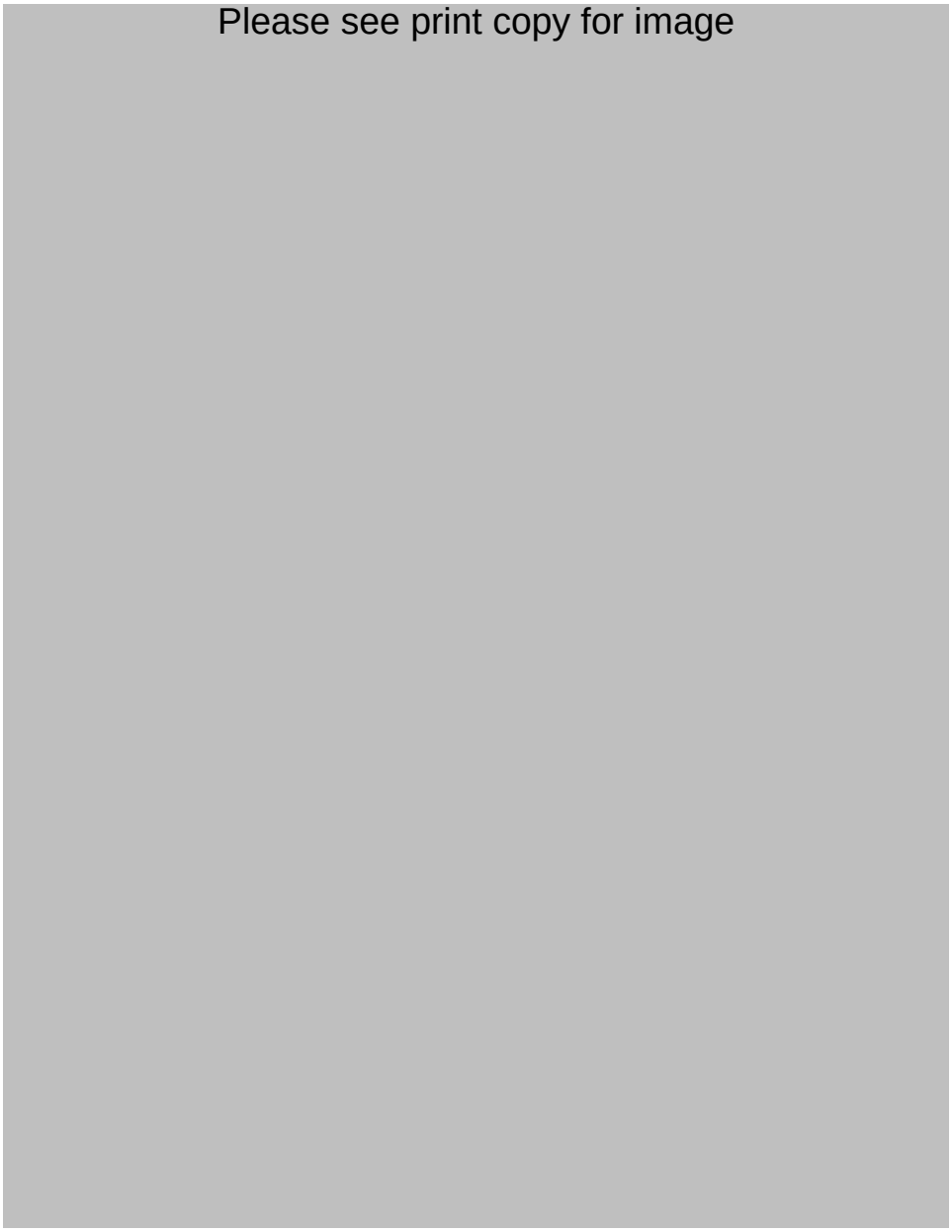

Fig. 5 Magnetic hysteresis loops for $Sr_{2-y}Y_yCoO_4$ (upper panel) and field-hysteretic magnetoresistance (lower panel) for Sr_2CoO_4 at 5 K (reproduced from [1]).

.

To achieve this, a series of RE doping studies, where RE = Pr, La, Eu, Gd and Nd, of Sr_2CoO_4 compound will be presented. The solid state reaction method was employed to make samples, as it is one of the most industrially practical methods of sample fabrications. The results will be presented, in detail, through individual discussions of the RE-doped Sr_2CoO_4 compounds.

The structure of the thesis is laid out to achieve the above-mentioned motivations/targets. In Chapter 1, some basic fundamentals theories and models that are applied in this study will be presented, and a brief relevant literature review on relevant research on the K_2NiF_4-type compounds from recent years will be provided.

In Chapter 2, sample fabrication and characterization will be discussed briefly, and the equipment used in the experiments will also be introduced. After this, the RE-doped sample studies will be presented, from Chapter 3 through Chapter 7, in the order of Pr, La, Eu, Gd, and Nd doping, and in Chapter 8, a brief summary for all these dopings will be provided.

In Chapter 3, we will see that the Pr-doped Sr_2CoO_4 polycrystalline compound presents very obvious ferromagnetic behaviour at various Pr doping levels. In Chapter 4, La doped Sr_2CoO_4 polycrystalline compound in this study will enable comparisons with known experimental results, and interesting typical ferromagnetic behaviour of the samples is also found. In Chapter 5, the Eu-doped Sr_2CoO_4 polycrystalline compound reveals a surprisingly high value of giant magnetoresistance (GMR) behaviour. In Chapters 6 and 7, a very interesting similarity is found between the Gd- and Nd-doped Sr_2CoO_4 polycrystalline compounds.

CHAPTER 1. FUNDAMENTALS AND LITERATURE REVIEW

1. 1 FUNDAMENTALS

1.1.1 Magnetic material category

In regards to magnetic behaviour, materials can be roughly categorised into five different types: Diamagnetic, paramagnetic, ferromagnetic, antiferromagnetic, and ferrimagnetic materials, as shown in Table 1.1.

Table 1. 1 Summary of different types of magnetic behaviour (Source: University of Birmingham website).

Material	Atomic magnetic behaviour	Material's magnetic behaviour	Examples /susceptibility
Diamagnetic	Atoms have no magnetic moment	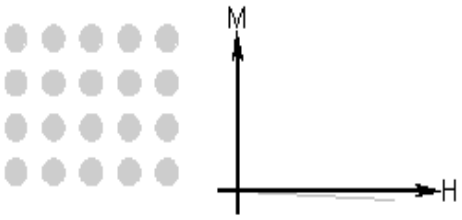	Au ($-2*10^{-6}$) Cu ($-1*10^{-6}$)
Paramagnetic	Atoms have randomly oriented magnetic moments	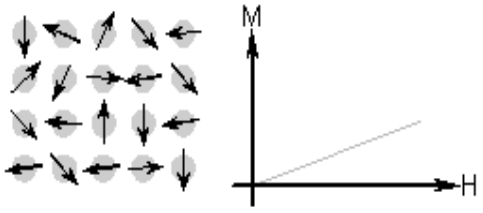	Pt ($21*10^{-6}$) Mn ($66*10^{-6}$)

Ferromagnetic	Atoms have parallel aligned magnetic moments	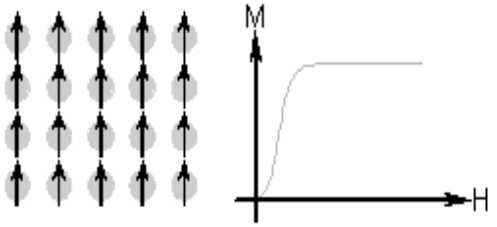	Fe (10^6)
Antiferromagnetic	Atoms have mixed parallel and anti-parallel aligned magnetic moments	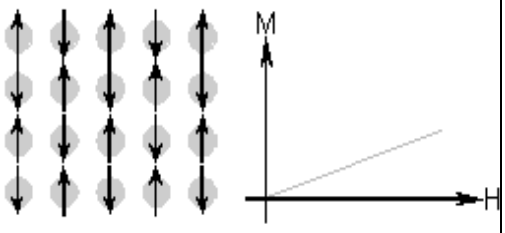	Cr ($3.6*10^{-6}$)
Ferrimagnetic	Atoms have anti-parallel aligned magnetic moments	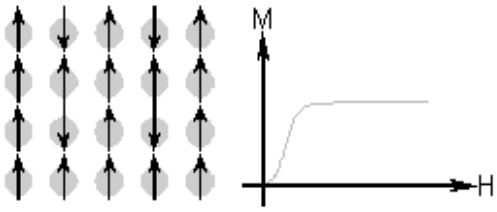	Ba ferrite (3)

From the intrinsic examples given in Table 1.1 (where an intrinsic material is a pure un-doped material), it is clearly seen that ferromagnetic materials have much higher susceptibilities compared to other types of materials. (In electromagnetism, the magnetic susceptibility is the degree of magnetization of a material in response to an applied magnetic field.) Magnetoresistance and magnetic hysteresis are two of the major aspects of magnetic (especially ferromagnetic) materials' properties that are relevant to applications. Magnetic materials are present in many areas of our modern life, from electric motors to computer disks, from road vehicles and consumer electronics to domestic appliances and credit cards. Their importance and complexity have resulted in

intensive research on magnetism, which, in turn, has led to greatly improved materials in recent decades [35]. Without a doubt, the two major aspects of magnetic materials that have attracted most of the research focus are colossal magnetoresistance effects (CMR) and the giant magneto-impedance (GMI) effects found in magnetic materials.

1.1.2 Colossal magnetoresistance (CMR)

Depending on the magnitude, large values of magnetoresistance are called either giant magnetoresistance(GMR) or colossal magnetoresistance(CMR). Colossal magnetoresistance (CMR) is a property of some materials, mostly manganese-based perovskite oxides, that enables them to dramatically change their electrical resistance in the presence of a DC magnetic field. The magnetoresistance of conventional materials enables changes in resistance of up to 5%, but materials featuring CMR may demonstrate resistance changes by orders of magnitude.

The CMR effect is characterized by its large numerical MR ratio, as well as its negative value and itsotropic nature (independent of field orientation) [36]. The magnetoresistance (MR) ratio is defined as:

$$MR = \frac{R(0) - R(H)}{R(H)} \qquad (1.1)$$

where R(0) is the material's resistance at zero magnetic field and R(H) is the resistance at an applied magnetic field H. This usually corresponds to more than a thousand-fold change in resistivity [37] for CMR materials. The MR ratio also can be expressed in terms of the fractional change to the zero field resistance as given by Von Helmholt [38,

39]:

$$MR = \frac{R(0) - R(H)}{R(0)} \qquad (1.2)$$

The MR effect has been of substantial importance technologically, especially in connection with read-out heads for magnetic disks and as sensors of magnetic fields. Until recently, however, there has not been much fundamental improvement of the performance of magnetoresistive materials since the work of W. Kelvin 150 years ago when he first found the MR effect [40, 41]. The general understanding in the 1980s was that it was not possible to significantly improve on the performance of magnetic sensors based on magnetoresistance. It was therefore a great surprise to researchers when in 1998 two research groups discovered the Giant Magnetoresistance (GMR) Effect independently. One group was led by Peter Grünberg [42], which used a trilayer system of Fe/Cr/Fe for their original experiment, and the other group, led by Albert Fert [43], used multilayers of the form $(Fe/Cr)_n$, where n could be as high as 60. Consequently, the 2007 Nobel Prize in physics was awarded to Albert Fert and Peter Grünberg for the discovery of GMR. Naturally, the discovery of GMR has led to a constantly increasing interest in magnetic material research for both basic science and applications [44-54].

1.1.3 Giant Magneto-impedance (GMI)

When a soft ferromagnetic conductor is subjected to a small alternating current (ac), a large change in the ac complex impedance of the conductor can be achieved upon applying a magnetic field. This is known as the Giant Magneto-impedance (GMI) effect.

The relative change of the impedance (Z) with applied field (H), which is defined as the giant magneto-impedance (GMI) effect, is expressed by

$$\Delta Z / Z(\%) = 100\% \times \frac{Z(H) - Z(H\max)}{Z(H\max)} \qquad (1.3)$$

where H_{max} is usually the external magnetic field sufficient to saturate the impedance. In practice, the value of H_{max} depends on the given conditions. Some researchers use H_{max} = 0 in Eq. (1.3), although this definition may not be appropriate, because the value of Z(0) depends on the remanent magnetic state of the material. Accordingly, the complex impedance,

$$Z = R + j\omega L \qquad (1.4)$$

where R and L are the resistance and the inductance, respectively.

By definition, the complex impedance Z for a uniform magnetic conductor is given by the ratio V_{ac}/I_{ac} where I_{ac} is the amplitude of a sinusoidal current $I = I_{ac}\exp(-j\omega t)$ passing through the conductor and V_{ac} is the voltage measured between the ends of the conductor. The inductance (or more accurately the self-inductance) in the imaginary part in Eq. 1.4 is given by the ratio of magnetic flux (ϕ) to ac current (i) passing through the conductor:

$$L = \frac{\Phi}{i} \qquad (1.5)$$

The magneto-impedance (MI) field dependence is related to the transverse permeability. As frequency increases, the current gets distributed near the surface of the conductor,

changing both the resistive and the inductive components of the total voltage V. The field dependence of the MI is dictated by the skin depth of the current:

$$\delta_s = \frac{c}{\sqrt{2\pi\varpi\sigma\mu}} \qquad (1.6)$$

where c is the velocity of light, σ the conductivity, and μ the permeability. (For nonmagnetic ordinary metals, μ = 1.)

Typical MI behaviour is such that it increases with frequency, attains a maximum at frequencies where the skin effect is strong ($\delta_s << a$, where *a* is a characteristic length scale, such as the wire radius or the thickness of a ribbon/film), and then decreases, since the permeability becomes insensitive to the field at sufficiently high frequencies.

The MI effect is usually weak and did not attract much attention in the past, until the early 1990s, when Panian and Mohri [55], and Beach and Berkowitz [56] reported a very large (giant) MI effect at relatively low frequencies in amorphous ferromagnetic FeCoSiB wires with small magnetic fields. Later, Machado [57] observed a smaller effect in $Fe_{4.6}Co_{70.4}Si_{15}B_{15}$ thin films, and Beach and Berkowitz [58] in ribbons.

Giant magneto-impedance (GMI) is a classical phenomenon that can be explained thoroughly on the basis of normal electromagnetic concepts [59-61].

1.1.4 Interlayer coupling

It has been a well known fact for a long time that disturbances such as defects and impurities in metallic systems can give rise to decaying oscillations of the electron density as a function of the distance from the disruption (known as Friedel or Ruderman-Kittel oscillations). In a similar way, a magnetic impurity atom in metallic surroundings gives rise to an induced spin polarization, and the disturbance will also decay in magnitude with distance (Fig. 1.1). If a second impurity is placed close to the first impurity, the magnetic moment of the second impurity will become aligned parallel or antiparallel to the first impurity, depending on the sign of the induced polarization for that particular distance.

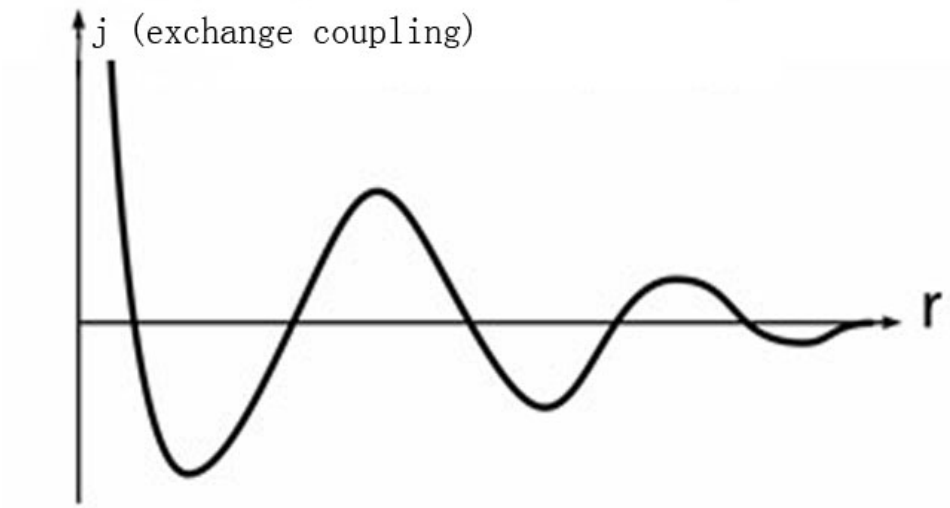

Fig.1. 1 Schematic illustration of the behaviour of the exchange coupling vs. distance.

Majkrzak et al. [62] reported (in 1986) in their work on a Gd/Y/Gd superlattice that antiparallel magnetic moment alignment between the Gd layers had been found for the case of 10 monolayers of Y. At the same time, Grünberg et al. [63] discovered an antiferromagnetic coupling between the iron layers for the Fe/Cr/Fe trilayer. This can be understood in a similar way to the Gd/Y/Gd example. It occurs where a ferromagnetic

Gd layer induces an oscillatory spin polarization of the normally non-magnetic Y metal and the second Gd layer happens to be at a distance where an antiferromagnetic alignment is preferred. Both of these examples show the important role of the electrons in the non-magnetic layer(s), that they provide the coupling mechanism between the magnetic layers. Naturally, many researchers then started to look at the dependence of the coupling on the thickness of the intermediate non-magnetic layers. A few groups had discovered a change of sign with increasing thickness [64-67]. Furthermore, Parkin [68] utilized the GMR effect as a tool to study the dependence of the oscillatory behaviour on the thickness of the non-magnetic layer and the dependence on the material of the non-magnetic layer, as well as on the dependence on the material of the magnetic layer itself. With Parkin's method, it was possible to prepare a large number of samples under comparable conditions. This work is regarded as important for the further development of the GMR effect into a working device [69-71].

1.1.5 Tunneling magnetoresistance

Julliere [72] first reported the Tunneling magnetoresistance (TMR) in a trilayer junction with the structure of Fe/amorphous Ge/Co. The experiments were done at low temperature and a TMR effect as high as 14% was reported. Fig. 1.2 shows an illustration of the TMR effect.

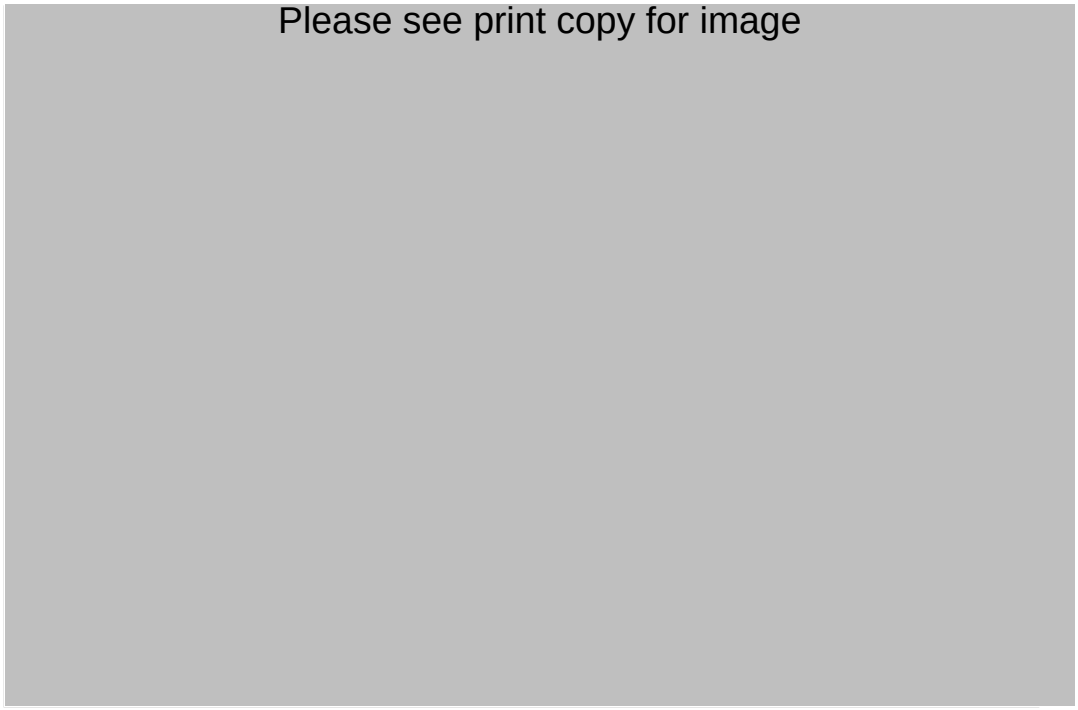

Fig.1. 2 Illustration of tunneling magnetoresistance (TMR). Two ferromagnetic layers separated by an insulating layer conduct a current i (reproduced from [41]).

Then the next work in this area was carried out by Maekawa [73], and the junction type investigated was Ni/NiO/FM (FM = Fe, Co or Ni). Both Julliere's and Maekawa's reports remained unnoticed for a long time. In fact it was only after the discovery by Fert and Grünberg of the GMR effect that attention was brought back to these types of systems again [74-79].

1.1.6. Ferromagnetism and its application

Ferromagnetic materials can be considered to be formed by microscopic magnetic regions in which many small dipoles (ions) are aligned, satisfying the demands of most of the electron bonds. However, the separate regions are aligned at random throughout the sample, making a very weak net magnetic field. These regions are called magnetic domains, and their behavior gives ferromagnetic materials their distinctive properties. If

some of the magnetic ions or dipoles are subtracted from the net magnetization (if they are partially anti-aligned), then the material is "ferrimagnetic". If the ions anti-align completely so as to have zero net magnetization, despite the magnetic ordering, then it is an antiferromagnet. All of these alignment effects only occur at temperatures below a certain critical temperature, called the Curie temperature (for ferromagnets and ferrimagnets) or the Néel temperature (for antiferromagnets). Above the Curie temperature, the thermal motion of the atoms in the material is so violent that the electrons in the bonds are no longer able to keep the dipole moments aligned. When this happens, the ferromagnetic material changes into a paramagnetic material with the usual weak magnetism.

If a ferromagnetic sample is placed in a magnetic field, the magnetic domains can be forced to 'rearrange' themselves into large domains aligned with the external field. When the external field is removed, the electrons in the bonds maintain the alignment, and the magnetism remains. This means that ferromagnetic materials can remember their past magnetic history - magnetic memory. This magnetic memory property is called magnetic hysteresis. Magnetic hysteresis is the basis and the soul for magnetic tapes and disk storage for computers.

The recording head of a tape recorder or the write head of a disk drive applies a field that magnetizes a small portion of the tape or disk, and the magnetism in each portion remains until another magnetic field changes it. When each magnetized section is moved under the playback head of a tape player, or the read head of a disk drive, the moving magnetic field induces small currents, which are amplified and turned into

either music or data bits. If the domains were unable to "remember" the field that had been applied to them, none of this would be possible.

1.1.7. Curie Weiss Law

The Curie-Weiss law is widely cited and applied in the ferromagnetic materials field. It describes the magnetic susceptibility of a ferromagnet in the paramagnetic region, above the Curie temperature, in this way:

$$\chi = C/(T-T_C) \qquad (1.7)$$

where: χ - is the magnetic susceptibility, which describes the degree of magnetization of a material in response to an applied magnetic field, C is a material-specific Curie constant T is absolute temperature, measured in kelvins, and T_C is the Curie temperature, measured in kelvins.

The susceptibility has a singularity at $T = T_C$. At this temperature and below there exists a spontaneous magnetization.

By re-ordering the Curie-Weiss equation, we can have:

$$\chi^{-1} = (1/C)T + (-T_C/C). \qquad (1.8)$$

As C and T_C are constants for a particular material, the relationship between χ^{-1} and T is linear.

1.1.8. Variable Range Hopping (VHR) - - the Mott Theory

Basis: when electronic states are localized near the Fermi level (EF), it is well known now that the electric conduction does not obey the classic process of diffusion, but follows the Variable Range Hopping (VRH) theory of Mott [80,81]. According to this theory, electrons are acting as if they are "intelligent", since in the conduction process they hop from an initial site " i " to another site " j " with an energy hop as low as possible. For such an energy, the site " j " is statistically located far from " i ", involving a distance r(i, j) = R which is generally much larger than the decay length of the wave function.

According to Mott, the conductivity σ in low temperature conduction in strongly disordered systems with localized states would have a characteristic temperature dependence of

$$\sigma = \sigma_0 \exp(-(T_o/T)^{1/4}) \qquad (1.9)$$

for three dimensional (3D) conductance, where T_0 js a material specific characteristic temperature in K, σ_0 is a material specific characteristic conductance, with unit Ω^{-1}.

and in general for *d*-dimensional compounds, it would be:

$$\sigma = \sigma_0 \exp(-(T_o/T)^{1/d+1}). \qquad (1.10)$$

Hopping conduction at low temperatures is of great interest because of the savings the semiconductor industry could achieve if they were able to replace single-crystal devices with glass layers. Interestingly, the VRH conduction mechanism is also found at a relatively higher range of temperatures [82, 83]. Due to the limitations of our testing equipment, we are unable to provide many experimental results for VRH in the low

temperature range, but nevertheless, some of the samples fit into the higher temperature range of the VRH mechanism, as will be shown in later chapters.

As the samples in this work are 2-dimensional (or quasi-two dimensional) compounds, the most likely VRH fitting model for these samples would be:

$$\sigma = \sigma_0 \exp(-(To/T)^{1/3}). \qquad (1.11)$$

This means, $\ln(\sigma) \propto (1/T)^{1/3}$, that is, if we are to plot $\ln(\sigma)$ vs $(1/T)^{1/3}$, we will get a straight line, if the VRH mechanism applies for the particular range of temperatures.

It should be noted that even though the VRH mechanism is a powerful tool for explaining and characterizing electrical transport in semiconductors, it is not always suitable for all semiconductors. There are other alternative mechanisms in addition to VRH, for example the Nearest Neighbor Hopping (NNH) and Granular Metal (GM) mechanisms, which are beyond the scope of this discussion.

1.2 RELEVANT RESEARCH - K_2NiF_4-TYPE COMPOUNDS

Layer structured, mixed-oxide compounds with Ruddlesden–Popper (RP) structures have attracted many researchers' attention in recent years due to their interesting magnetic and electrical properties. The attention is particularly due to the discovery of superconductivity in this family in 1986 [84] and 1994 [85], and of colossal magnetoresistance in 1993 [39] and 1996 [86], as well as the dielectricity property [87].

The K_2NiF_4-type compounds are the end members of a homologous series of the phases given by the general formula $A_{n+1}B_nO_{3n+1}$. This formula could also be written as $AO(ABO_3)n$, where $1 \leq n \leq \infty$ [88]. A Ruddlesden-Popper compound consists of perovskite blocks that are *n* octahedra thick and separated by rock–salt AO layers along the crystallographic *c*-axis. The presence of the AO layers reduces the three-dimensional characteristics exhibited by the well-known perovskite structure, which is the end member with $n = \infty$ for this family. A schematic presentation of RP-type phases is given in Fig. 1.3. In these structures, the BO_6 octahedral corners are shared with other such octahedra, extending infinitely in the *ab* plane, and the *n* units of such planes stack in the *c*-direction to form the perovskite slab. In the case where A is a rare earth and/or alkaline earth ion, and B is a transition metal ion in such compounds, the electric transport and magnetic properties of these phases within a given series are governed by the identity and valence state of the ions, the width of the *n* perovskite slabs, the B-O-B bond angle, and the oxygen content [85-87].

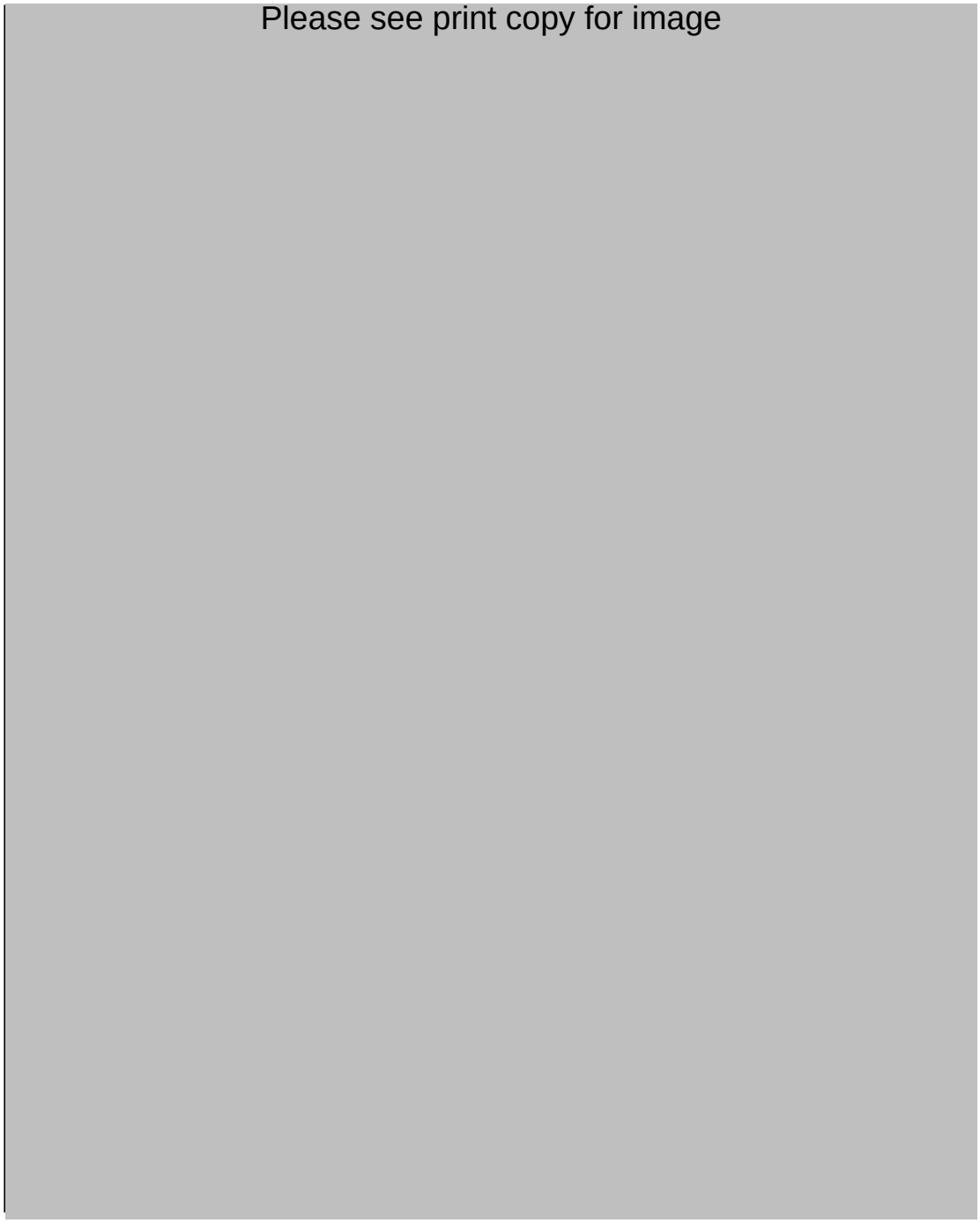

Fig.1. 3 Sketch of the crystal structure of the n = 1, 2, 3, and ∞ members of the perovskite-related layered homologous series $AO(BO_3)_n$ projected along the a- (or b-) axis. Circles represent the A cations. The layers are formed by corner-sharing BO_6 octahedra within the ab-plane. Along the c-axis, the layers are n+1 octahedra thick; thus, the thickness of the layers rises with increasing n. For n = ∞, the three-dimensional perovskite structure ABO_3 is realized. Light and heavy drawings of the BO_6 octahedra, as well as filled and open circles, indicate a height difference perpendicular to the drawing plane [88].

For n = 1, the other limiting composition, A_2BO_4, another well known K_2NiF_4 structure, is formed [89]. It is quasi-two dimensional and can be described as a sequence of BO_2 layers in between AO rock–salt planes, in which the B ions are in a usually distorted octahedral environment, while the A cations are 9-coordinated (Fig. 1.4).

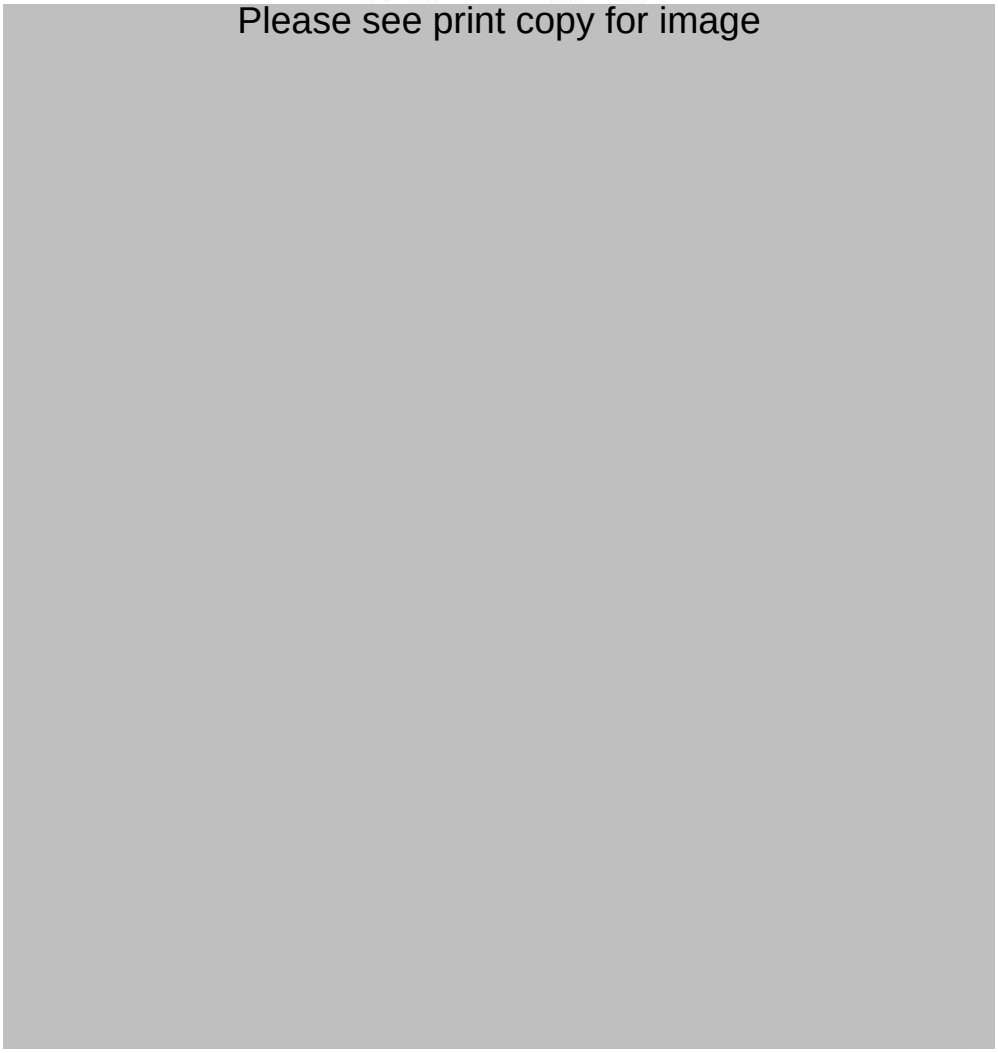

Fig.1. 4. Schematic representation of the K_2NiF_4 structure displayed by the n = 1 RP phase A_2BO_4 [33].

In 2003, Müller-Buschbaum reviewed the crystal chemistry of AM_2O_4 oxometallates [89]. The AM_2O_4 oxometallates were classified into more than 50 structure types according to the categories of crystal structures by numbers of layers of octahedra, tunnel structures, and planar polygons, as well as the presence of structures with small

coordination numbers, such as O–M–O dumb-bells.

The investigation of the crystal structure of K_2NiF_4 [90] is chronologically older than the discovery of the corresponding oxometallate A_2MO_4. That is the reason for calling the oxides K_2NiF_4-like compounds. The fluoride already shows the tendency that this structure type can only exist if the A ions are definitely larger than the M ions. Good examples include the urinates of lithium and sodium. Classic oxometallates [89] with the K_2NiF_4 structure are Ba_4PbO_4, Ba_2SnO_4; Sr_2SnO_4; Sr_2VO_4; and La_2PdO_4. Scholder and Räde [91] assigned Ba_2ZrO_4, Ba_2HfO_4, Sr_2ZrO_4, and Sr_2HfO_4 to the K_2NiF_4-type in an older paper.

The nature and size of the cations at the A and B sites significantly influence the structure and properties of these layer structure phases. The size of the A-site ion at the 9-coordinated position affects the cell parameters and consequently, the structure of these compounds. Larger cations at A sites elongate the interlayer distance, hence cause an increase in *c*, while smaller ions shorten it. The size of the ion at an A site is expected to affect lattice constant *c* more prominently than *a*. Because B-O interactions occur only along the *ab* plane, the cation at B sites is expected to predominantly influence cell parameter *a*.

The acidity of the ions at the A and B sites influences the structure and properties. According to Goodenough (1971), the more basic the cation at the A site, the higher is the covalency of the π(B-O) bond which competes with the σ(A-O) bond. Another factor which influences the behavior of these phases is the Jahn-Teller effect, which comes into existence due to difference in the electronic population in the e_g orbitals.

It was observed that the sites of the A ions can be statistically occupied by two different elements. Examples are the following substances: $AMBO_4$ with AM = Ca/La, B = Ga [92], AM = Sr/Ce, B =Al [93]; AM = Sr/Pr, B = V [94]; AM = Sr/Nd, B = Co [95]; AM = Sr/Sm, B = Ni [96].

In recent years, there has been considerable interest in $A_{2-x}M_xBO_{4\pm\delta}$ mixed oxides (A = Ln; M = Ca, Sr, Ba; B = Mn, Fe, Co, Ni, Cu) with the K_2NiF_4-type crystal structure. These compounds have high total electrical conductivity and are characterized by high oxygen mobility as well as fast oxygen exchange kinetics between the solid and the gas phases [97–99]. They are being considered as potential cathode materials for solid oxide fuel cells (SOFC) [100, 101], oxygen pumps [102], oxygen permeable membranes [102, 103], and catalysts for oxidation of hydrocarbons [104].

The physical properties of the oxides of the 3d transition metals, such as Fe, Co, and Mn with the K_2NiF_4-type structure have attracted considerable attention, not only because of the similarity of these oxides to the superconducting Cu oxides, but also because of the underlying Mott–Hubbard physics [105-109]. Imada et al. [110] comprehensively reviewed these compounds with 3d electron numbers from 1 to 9, and for electron and hole doping (viz. increase and decrease of band filling, respectively, of the parent correlated insulator). The properties of some of these compounds were also discussed.

In the 1960s all rare-earth oxometallates with the composition Ln_2CuO_4 (Ln = La, Gd) were assigned to the K_2NiF_4 structure. These compounds actually possess a modified K_2NiF_4 structure. The first investigations on the distorted orthorhombic structure of

La_2CuO_4 [111-112] were overshadowed at the end of the 1980s by the turbulent investigations of the superconducting phases of $La_{2-x}M_xCuO$.

In order to obtain a deeper understanding of the mechanisms of superconductivity, there have been many studies of the physical and structural properties of Cu-free oxides, e.g. titanates and ruthenates.

Fig. 1.5 [113] shows the results for Sr_2RuO_4 (n = 1), $Sr_3Ru_2O_7$ (n = 2) and $SrRuO_3$ (n = ∞). Note that $SrRuO_3$ is well known as a ferromagnetic metal with a ferromagnetic transition temperature T_C =160 K [113,114]. It is an itinerant ferromagnet, i.e. the ferromagnetic ordering is due to delocalized electrons. It represents one of the very few ferromagnetic materials without a 3d or 4f element. The resistivity behavior of $SrRuO_3$ shown in Fig.1.5 is in accordance with the data published by Bouchard and Gillson in 1972 [116]. For the layered Sr_2RuO_4 and $Sr_3Ru_2O_7$, it seems likely that the true resistivity behavior differs from that shown in Fig. 1.5, because the polycrystalline nature of the samples hides their anisotropic features along and perpendicular to the layers. Also, grain boundaries were expected to influence the resistivity behavior.

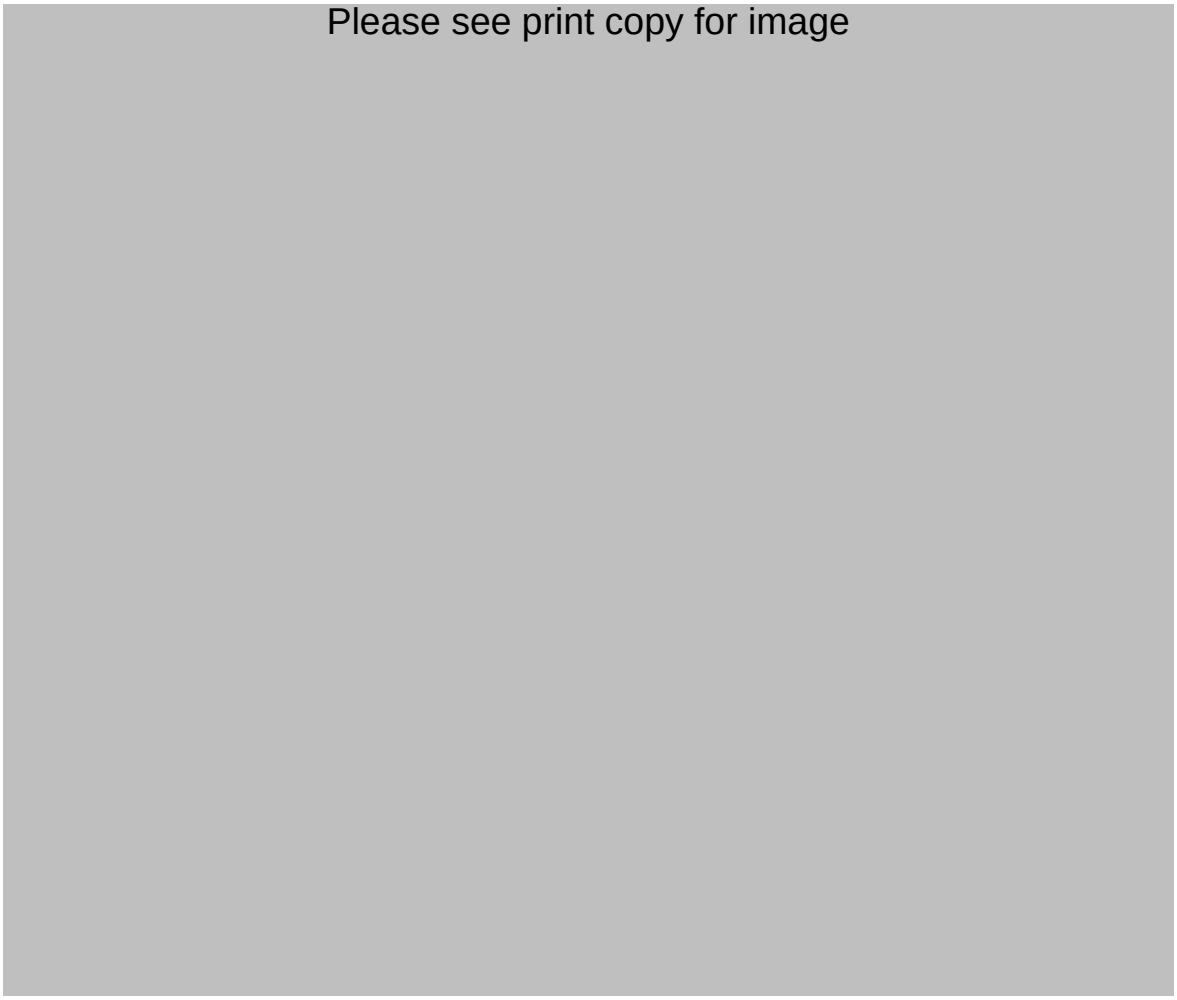

Fig.1. 5 Resistivity as a function of temperature for polycrystalline Sr–Ru–O compounds. The oxidation state of the Ru ions is the same for all of these compounds, namely, $Ru^{4+}/4d^4$. The position of the ferromagnetic transition temperature T_C of $SrRuO_3$ is indicated by an arrow [88, F. Lichtenberg, 2002].

In 1994, Maeno and Hashimoto from the University of Hiroshima (Japan) searched for superconductivity in Sr_2RuO_4 at low temperatures below 4 K. Measurements on single crystals revealed the presence of superconductivity with $T_c = 0.93$ K in an unambiguous way, as shown in Fig. 1.6 [116].

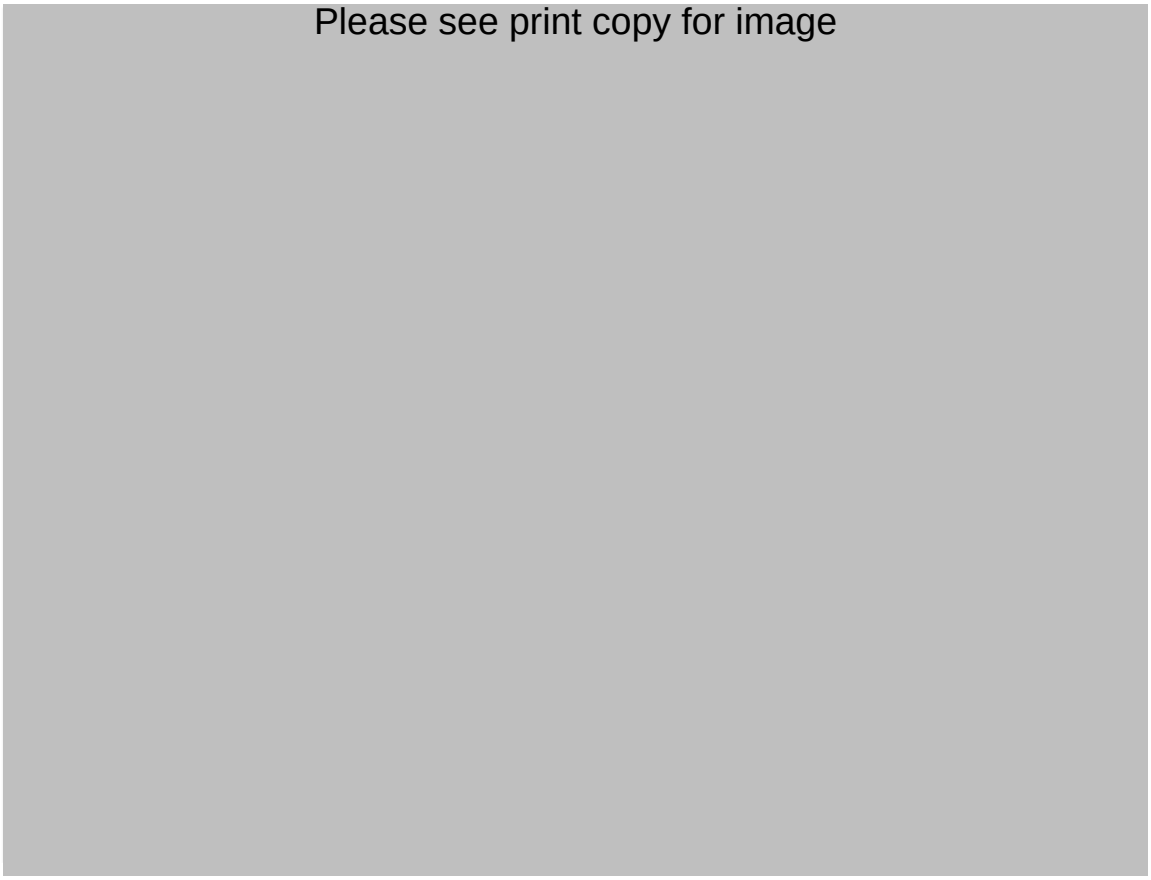

Fig.1. 6 Low temperature behavior of Sr_2RuO_4 single crystals. Left: Real part χ'' and imaginary part χ' of the magnetic susceptibility. Right: Resistivity ρ_c and ρ_{ab} perpendicular to and along the layers, respectively. Note that $\rho_c \approx 10^3 \times \rho_{ab}$. The resistivity curves clearly display the existence of superconductivity with $T_c = 0.93$ K. These results were obtained in 1994 with crystals grown by F. Lichtenberg in 1990 [116].

Since that time, Sr_2RuO_4 has gained considerable attention, and more than 400 papers have been published on this compound. It is an unconventional spin-triplet superconductor with intriguing superconducting properties. These are discussed in two excellent review articles by Mackenzie and Maeno [117] and by Maeno, Rice and Sigrist [118]. Physical properties studies [119, 120] have firmly shown unconventional superconducting properties at close to $T_c = 1.5$ K. As a heavy fermion system, Sr_2RuO_4 is not an *s*-wave type superconductor [121]. The main consequence is a non-magnetic impurity effect at very low concentration, which sharply reduces the superconducting temperature to 0 K [122, 123].

The superconductivity in Sr_2RuO_4 is a very active field of research, and there are many open questions.

The search for RP-type phases containing transition metals other than copper has revealed giant and colossal magnetoresistive effects in RP-type cobaltites [124] and manganites [125], respectively. Generally, RP chemistry is diverse, although RP-type phases containing chromium are less common and difficult to prepare under conventional synthetic conditions. Tom Baikie et al. [126] prepared the K_2NiF_4-type phase Sr_2CrO_4 at ambient pressure. The material displays antiferromagnetic interactions (as shown in Fig. 1.7), but there is no transition to long-range magnetic ordering. The magnetic susceptibility data for Sr_2CrO_4 are quite noisy, probably due to the small magnetic moments of the sample and the presence of secondary phase(s).

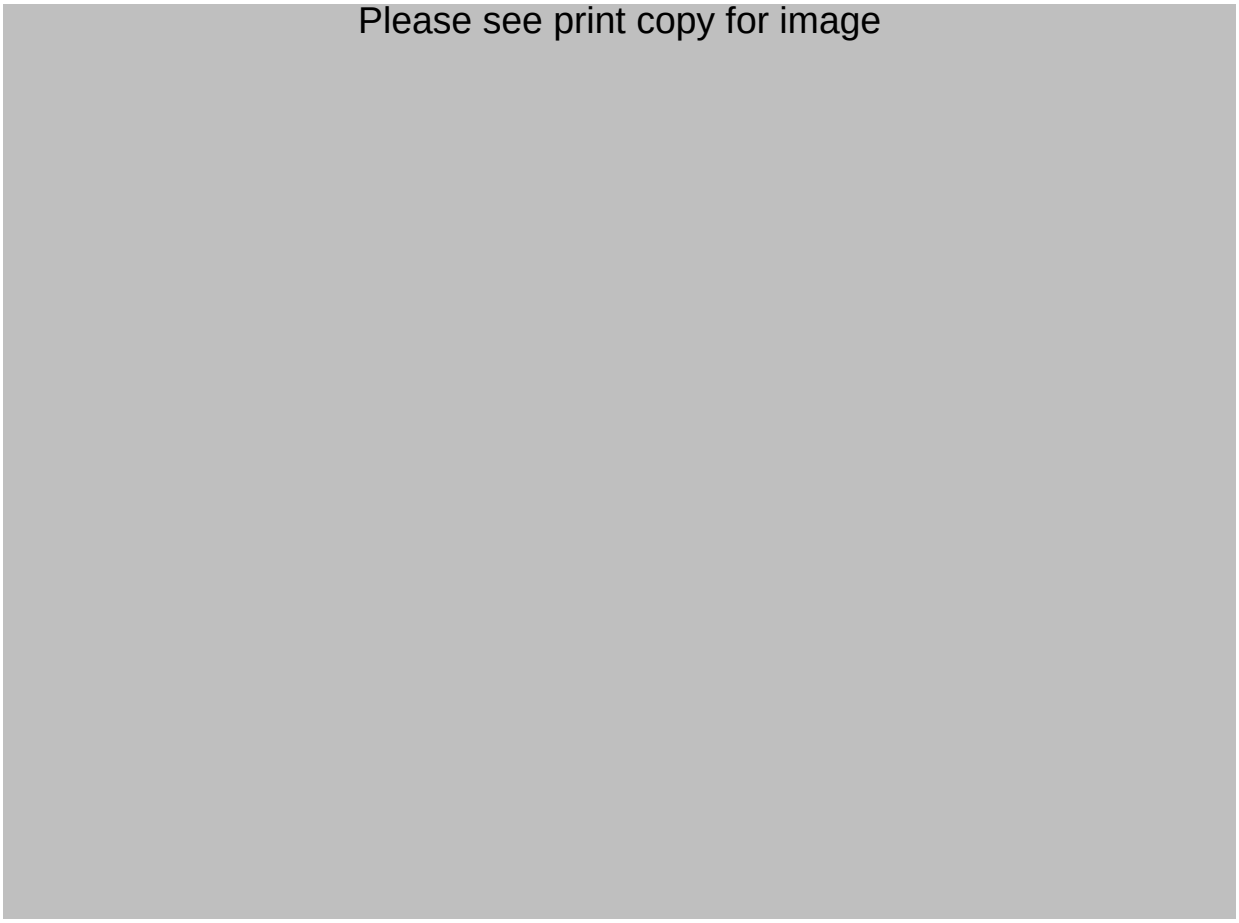

Fig.1. 7 *Magnetic susceptibility versus temperature plot for Sr_2CrO_4 in a magnetic field of 3000 Oe. [Baikie 2007]*

Cobalt-based RP structure oxides are of particular interest due to the richness of the available cobalt oxidation states and the intriguing competition between low-spin, high-spin, and intermediate-spin configurations for Co. These different spin states are the key to understanding the peculiar way the magnetic and transport properties change with composition and temperature.

RP structures containing only Co^{4+} ions are known for the n = ∞ compound, $SrCoO_3$, which can be obtained as a completely stoichiometric perovskite either at high oxygen pressure [127] or by electrochemical oxidation of $SrCoO_{2.5}$ at room temperature in alkaline media. The resultant sample is metallic and, at temperatures below T = 280K, it

shows ferromagnetic behavior. The magnetic moment at 0 K is 2.1 μ_B [128]. The electrochemical and chemical oxidation were shown to be reversible processes with the appearance of intermediate compounds [129].

When doped with rare earth elements (Ln = Y, Ho, Dy, Sm-Tm), it was found that the stability of the perovskite related structure decreases with decreasing size of the cations, and the doping has also revealed the presence of a complex perovskite-related superstructure phase [130, 131]. Ce doping turns strontium cobaltite into a stabilized, highly conductive material [132]. The perovskite form of $Ce_{1-x}Sr_xCoO_{3-\delta}$ is only stabilized over a relatively narrow solid solution range ($x > 0.85$). It shows ferromagnetic behavior under applied magnetic fields with an ordered cobalt moment of 1.7 μ_B at 25 K [133].

The substitution of a tetravalent cation for Sr^{2+} appears to be a promising route to synthesize $SrCoO_{3-\delta}$ itinerant ferromagnets without the use of high oxygen pressure or of electrochemical oxidation.

In 1995, Dann et al. [134] prepared an oxygen-deficient PR phase with n = 2, $Sr_3Co_2O_{7-\delta}$ ($0.94 \leq \delta \leq 1.22$). It was found that at low δ (0.94), the system is tetragonal (*I4/mmm*), but as δ (1.06, 1.22) increases, a phase change to orthorhombic (*Immm*) occurs. Viciu et al. [135] successfully synthesized three cobalt-based oxygen deficient members of orthorhombic $Sr_3Co_2O_{5+\delta}$ with δ = 0.91, 0.64, and 0.38 in a nitrogen atmosphere. The crystal structures were determined by powder neutron diffraction. Fig. 1.8 presents the idealized crystal structure of $Sr_3Co_2O_{5+\delta}$. Oxygen vacancies are found both in O(3) and O(4) sites, but the majority are along one crystallographic axis in the CoO_2 plane,

inducing an orthorhombic distortion of the normally tetragonal n = 2 Ruddelsden–Popper structure.

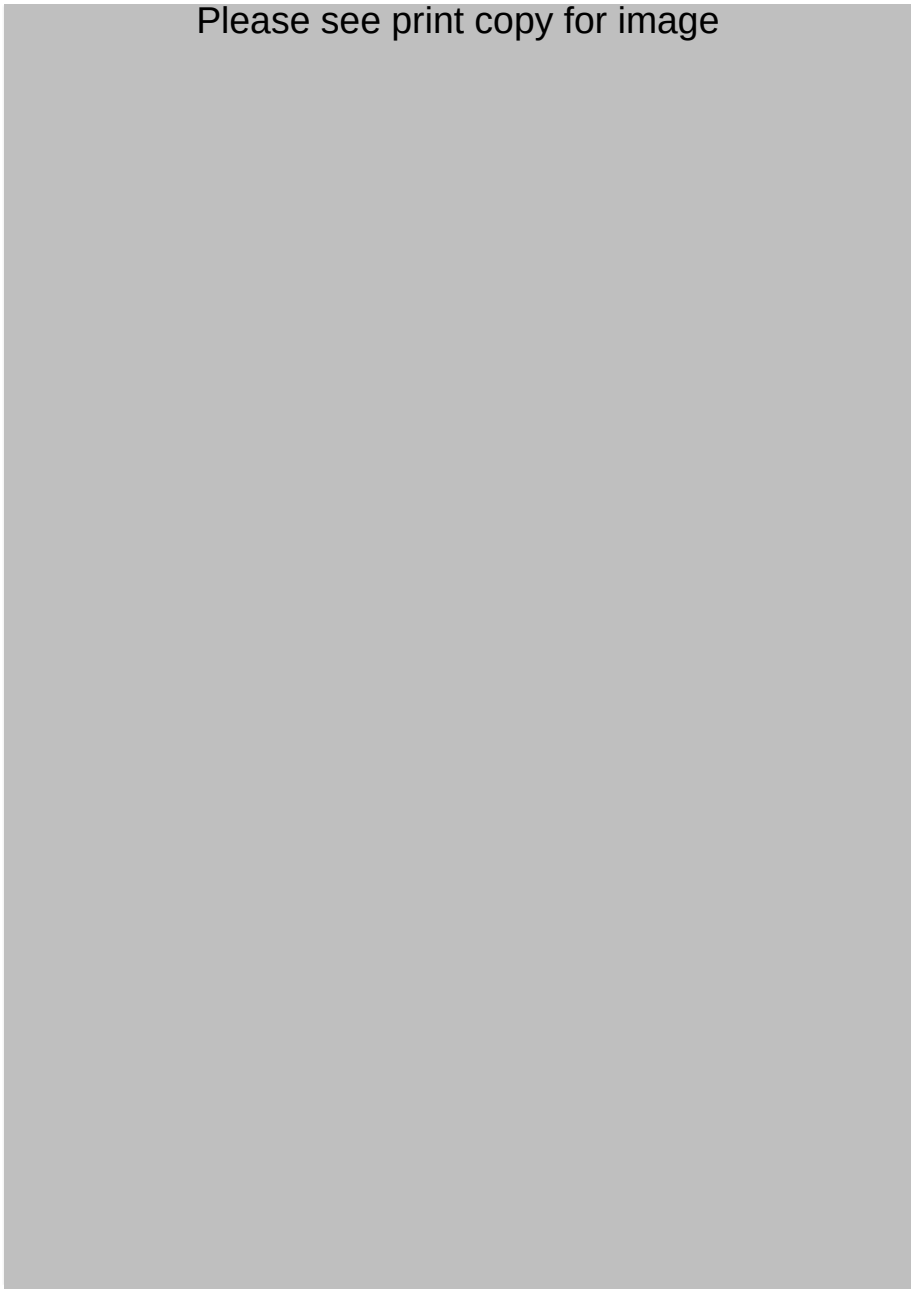

Fig.1. 8 Idealized representation of $Sr_3Co_2O_{5+\delta}$ structure. The right side of the figure shows the displacement of O(2) and how the polyhedra are distorted [136].

Superstructures due to oxygen ordering are observed by electron microscopy. The magnetic measurements reveal complex behavior, with some ferromagnetic interactions

present for $Sr_3Co_2O_{5.91}$ and $Sr_3Co_2O_{5.64}$, as shown in Fig. 1.9 and Fig. 1.10, respectively.

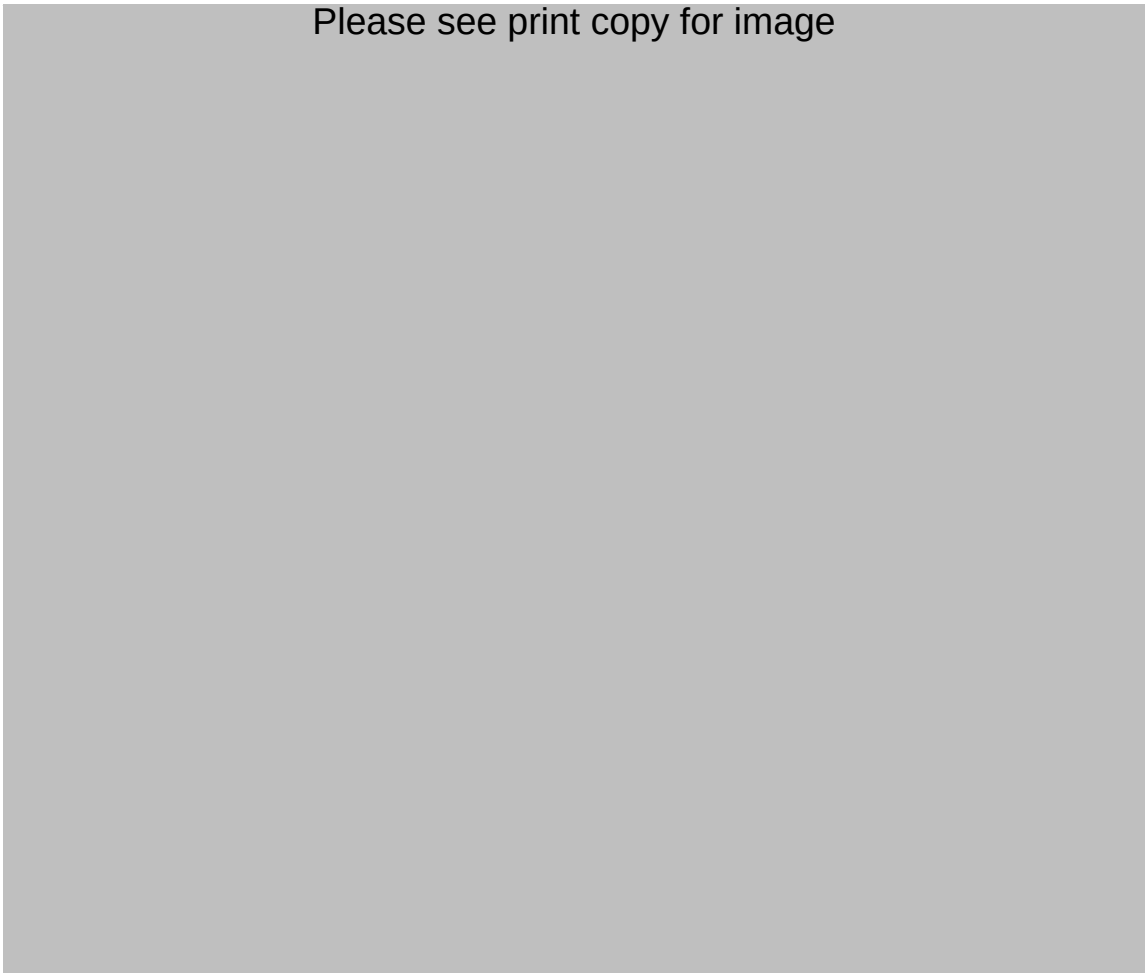

Fig.1. 9 Temperature dependence of magnetic susceptibility for $Sr_3Co_2O_{5.91}$.

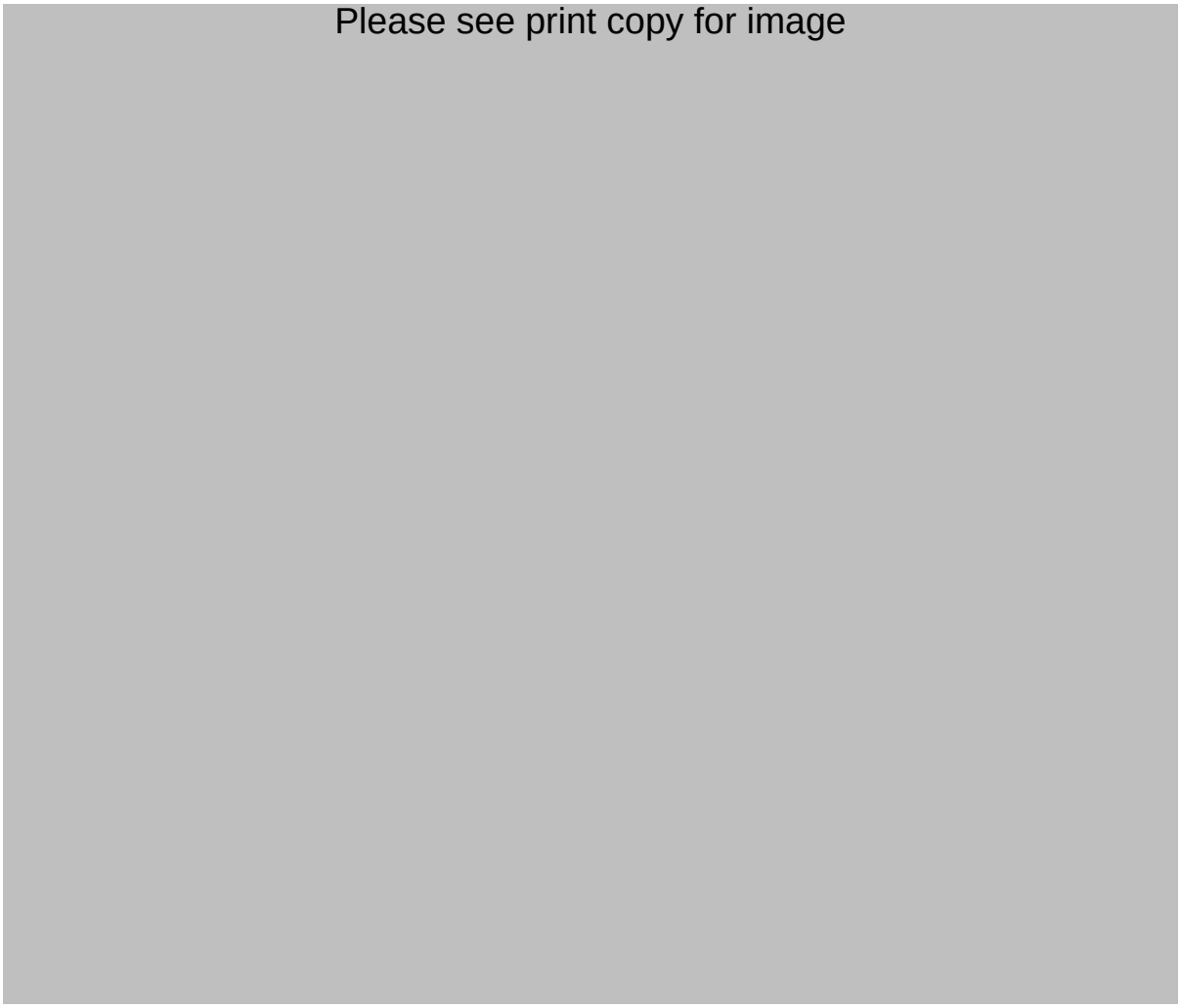

Fig.1. 10 *Temperature dependence of magnetic susceptibility for* $Sr_3Co_2O_{5.64}$.

In attempts to increase the oxygen content, $Sr_3Co_2O_{6.06}$ was obtained, a material that is not stable under atmospheric conditions, converting to an oxyhydrated form.

Hill et al. [136] soon extended the structural and magnetic phase diagrams of the bilayer Ruddlesden-Popper phase $Sr_3Co_2O_x$ beyond previously reported limits of $x \approx 6.1$ to $x = 6.60$. The room temperature crystal structure for the $x = 6.60$ material is orthorhombic, with oxygen vacancies located in the apical position that links the two nominally CoO_2 layers in the perovskite block. An antiferromagnetic ground state is converted to ferromagnetic by moderate magnetic fields, and high-temperature magnetic

susceptibility data indicate short-range ferromagnetic order. Oxygen vacancies are present in both the in-plane sites, as well as the linking apical site in the range of $5.64 \leq x \leq 5.80$. Additionally, low-temperature neutron powder diffraction (NPD) and magnetization data show that the magnetic ground state of these oxygen-deficient materials is a complex antiferromagnet, with considerable sensitivity to the precise oxygen content. Fig. 1.11 presents the M/H data plotted as a function of T for $Sr_3Co_2O_x$ ($x < 6$), clearly showing that the magnetic properties vary dramatically with small changes in oxygen content.

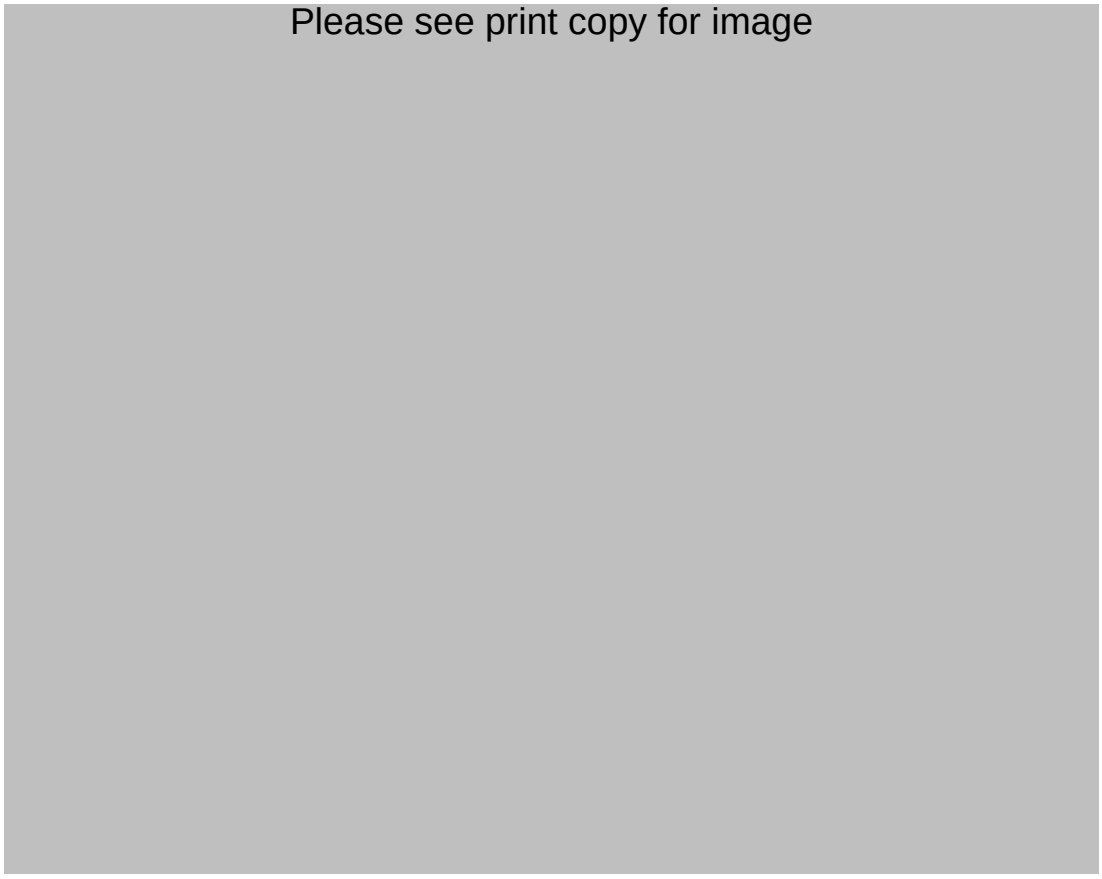

Fig.1. 11 Magnetization divided by magnetic field vs. temperature data for $Sr_3Co_2O_x$ samples: A (x = 5.80), B (x = 5.71), C (x = 5.73), and D (x =5.64). For clarity, the D data were shifted down by 0.003 cm^3 /mol [137].

It has been found that the most oxidized phases ($\delta \approx 1$) of $Sr_3Co_2O_{7-\delta}$ are very unstable in air, showing a very rapid reaction with water. The intercalation process starts with the introduction of OH^- groups, to form $(SrOH)^+$ layers, and the intercalation of additional H_2O molecules has been found to significantly expand the thickness of the block separating two successive perovskite blocks [137]. The strong air sensitivity of the $Sr_3Co_2O_{7-\delta}$ ($\delta \approx 1$) phases could originate from the unstable CoO_x polyhedra and thus explain the experimental difficulty in stabilizing more oxidized phases, such as $\delta \ll 1$. The topotactic behavior of the hydrolysis process for the $Sr_3Co_2O_{7-\delta}$ phase is demonstrated in Fig.1.12.

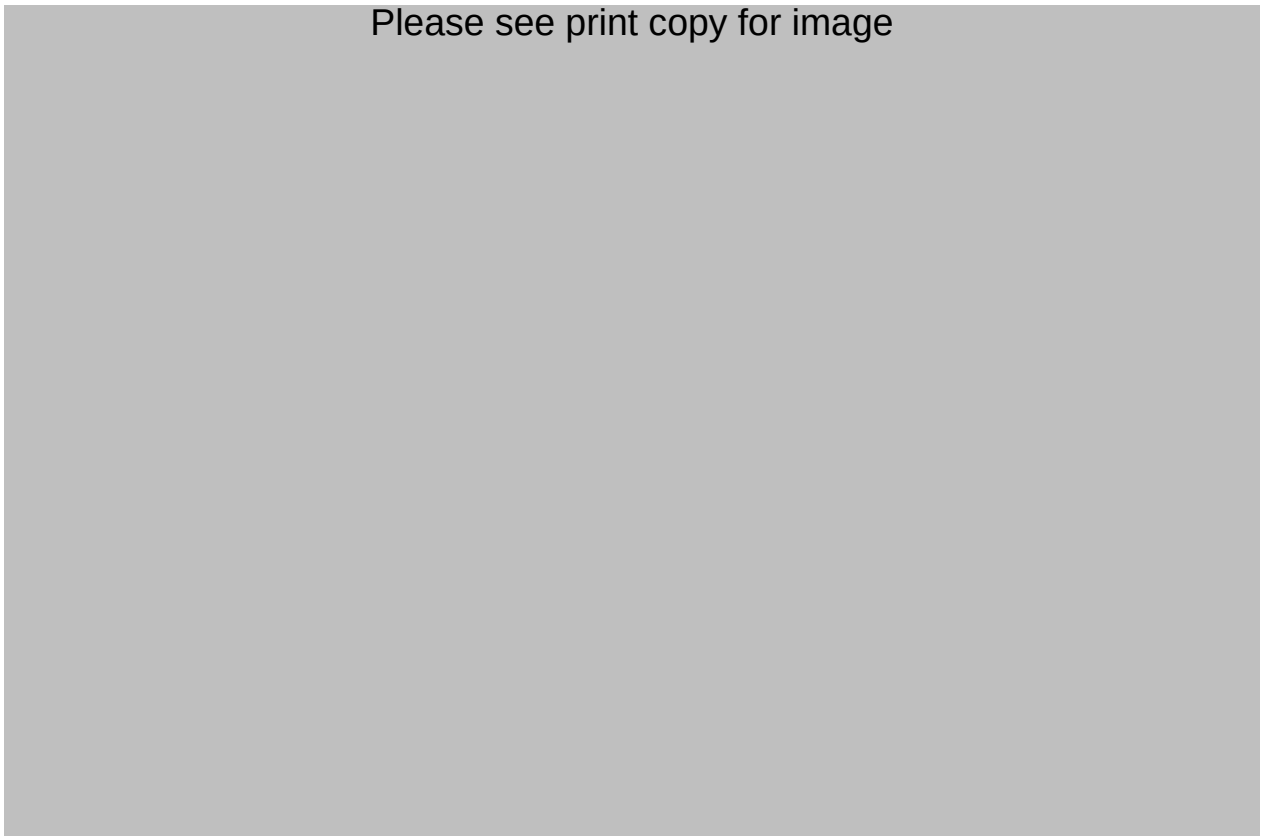

Fig.1. 12 *Left figure: hydrated oxyhydroxides $Sr_{n+1}MnO_{3n-1}(OH)_2 \cdot H_2O$ (M = transition metal) obtained by hydrolysis/hydration of the corresponding members of the RP series $Sr_{n+1}MnO_{3n+1}$ (right figure). By removing one H_2O molecule from the hydrated oxyhydroxide, the oxyhydroxides $Sr_{n+1}MnO_{3n-1}(OH)_2$ are obtained (central figure). The*

thickness evolution of the block separating two successive perovskite blocks depends on the intercalated groups. The dashed lines are used to suggest the n layers [138].

A series of oxygen-deficient n = 2 Ruddlesden–Popper phases, $Sr_3Fe_{2-x}CoxO_{7-\delta}$ ($0.25 \leq x \leq 1.75$), were prepared by solid state reaction [138]. These compounds are still unstable in air, and the dominant magnetic interactions are ferromagnetic. All the Fe doped phases are semiconducting with the variable-range hopping mechanism. Large negative magnetoresistance (with the largest MR ≈ -65% for x = 0.25) is observed for all phases. Fe ions are tetravalent on average with a strong covalency-induced superposition of *d* configurations.

The second member of the Ruddlesden–Popper series, n = 2 in $Sr_{n+1}Co_nO_{3n+1}$, has been stabilized by substituting cerium for strontium, leading to the pure compound $Sr_{2.75}Ce_{0.25}Co_2O_{7-\delta}$. The oxygen vacancies of this phase can be partially filled by a post-annealing oxidizing treatment, with δ decreasing from 1.1 to 0.3 for the as-prepared and oxidized phases, respectively. As the samples are oxidized from $\delta \approx 1.1$ to 0.3, the *a* and *b* unit cell parameters decrease. Despite the average value of the cobalt valence state, $V(Co) \approx +3.5$, obtained in the oxidized $Sr_{2.75}Ce_{0.25}Co_2O_{6.7}$ phase, a clear ferromagnetic state with $T_C = 175K$ is reached. The results also confirm the ability of cerium to be substituted into RP strontium based cobaltates in the $n = \infty$ and n = 1 phases [139].

In May 2005, Wang et al. made the very first such report on their successful synthesis of the RP series of $(SrO)(SrCoO3)_n$ where n = 1, 2, 3, 4, and ∞, and relevant discussions on the structures, transport, and magnetic properties were presented [140]. They found that these compounds crystallize in tetragonal structures for $n \leq 4$, and in cubic for n =

∞. These compounds are ferromagnetic, with the Curie temperatures decreasing as n increases, as shown in Fig. 1.13, a graph reproduced from Wang's report.

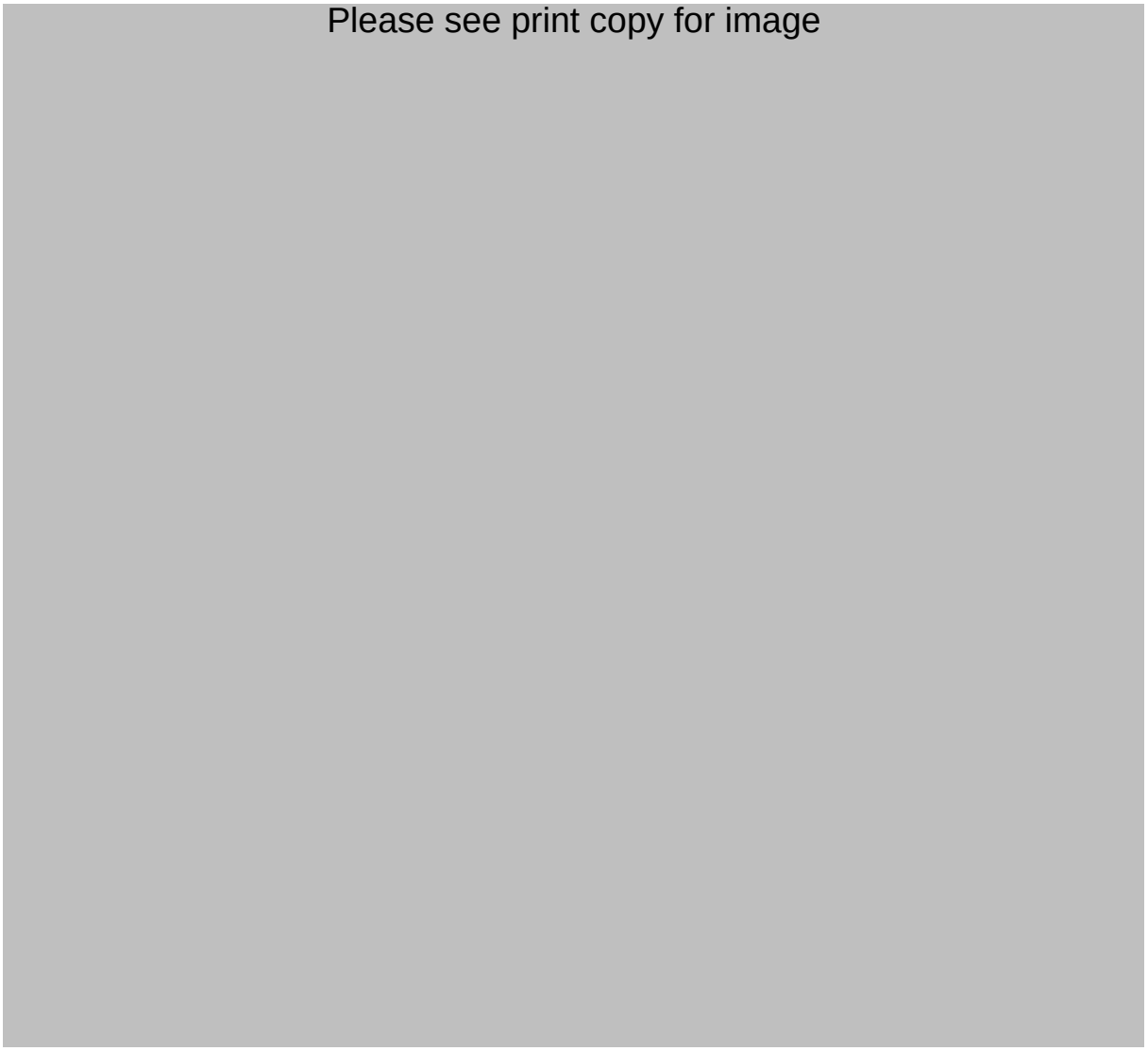

Fig.1. 13 DC magnetization vs. temperature for $(SrO)(SrCoO_3)_n$, where n = 1, 2, 3, 4, and ∞. Inset is the Curie–Weiss fitting for the n =1 sample [140].

Wang also presented a coercive field as large as 2.5 Tesla for the Sr_2CoO_4 compound at 5 K as shown in Fig. 1.14. This clearly shows the great potential of Sr_2CoO_4, which could be a good candidate for high quality magnetic memory applications or similar equipment for industrial purposes.

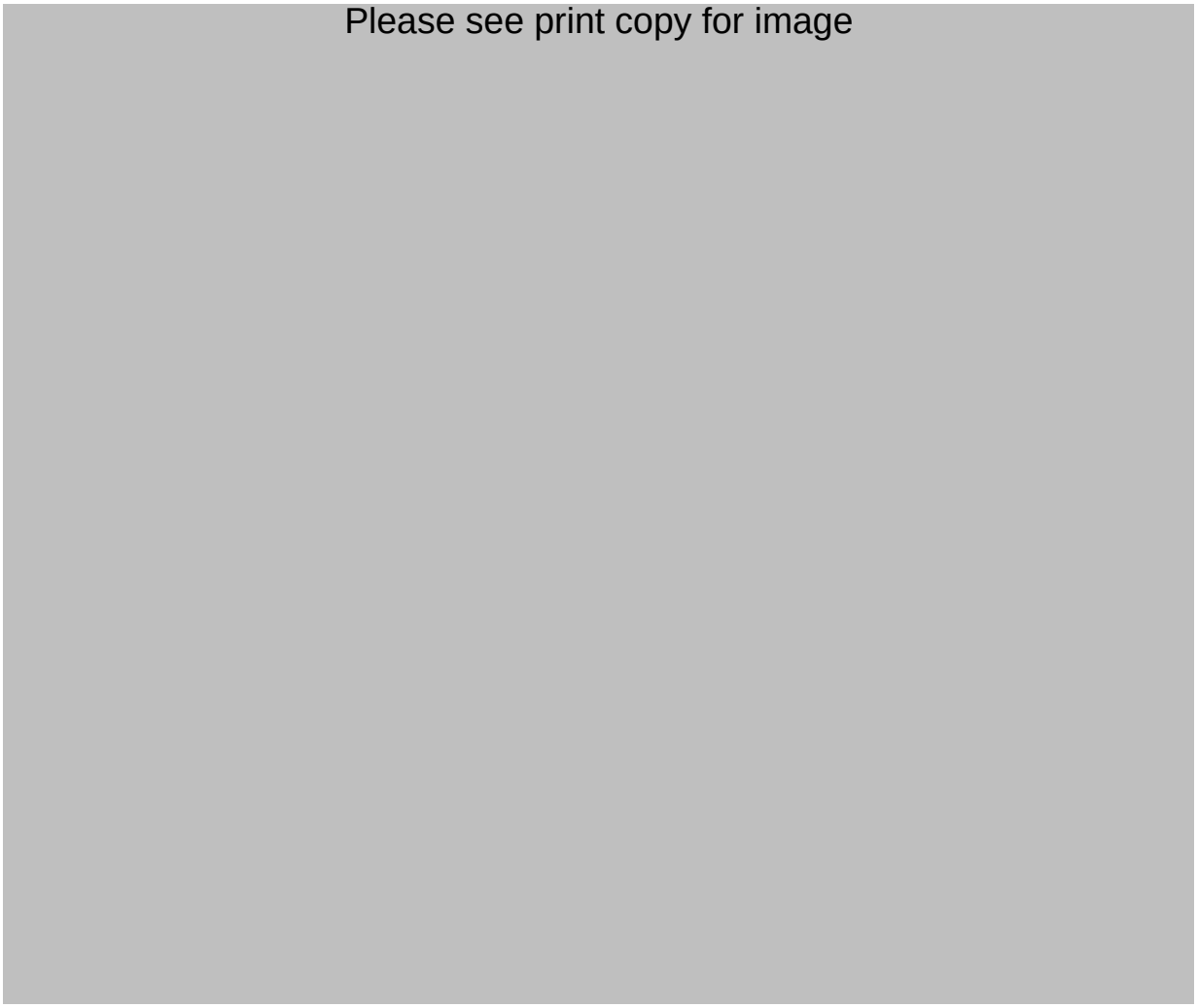

Fig.1. 14 Magnetic hysteresis loops (lower panel) and field-hysteretic magnetoresistance
(upper panel) for Sr_2CoO_4 at 5 K [140].

It should be noted that Wang's method for achieving these unusual and seemingly useful results on Sr_2CoO_4 compound was with a high pressure and high temperature technique, but such methods are not practical for industrial production of these compounds. Therefore, alternative practical methods for synthesizing such compounds would be desirable.

Also in 2005, J. Matsuno et al. reported that they had successfully synthesized single phase Sr_2CoO_4 in the form of a single-crystalline thin film with square-lattice CoO_2

sheets (of K_2NiF_4-type structure) [34]. They found that this compound was a metallic ferromagnet, with appreciable magnetic anisotropy and quasi-two-dimensional transport properties. They thus claimed that the CoO_2 layers can act as a stage for two-dimensional ferromagnetism as well as superconductivity. The fairly high T_C (250 K) that this group found for Sr_2CoO_4 (the same as Wang's result [140]) may provide, as we can imagine, very intriguing opportunities to explore the spintronic functionality of CoO_2 layers. Fig. 1.15 contains a reproduced graph from [140] giving the temperature dependence of the magnetization M for Sr_2CoO_4 thin films. The inset shows the field dependence of the magnetization M measured at 5 K.

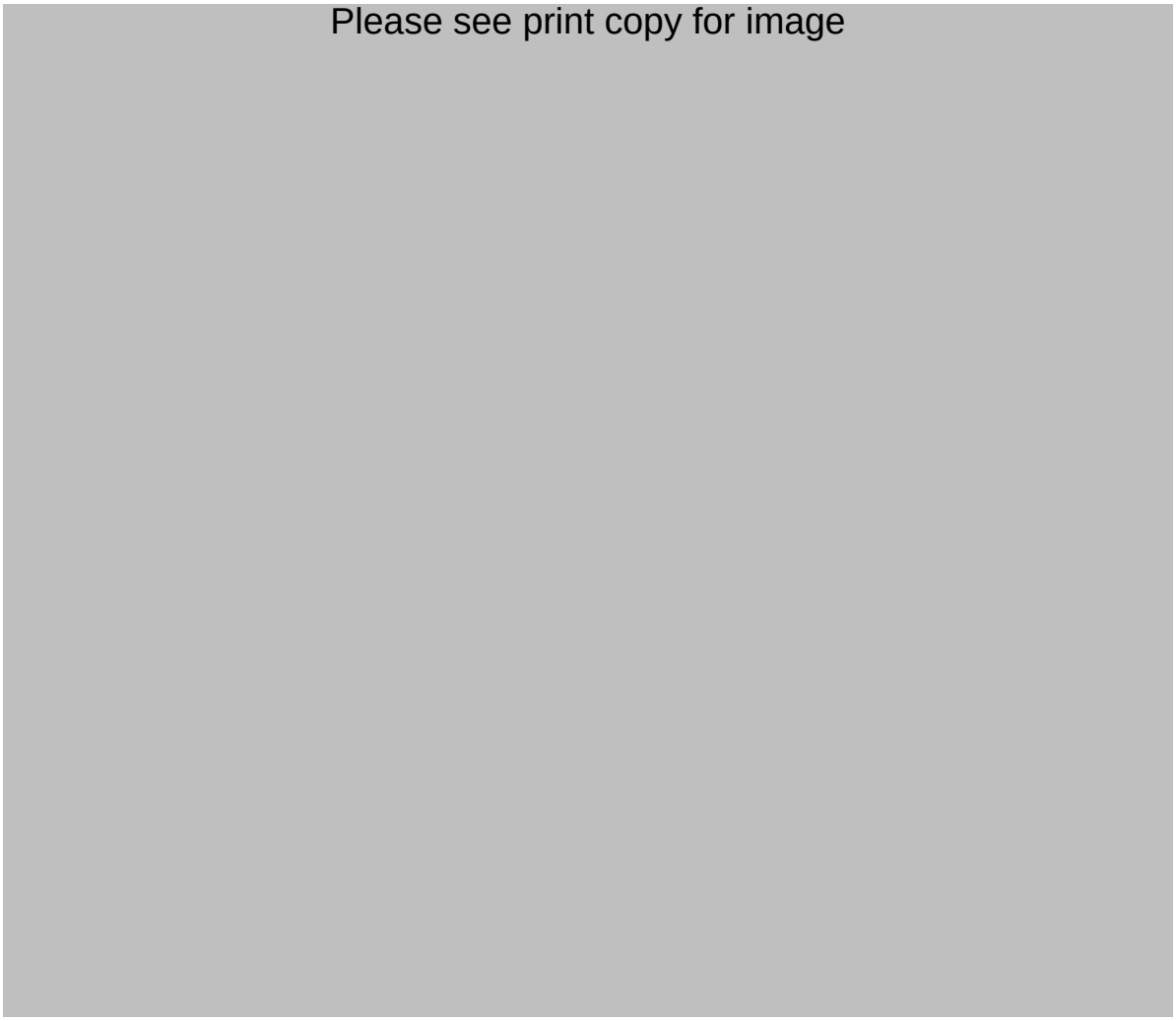

Fig.1. 15 Temperature dependence of the magnetization M for Sr_2CoO_4 thin films. Inset shows the field dependence of the magnetization M measured at 5 K [140].

It should be noted again that Matsuno's sample was produced by a complicated PLD method with an initial target of polycrystalline Sr_2CoO_4 (with details on how the polycrystalline target of Sr_2CoO_4 was produced not provided in his report), and the experimental method described by Matsuno is rather complex and industrially impossible for mass production purposes. Nevertheless, a similar coercive field for the single crystal sample of Sr_2CoO_4 of about 2.5 T was achieved in his sample, so this reconfirms Wang's finding about the unusual properties of compounds with the Sr_2CoO_4 structure.

Hideki Taguchi reported (2007) that K_2NiF_4-type $Ca_{1+x}Sm_{1-x}CoO_4$ ($0.00 \leq x \leq 0.15$) compounds were synthesized successfully by a polymerized complex route [141]. Taguchi claimed that the decrease in the cell parameters (*a* and *b*) with doping was caused by the difference in the ionic radii between the Co^{3+} and Co^{4+} ions, while the increase in the *c* lattice parameter was caused by the increase in the Ca,Sm - Ca,Sm distance. Also, $Ca_{1+x}Sm_{1-x}CoO_4$ is a *p*-type semiconductor and exhibits hopping conductivity in the small-polaron model at low temperatures. Taguchi showed that the $1/\chi$ vs. T curves deviate from the Curie Weiss law, as $Ca_{1+x}Sm_{1-x}CoO_4$ shows paramagnetic behavior above 5 K. A reproduced figure from Taguchi's paper of the $1/\chi$ vs. T curves is shown in Fig. 1.16.

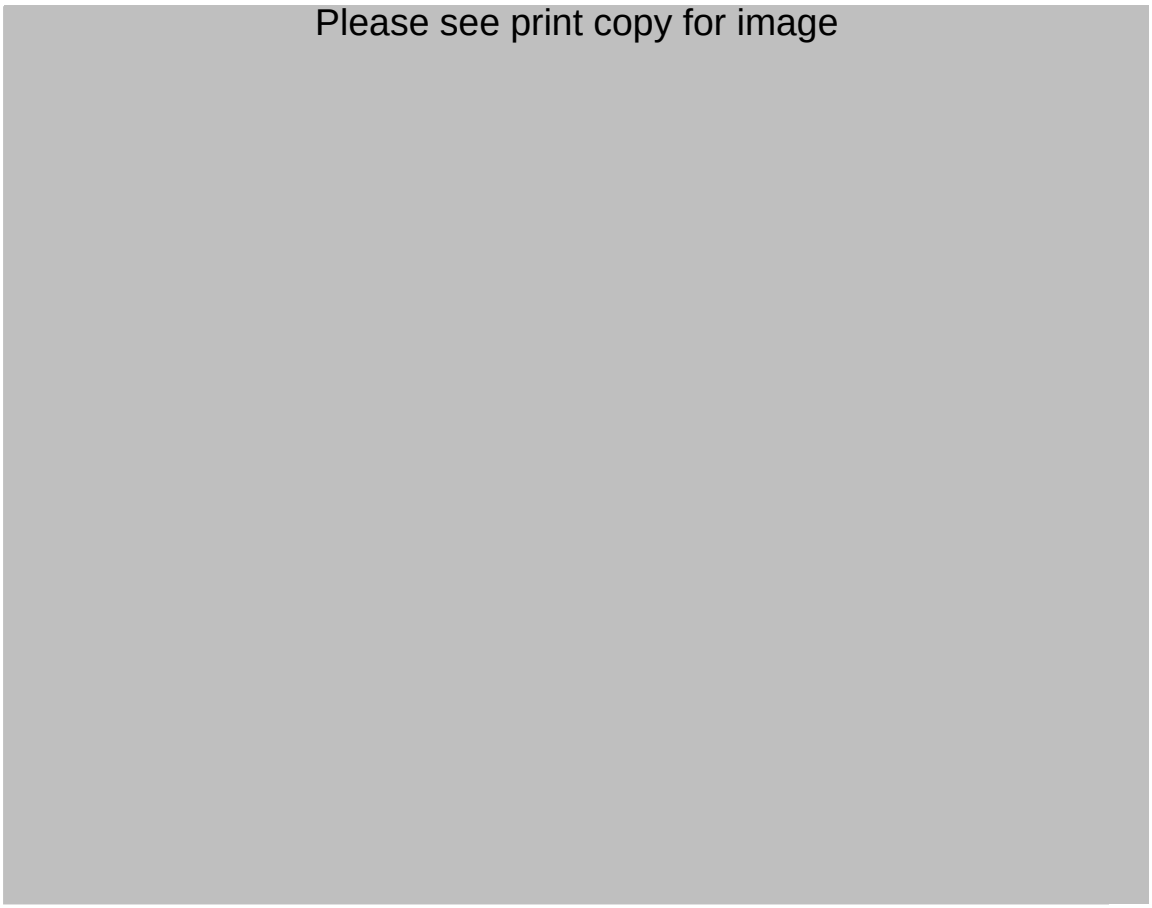

Fig.1. 16 The temperature dependence of the reciprocal of the magnetic susceptibility (1/χ) of $Ca_{1+x}Sm_{1-x}CoO_4$ [142].

Taguchi pointed out that both the Co^{3+} and Co^{4+} ions are localized and have low-spin states. He thus claimed that the results indicate that the Co^{4+} ion acts as an acceptor, and that the electron transfer becomes active through the Co^{3+} – O - Co^{4+} path as the proportion of Co^{4+} ions is increased. Even though Taguchi's complex experimental method for obtaining the $Ca_{1+x}Sm_{1-x}CoO_4$ is not very close to our set target of a "industrially practical method for sample fabrication", his findings on the changes in lattice parameters vs. the compound compositions provided a good reference in our study on RE-doped Sr_2CoO_4 polycrystalline compounds.

In late 2005, Liu et al. reported that polycrystalline $SrLaCoO_4$ with the tetragonal

K_2NiF_4 structure had been successfully synthesized by a solid-state reaction process [142], and they found that the sample had a paramagnetic–ferromagnetic transition that occurred at around 250 K. In a magnetic field of 5 T, the maximum magnetoresistance (MR) of 18.4% was obtained at 12 K for this compound, as shown in Fig. 1.17.

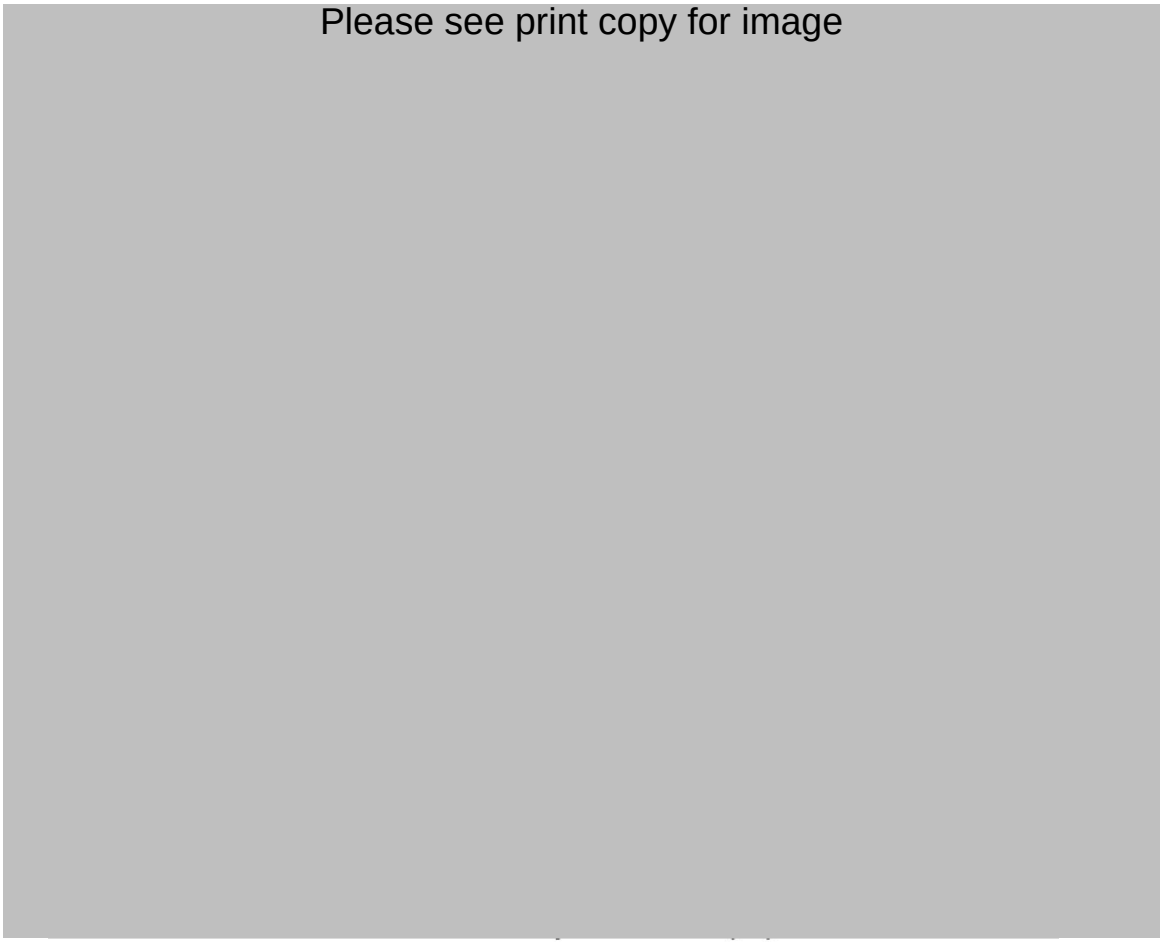

Fig.1.17 Temperature dependence of the magnetoresistance of polycrystalline $SrLaCoO_4$ for 2.5 T and 5 T fields [21]. Reproduced from [143].

This was a good indication that doped polycrystalline Sr_2CoO_4 compounds could be colossal magnetoresistance (CMR) materials. It should be noted that Liu's sample had "fractional diffraction lines of perovskite phase existing". Perhaps with a slightly different approach to sample preparation, this perovskite phase impurity could have been eliminated – as can be seen in our results later on.

In 2005, Xu et al. reported that new layered cobalt oxides $Sr_{2-x}Ho_xCoO_4$ ($0.00 \leq x \leq 1.0$) with square-lattice CoO_2 sheets (K_2NiF_4-type structure) had been synthesized using a high pressure and high temperature technique [143]. They found that for the Sr_2CoO_4 compound, with increasing doping content of Ho, the T_C decreased to 150 K for x = 0.5 and ferromagnetism was not observed for x = 0.67 (Fig. 1.18). The Ho substitution effects on the magnetic and transport properties (Fig. 1.10), and the spin states of Co were also studied for the $Sr_{2-x}Ho_xCoO_4$ system. They found that large magnetoresistance was also observed at both low temperatures and the vicinity of T_C (for $x \leq 0.3$) (Fig. 1.19), which can be ascribed to the tunneling magnetoresistance at grain (or domain) boundaries and an intrinsic mechanism.

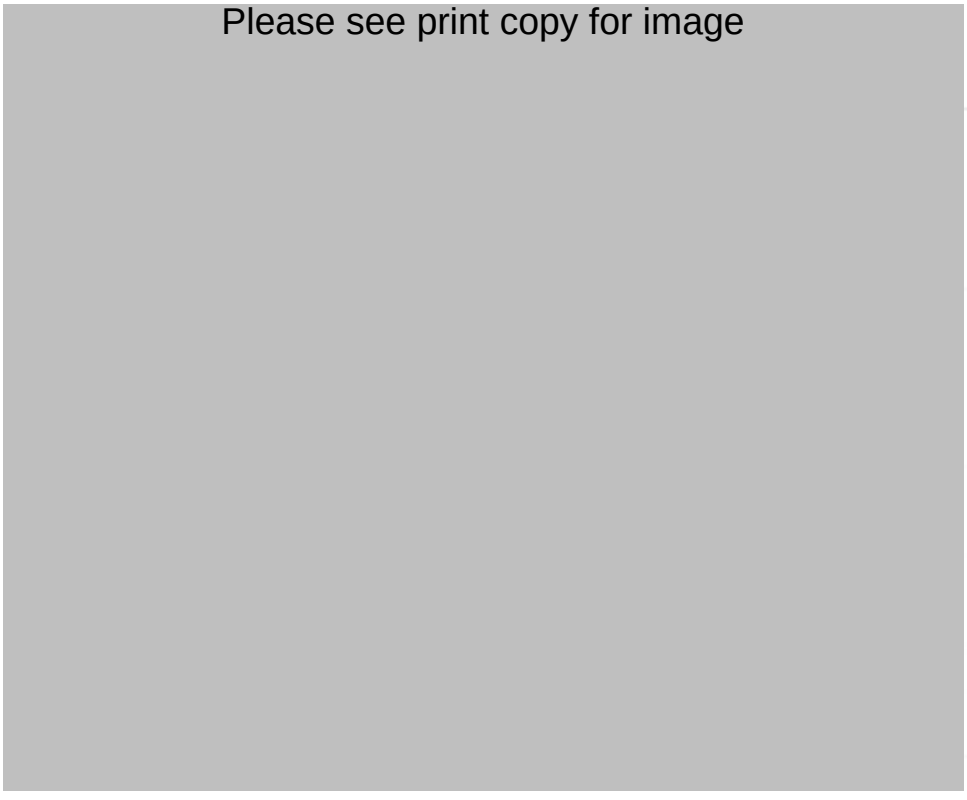

Fig.1. 18 Temperature dependence of the field-cooled dc magnetization of $Sr_{2-x}Ho_xCoO_4$ [144].

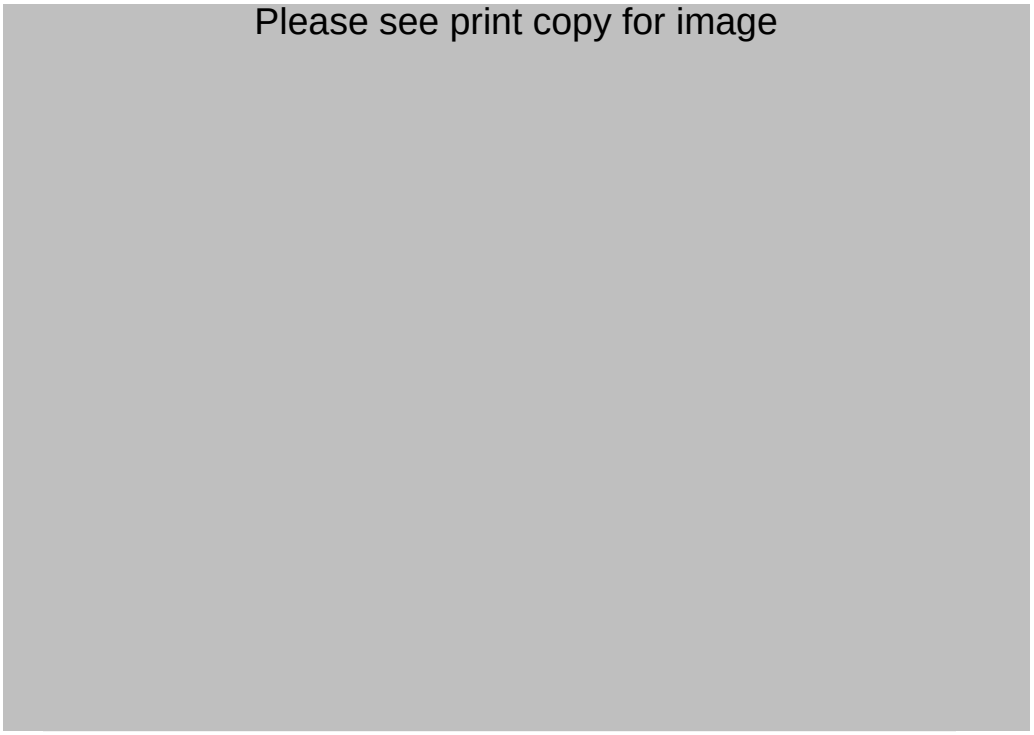

Fig.1.19 Temperature dependence of the electrical resistivity for the $Sr_{2-x}Ho_xCoO_4$ system [144].

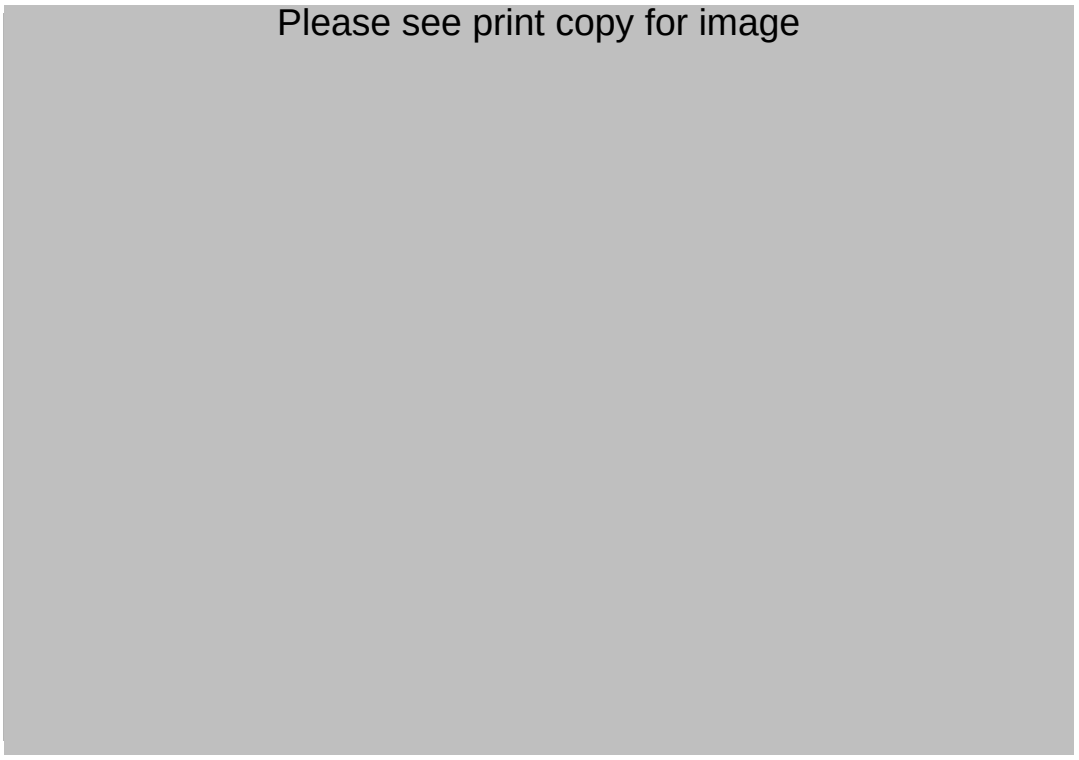

Fig.1. 20 Temperature dependence of the magnetoresistance (MR) for the $Sr_{2-x}Ho_xCoO_4$ system under a 7 T field [144].

Riza et al. also reported [144] that through a citrate synthesis and pyrolysis method, they had found that doping of B-sites in A_2BO_4 compounds greatly improved the electrical conductivity of the mixed conductor $La_2CoO_{4\pm\delta}$ and slightly increased the linear thermal expansion coefficient. They found that the doped oxides of the $La_2CoO_{4\pm\delta}$ system exhibited better properties than the equivalent perovskites. Therefore, they claimed that La_2CoO_4 compounds could be very good candidate materials for catalytic applications, energy production as solid oxide fuel cell electrodes, and numerous other electrochemical applications.

Other interesting and useful properties/applications were also found in tetragonal K_2NiF_4 structure compounds, for example, reports on their applications as catalysts for the partial oxidation of hydrocarbons, electrodes for solid oxide fuel cells, oxygen pumps, ceramic membranes for oxygen separation, and also as dielectric, ferroelectric, and piezoelectric materials. Due to their unusual amd interesting properties, researchers have been attracted to the extensive study of the strontium-doped $Ln_{2-x}Sr_xMO_4$ phases (Ln = rare earth ions; M = Mn, Ni, and Cu) [145 – 155]. With the exception of the $La_{2-x}Sr_xCoO_4$ compounds [156-160], other rare earth cobalt based K_2NiF_4 phases have received relatively little attention [33, 161].

Wang et al. reported their studies on the band structures and on the magnetic and magneto-transport properties of the high pressure phase of $Sr_{2-x}RE_xCoO_4$ (RE = Gd and Y, x = 0.1 - 0.5) compounds, which were synthesized by a high pressure and high temperature technique [1]. They found that as x increases, the magnetoresistance, MR $\{(\rho_H-\rho_0)/\rho_0\}$, increases up to -17% at 5 K and 7 T (Fig. 1.21), which is 2.5 times higher

than for the un-doped Sr_2CoO_4, although the ferromagnetic transition drops from 255 to 200 K for the Gd doping with x = 0.3 (Fig. 1.22).

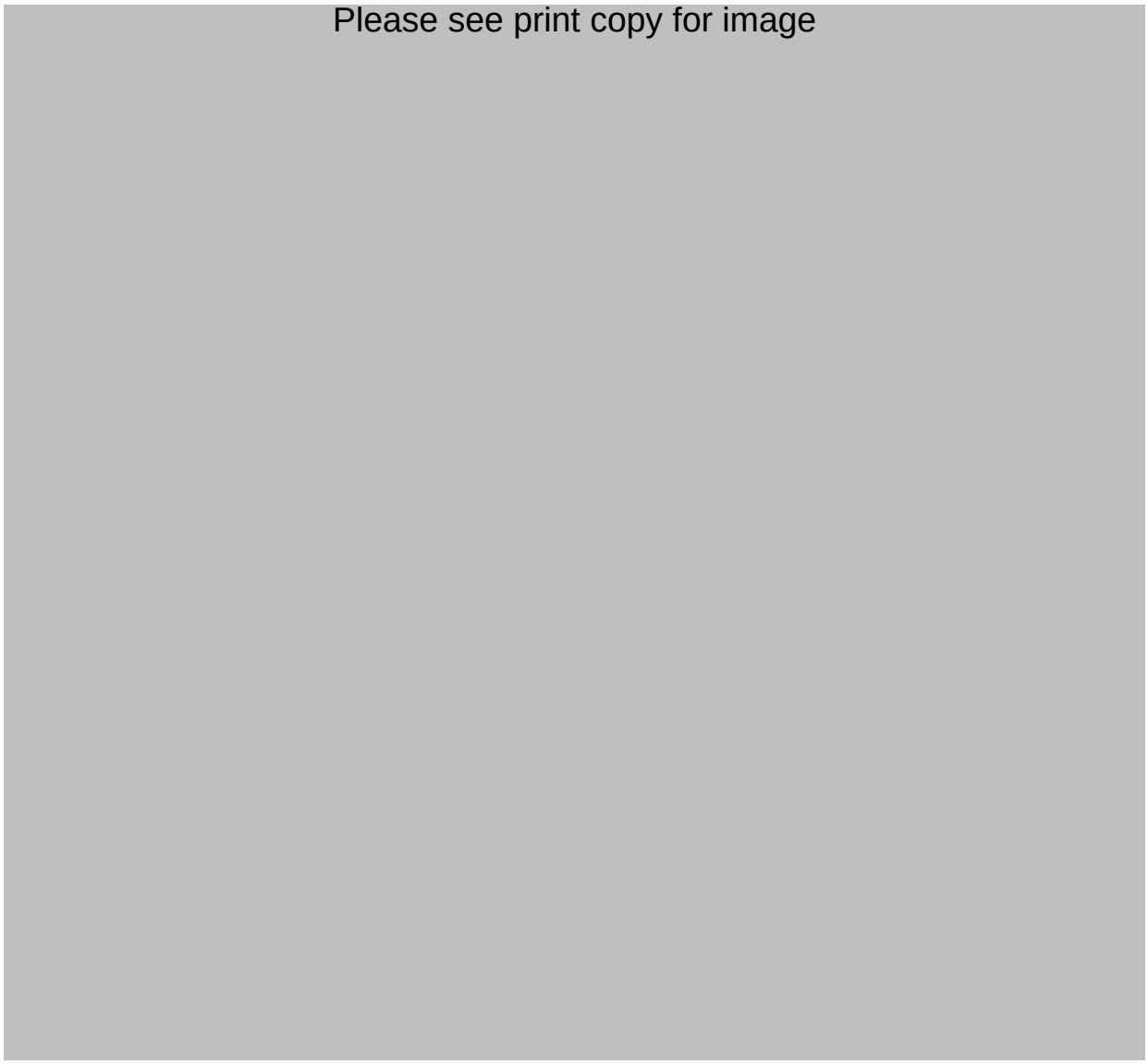

Fig.1. 21 Magnetoresistance (upper panel) and magnetization M (lower panel) for pure and Y or Gd doped Sr_2CoO_4 [1].

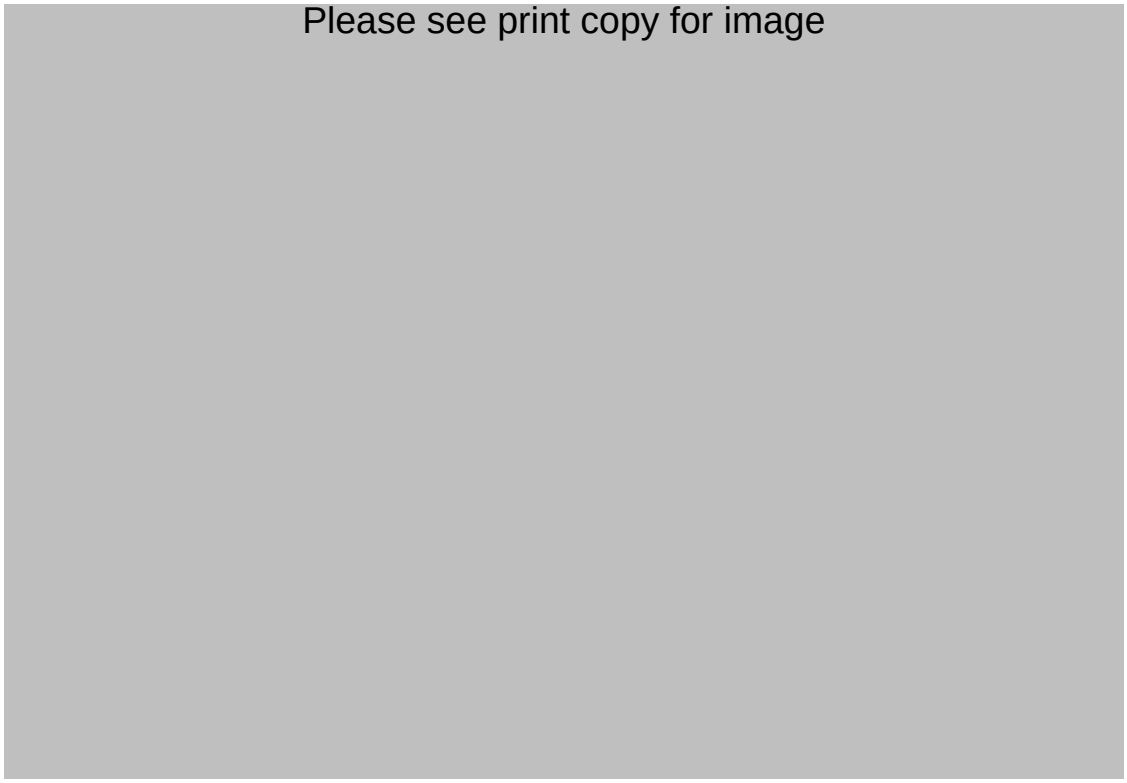

Fig.1. 22 Temperature dependence of the field-cooled magnetization for both Gd and Y doped Sr_2CoO_4 [1].

The saturation moments at low temperature are significantly enhanced for the Gd doped Sr_2CoO_4. Observation of a close correlation between resistance and field revealed a strong spin-dependent tunneling magnetoresistance.

First principles band structure calculations have indicated that high spin polarization is present for both the un-doped and the doped compounds, and that the *p* and *d* electrons from oxygen, cobalt, and gadolinium atoms all contribute to the high spin polarizations.

In conclusion, we have found that the goal of an industrially achievable and economically practical method of sample fabrication is desirable, and hence it was implemented in my PhD research study with the focus point at the polycrystalline

compound Sr_2CoO_4. This compound was studied via doping with various rare earth elements, and the corresponding changes and enhancements due to their corresponding doping states will be discussed later on in the thesis.

CHAPTER 2. EXPERIMENTAL PROCEDURES AND TECHNIQUES

2.1. SAMPLE PREPARATION

Various experimental procedures have been employed to fabricate and characterize the RE-doped Sr_2CoO_4 polycrystalline compounds. A sample preparation chart is provided in Fig. 2.1 to illustrate the process of sample preparation. The main method for the experiments on preparing samples was the solid state reaction approach. Polycrystalline samples of $Sr_{2-x}RE_xCoO_4$ ($0.25 \leq x \leq 1.5$) were synthesized by conventional solid-state reaction methods. Highly pure powders of RE oxides (Pr_6O_{11}, La_2O_3, Nd_2O_3, Gd_2O_3, and Eu_2O_3, all with 99.9% or above purities), $SrCO_3$, and Co_3O_4 were mixed in stoichiometric quantities accordingly. Pelletized samples were then sintered in air at 1000 - 1100 ^oC for 12 hours with several intermediate grindings. The intermediate grindings were necessary for thorough atomic-substitution to be realized in the samples. More specific details will be provided in subsequent chapters.

A list of the polycrystalline samples of $Sr_{2-x}RE_xCoO_4$ for which synthesis was attempted in this study is shown in Table 2.1.

Table 2. 1 Single phase polycrystalline samples $Sr_{2-x}RE_xCoO_4$ for which synthesis was attempted.

RE dopant	X values	Single phase with K_2NiF_4 structure
Pr	0, 0.5, 0.75, 1, 1.25, 1.5	x = 0.5- 1.25
Eu	0.25, 0.5, 0.75, 1, 1.25, 1.75	x = 0.75 - 1

La	0.5, 0.75, 1, 1.25	x = 0.75 – 1.25
Gd	0.5, 0.75, 1, 1.25	x = 0.5 – 1.25, all with small amount of impurity
Nd	0.5, 0.75, 1, 1.25	x = 0.5 – 1.25, all with small amount of impurity
Tm	0.5, 0.75, 1, 1.25	none
Yb	0.5, 0.75, 1.25, 1.5	none
Tb	0.5, 0.75, 1, 1.25	none

For the samples listed in Table 2.1, only those samples that can form single or near single K_2NiF_4 phase structure were investigated further. Consequently, I will only be presenting the studies of the samples that can form single (or close to single) K_2NiF_4 phase structures, namely, only the samples of $Sr_{2-x}RE_xCoO_4$ where RE = Pr, Eu, La, Gd, and Nd will be presented in this thesis.

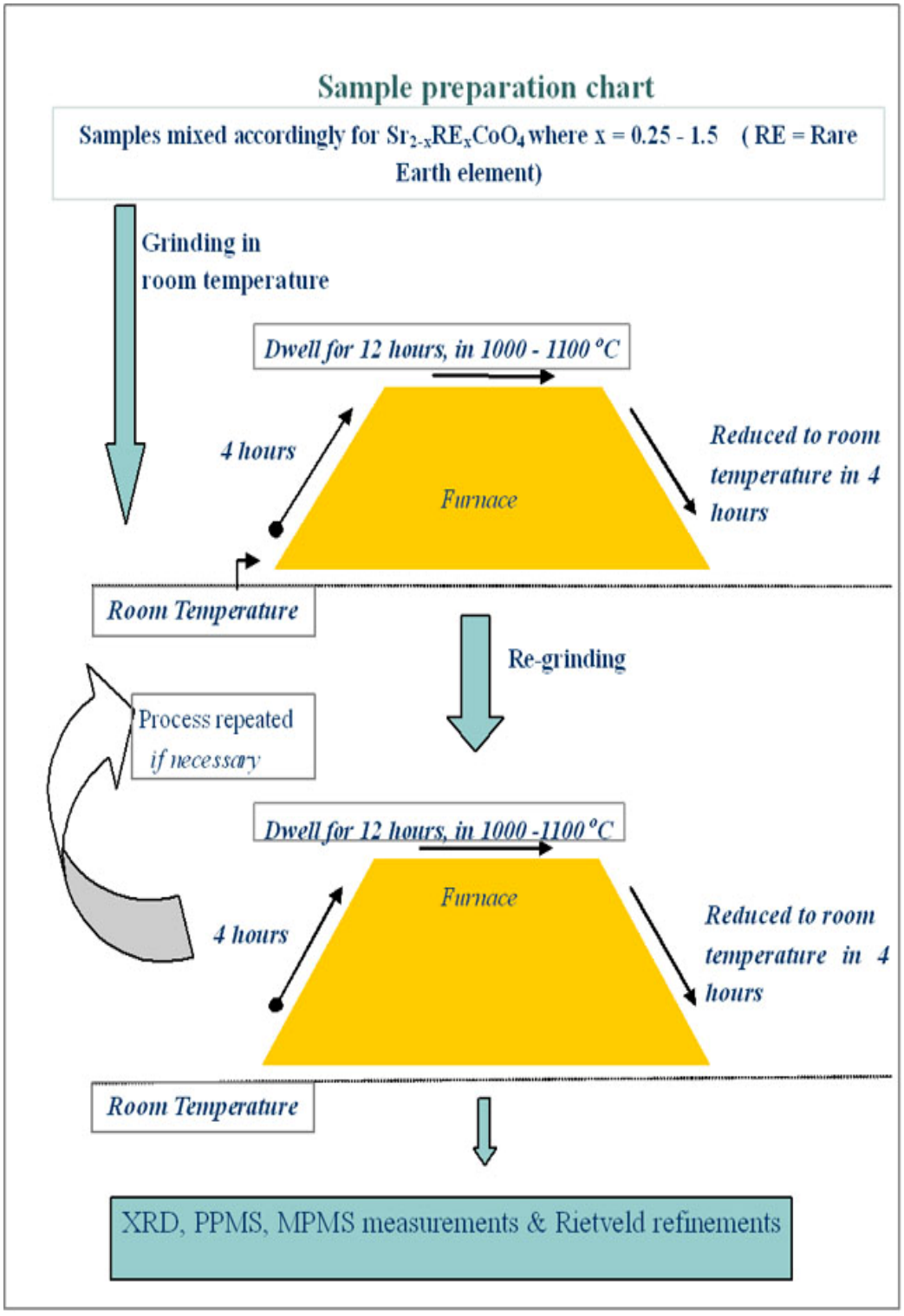

Fig. 2. 1 Sample preparation flow chart.

2.2 SAMPLE CHARACTERISATION

The phases and structures of the samples were studied using powder x-ray diffraction (XRD). The powder X-ray diffraction measurements were carried out on a Phillips PW1730 model diffractometer using Cu-Kα radiation, and the Rietveld refinement method was applied using the RIETICA program [119]. For the Rietveld refinement, the background was modeled with a 5-term polynomial; the peak shapes were described by a pseudo-Voigt function. A preferential orientation along the [001] direction was included in the refinement. The initial structural model for these refinements was taken from that of Sr_2TiO_4. The refined structures of these samples were found to be of the K_2NiF_4 type with space group $I4/mmm^2$.

Magnetic and transport properties were measured using a commercial Quantum Design magnetic properties measurement system (MPMS) and a Qunatum Design physical properties measurement system (PPMS) between 5 and 330 K in magnetic fields up to 8 Tesla. For some of the samples, the dielectric constant and loss were measured using a HP 4194A Impedance Analyzer in the frequency range from 200 up to 10 MHz.

2.3 THE PHYSICAL PROPERTIES MEASUREMENT SYSTEM (PPMS)

The basic PPMS measurement is accomplished by oscillating the sample near a detection (pick-up) coil and synchronously detecting the voltage induced. By using a compact gradiometer pick-up coil configuration, a relatively large oscillation amplitude (1-3 mm peak), and a frequency of 40 Hz, the system is able to resolve magnetization

changes of less than 10^{-6} emu at a data rate of 1 Hz. The Vibrating Sample Magnetometer (VSM) measurement system for the PPMS consists primarily of a VSM linear motor transport (head) for vibrating the sample, a coilset puck for detection, electronics for driving the linear motor transport and detecting the response from the pick-up coils, and a copy of the MultiVu software application for automation and control. The sample is attached to the end of a sample rod that is driven sinusoidally. The center of oscillation is positioned at the vertical center of a gradiometer pick-up coil. The precise position and amplitude of oscillation is controlled from the VSM motor module using an optical linear encoder signal that is read back from the VSM linear motor transport. The voltage induced in the pick-up coil is amplified and detected by a lock-in technique in the VSM detection module. The VSM detection module uses the position encoder signal as a reference for synchronous detection. This encoder signal is obtained from the VSM motor module, which interprets the raw encoder signals from the VSM linear motor transport. The VSM detection module detects the in-phase and quadrature-phase signals from the encoder and from the amplified voltage from the pick-up coil. These signals are averaged and sent over the controller area network (CAN) bus to the VSM application running on a personal computer (PC). The system is designed to be user-installable and compatible with existing PPMS systems. Like the other PPMS applications, the VSM is used only when required, leaving the PPMS to run other applications as needed. Since the VSM system is a completely self-contained measurement application, rather than one of the PPMS Base Systems, there are no other PPMS applications or options required for its use (source: www.qdusa.com).

The samples were also measured using the Four Point Probe technique [120], which uses four probes of four thin collinearly placed copper wires that are made to form

contacts with the sample. The sample is usually ground to a small uniform bar with a uniform rectangular cross-section. The four contact points were made by painting silver paste on the sample. The silver paste was then annealed and dried (to minimise contact resistance). Current (I) is made to flow between the two outer probes, and the voltage (V) is measured between the two inner probes (with a very small amount of current flow). The signal from the voltage wires is collected via a relay and measured with a multimeter, and the sample resistance is then recorded by a computer via an IEEE488 bus interface card.

The resistivity of the sample can be calculated using Eq. 2.1:

$$\rho = R(A/L) \qquad (2.1)$$

where R (Ω) is the measured resistance value, A (cm^2) is the cross sectional area of the sample, and L (cm) is the distance between the two inner voltage contacts.

2.4 THE MAGNETIC PROPERTIES MEASUREMENT SYSTEM (MPMS)

The Magnetic Properties Measurement System (MPMS) utilizes Superconducting Quantum Interference Device (SQUID) technology combined with patented enhancements, so that the MPMS sample magnetometer achieves high measurement sensitivity, dynamic range, and reproducibility. The modular MPMS design integrates a SQUID detection system, a precision temperature control unit residing in the bore of a high-field superconducting magnet, and a sophisticated computer operating system.

Data collection and analysis are under software control. The integrated Windows software allows full automation of all system parameters.

Magnetic measurements are critical in this study. DC magnetic measurements were needed to determine the equilibrium value of the magnetization of a sample, while in AC measurements, the AC moment of the sample is determined. The AC magnetic measurements give information on magnetization that can not be gathered in DC measurements. In this study, two types of magnetic measurements were performed. First, the dependence of the magnetization (M) of the sample on the temperature under zero magnetic field cooling (ZFC) and applied magnetic field cooling (FC) were measured. The applied magnetic field during FC measurements was usually set to 2000 Oe, from which the Curie or Neel temperature could be determined. Second, measurements of the magnetization (M) of the sample under changing applied magnetic field (H) at a certain temperature were taken, from which hysteresis effects and saturation magnetization can be accessed using the M-H curves for the sample. The range of applied magnetic field was from 0 to 6 T.

2.5 DIELECTRIC MEASUREMENTS

For some of the samples, the dielectric properties were measured using a HP 4194A Impedance/Gain-Phase Analyzer. This analyzer is able to perform a wide range of impedance measurements: 100 Hz to 40 MHz, 10mΩ to 100MΩ, 10 kHz to 100 MHz, Gain-phase measurements are in the range of : 10 Hz to 100 MHz, -107 dBm to +15

dBm, 0.1 dB res. It has flexible measurement, computation, and analysis capabilities on a color graphic display and is fully programmable.

CHAPTER 3. PR DOPED SR_2CoO_4 ($SR_{2-X}PR_XCoO_4$, X=0.25, 0.5, 0.75, 1, 1.25, 1.5)

3.1 INTRODUCTION

Polycrystalline samples of $Sr_{2-x}Pr_xCoO_4$ ($0.25 \leq x \leq 1.75$) were synthesized by the conventional solid-state reaction method, as mentioned earlier in Chapter 2. Highly pure powders of Pr_6O_{11}, $SrCO_3$, and Co_3O_4 were used as the starting materials. The phases and structures were studied using powder x-ray diffraction. The powder X-ray diffraction measurements were carried out on a Phillips PW1730 model diffractometer using Cu-Kα radiation, and the Rietveld refinement method was applied using the RIETICA program [119]. Magnetic and transport properties were measured using commercial Quantum Design magnetic and physical properties measurement systems (MPMS and PPMS) between 5 and 330 K in magnetic fields up to 8 Tesla. Dielectric constants and losses were measured using a HP 4194A Impedance Analyzer in the range from 200 up to 10 MHz.

At room temperature, most of these samples appear to be semiconductive, while samples with a small amount of Pr doping or non-doped $SrCoO_4$ samples were conductive.

3.2 STRUCTURAL PROPERTIES

XRD patterns for $Sr_{2-x}Pr_xCoO_4$, x = 0.25, 0.5, 0.75, 1, 1.25, 1.5 are shown in Fig. 3.1.

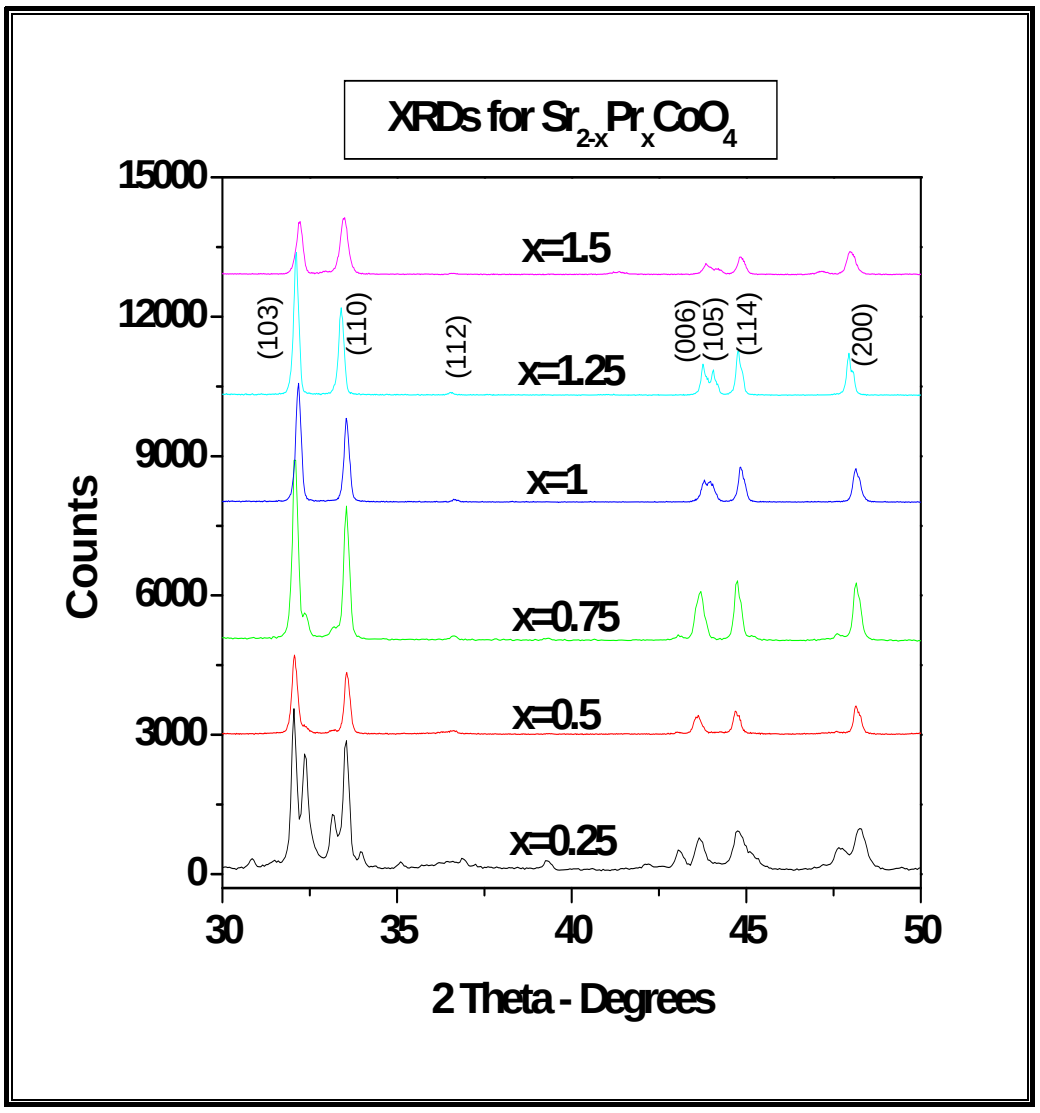

Fig. 3. 1 XRD patterns for $Sr_{2-x}Pr_xCoO_4$, where x = 0.25–1.5.

For x = 0.5 – 1.5, most of the peaks in the XRD patterns can be indexed based on a tetragonal unit cell similar to that of Sr_2TiO_4. Peaks from impurity phases are very weak or negligible in these specimens. For x = 0.25, impurity or multi-phases become obvious. It was observed that samples with $x \leq 0.5$ were not stable in air and tended to decompose within less than two hours for the x = 0.25 sample and within a few days for

the x = 0.5 sample. This is because of the high chemical reactivity of Co^{4+} with H_2O for those samples containing a high concentration of Co^{4+} ions. This phenomenon is also observed in other rare earth element doped Sr_2CoO_4 samples with low doping levels, as will be seen in other chapters.

The structure of Sr_2CoO_4 consists of corner-sharing CoO_6 octahedra with 2D CoO_2 planes separated by insulating double layers of SrO, as shown in Fig. 3.2 [33].

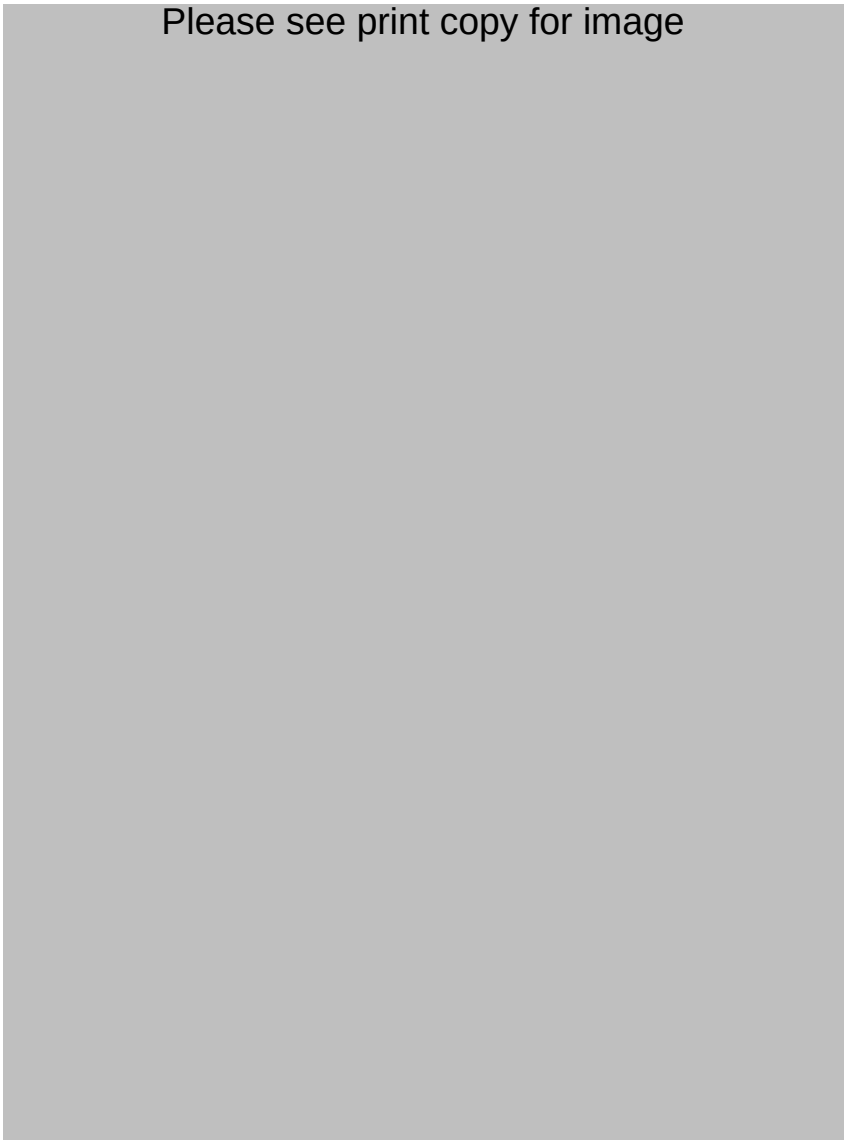

Fig. 3. 2 Crystal structure of Sr_2CoO_4 [33].

Rietveld refinement was carried out based on the XRD results for all the abovementioned samples. The observed (crosses), calculated (solid lines), and difference diffraction (bottom lines) profiles at 300 K for all the samples with x = 0.5, 0.75, 1, 1.25, and 1.5 are shown in Figures 3.3, 3.4, 3.5, 3.6, and 3.7, respectively. It can be seen that the calculated results match well with the experimental data. It should be pointed out that a few peaks which are not refined are from unknown impurities for the x = 1.5 sample.

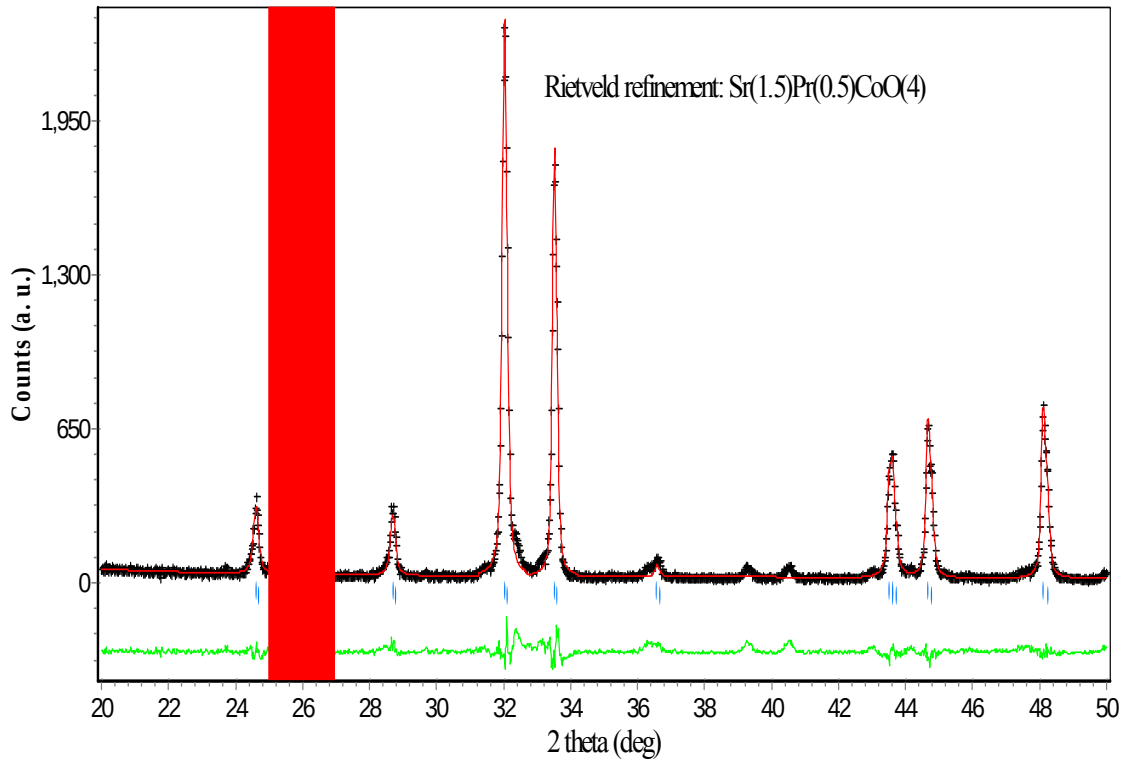

Fig. 3. 3 Rietveld refinement for $Sr_{1.5}Pr_{0.5}CoO_4$. The observed (crosses), calculated (solid line), and difference diffraction (bottom line) profiles at 300K. (Refinement factors: Rp=11.8%, RB=3.31%, with the blue-strip range ignored in the refinement for the x=0.5 sample).

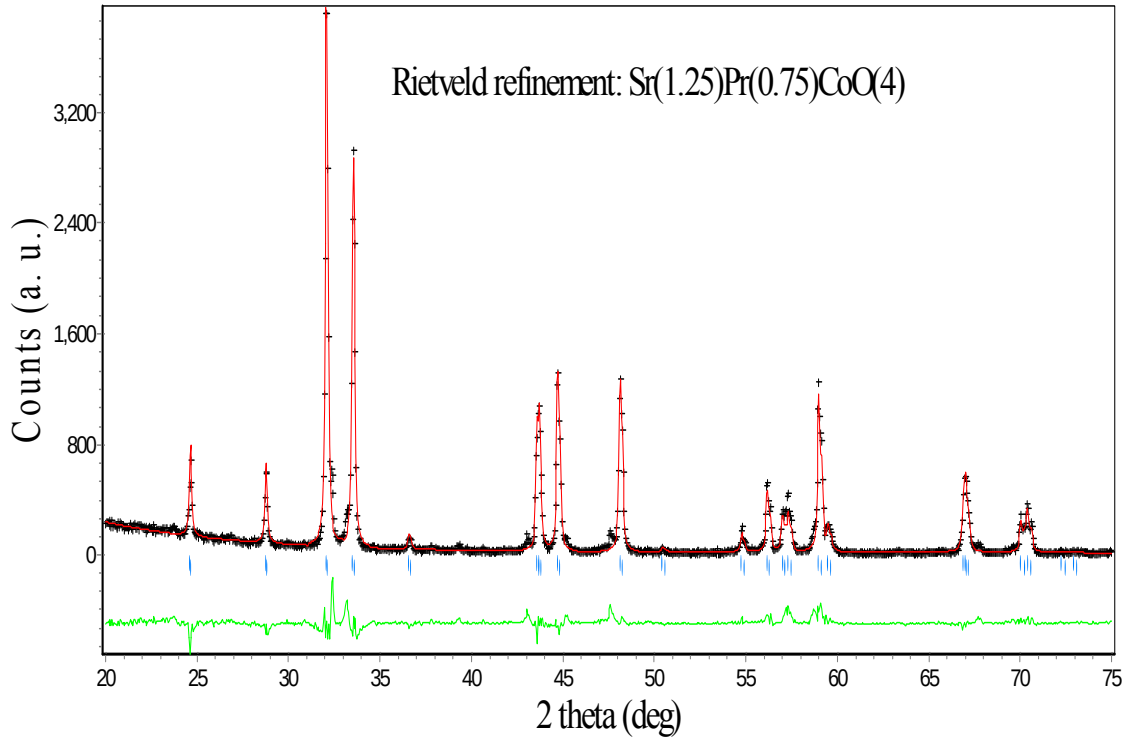

Fig. 3. 4 Rietveld refinement for $Sr_{1.25}Pr_{0.75}CoO_4$. The observed (crosses), calculated (solid line), and difference diffraction (bottom line) profiles at 300K (Refinement factors Rp=11.7%, RB=4.3% for the x=0.75 sample).

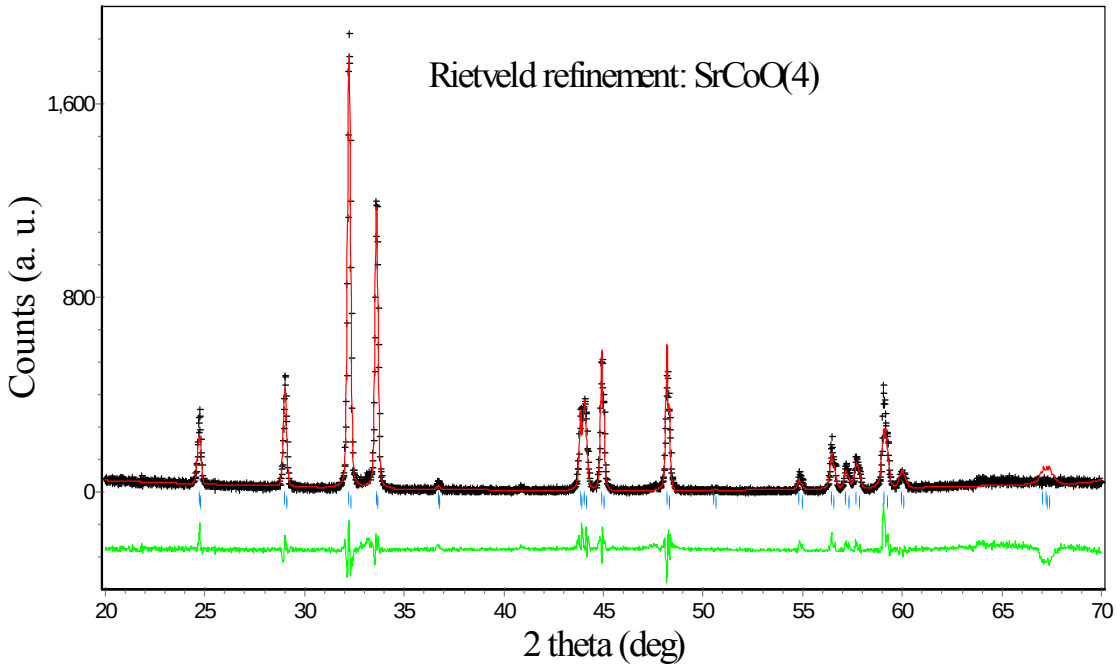

Fig. 3. 5 Rietveld refinement for $SrPrCoO_4$. The observed (crosses), calculated (solid line), and difference diffraction (bottom line) profiles at 300K (Refinement factors Rp=17.8%, RB=3.4% for the x=1 sample).

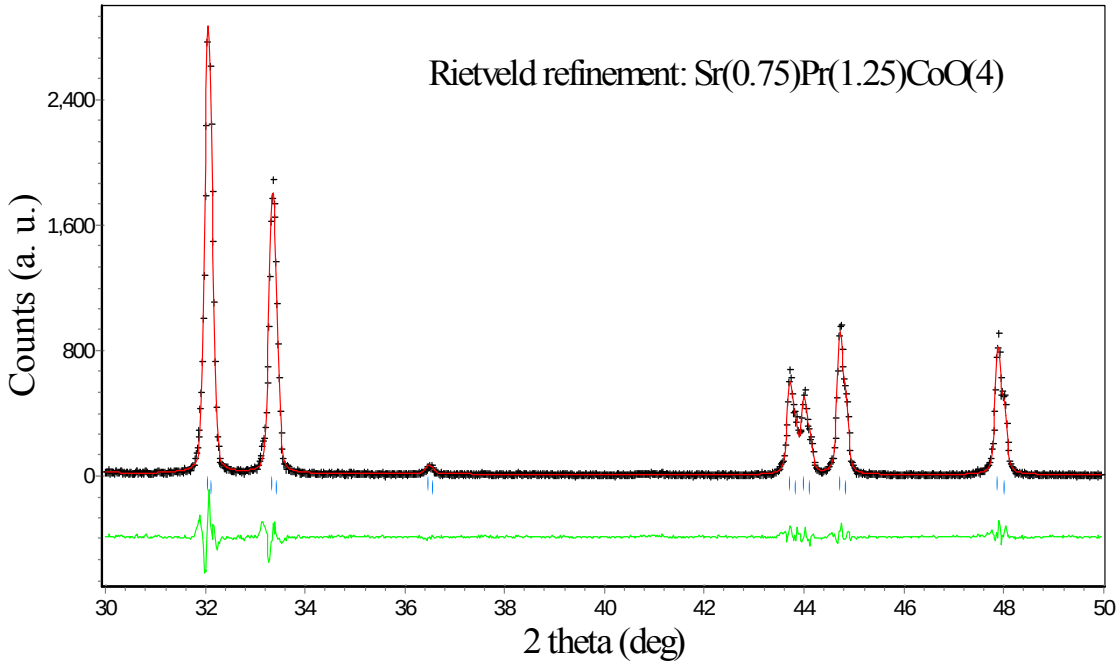

Fig. 3. 6 Rietveld refinement for $Sr_{0.75}Pr_{1.25}CoO_4$. The observed (crosses), calculated (solid line), & difference diffraction (bottom line) profiles at 300K (Refinement factors Rp=9.4%, RB=2.0% for the x=1.25 sample).

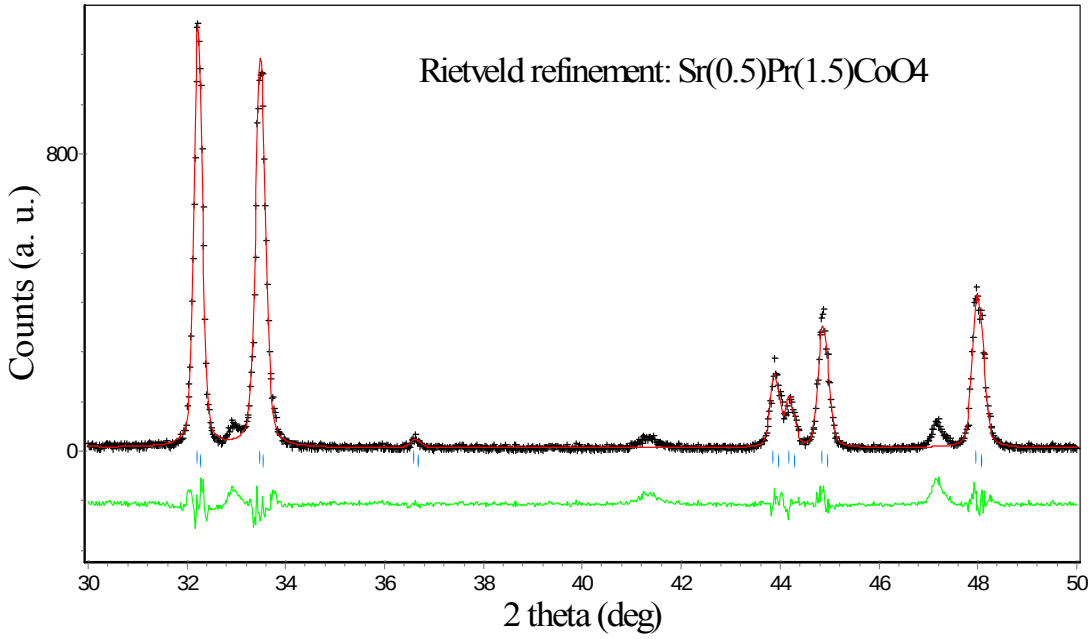

Fig. 3. 7 Rietveld refinement for $Sr_{0.5}Pr_{1.5}CoO_4$. The observed (crosses), calculated (solid line), & difference diffraction (bottom line) profiles at 300K (Refinement factors Rp=13.0%, RB=2.3% for the x=1. 5 sample).

The atomic parameters, isotropic temperature factors, Co-O bond lengths and unit cell volumes obtained from the refinement results are summarized in Tables 3.1 and 3.2.

Table 3.1 Crystal data for $Sr_{2-x}Pr_xCoO_4$ (x = 0.5, 0.75, 1, 1.25) - Space group: I4/mmm.

Atom	Samples	x	y	z	*B*iso[a]
Co	$Sr_{0.5}Pr_{1.5}CoO_4$	0	0	0	
	$Sr_{0.75}Pr_{1.25}CoO_4$	0	0	0	0.14
	$SrPrCoO_4$	0	0	0	0.14
	$Sr_{1.25}Pr_{0.75}CoO_4$	0	0	0	0.14
	$Sr_{1.5}Pr_{0.5}CoO_4$	0	0	0	0.14

Sr/Pr	$Sr_{0.5}Pr_{1.5}CoO_4$	0	0	0.3605	
	$Sr_{0.75}Pr_{1.25}CoO_4$	0	0	0.3605	0.14(Pr) 0.14(Sr)
	$SrPrCoO_4$	0	0	0.3605	0.14(Pr) 0.184(Sr)
	$Sr_{1.25}Pr_{0.75}CoO_4$	0	0	0.3605	0.09(Pr) 0.18(Sr)
	$Sr_{1.5}Pr_{0.5}CoO_4$	0	0	0.3605	0.07(Pr) 0.21(Sr)
O (1)	$Sr_{0.5}Pr_{1.5}CoO_4$	0	0.5	0	
	$Sr_{0.75}Pr_{1.25}CoO_4$	0	0.5	0	0.32
	$SrPrCoO_4$	0	0.5	0	0.29
	$Sr_{1.25}Pr_{0.75}CoO_4$	0	0.5	0	0.30
	$Sr_{1.5}Pr_{0.5}CoO_4$	0	0.5	0	0.29
O (2)	$Sr_{0.5}Pr_{1.5}CoO_4$	0	0	0.1701	
	$Sr_{0.75}Pr_{1.25}CoO_4$	0	0	0.1618	0.23
	$SrPrCoO_4$	0	0	0.1597	0.29
	$Sr_{1.25}Pr_{0.75}CoO_4$	0	0	0.1619	0.27
	$Sr_{1.5}Pr_{0.5}CoO_4$	0	0	0.1610	0.25

[a] *B*iso is an isotropic thermal parameter.

Table 3.2 Crystal data for $Sr_{2-x}Pr_xCoO_4$ (x=0.5, 0.75, 1, 1.25) - Space group: I4/mmm.

Samples	a(Å)	c(Å)	Co-O(1) (Å)	Co-O(2) (Å)	Cell Volume ($Å^3$)
$Sr_{0.5}Pr_{1.5}CoO_4$	3.8008	12.341	2.0989	1.9004	
$Sr_{0.75}Pr_{1.25}CoO_4$	3.79351	12.32776	2.0493	1.8968	177.51
$SrPrCoO_4$	3.78155	12.34973	1.9212	1.8908	176.60
$Sr_{1.25}Pr_{0.75}CoO_4$	3.78058	12.42291	2.0192	1.8903	177.42
$Sr_{1.5}Pr_{0.5}CoO_4$	3.7824	12.4518	1.9999	1.8912	178.14

From Table 1, we can see that the atomic position for Sr/Pr is not sensitive to the Pr doping level. However, the O2 position does vary with the doping level, although the variations are not significant. This reflects the change in the bond length of Co-O(2). The bond length of the Co-O bonds vs. doping level is plotted in Fig. 3.10.

We can see from Table 2 that Pr doping reduces the *c* parameter fairly consistently, while the *a* parameter is not significantly changed. Lattice parameter *a* increases gradually with increasing x for x > 0.5. However, lattice parameter *c* decreases with increasing x, until x reaches 1.5. The trends in both the *a* and *c* parameters can be more clearly seen in the plots of x vs. lattice parameter as shown in Figs. 3.8 and 3.9. The *a* parameter for the x > 1 samples increases more quickly compared to the samples with x

< 1. However, the values of lattice parameter *c* exhibit an opposite trend. Generally speaking, the changes in the *a* parameter are much smaller compared to the changes observed in the *c* parameter, in regards to the doping level. The maximum change in the *a* parameter is about 0.02 Å, while it is about 0.14 Å for the *c* parameter.

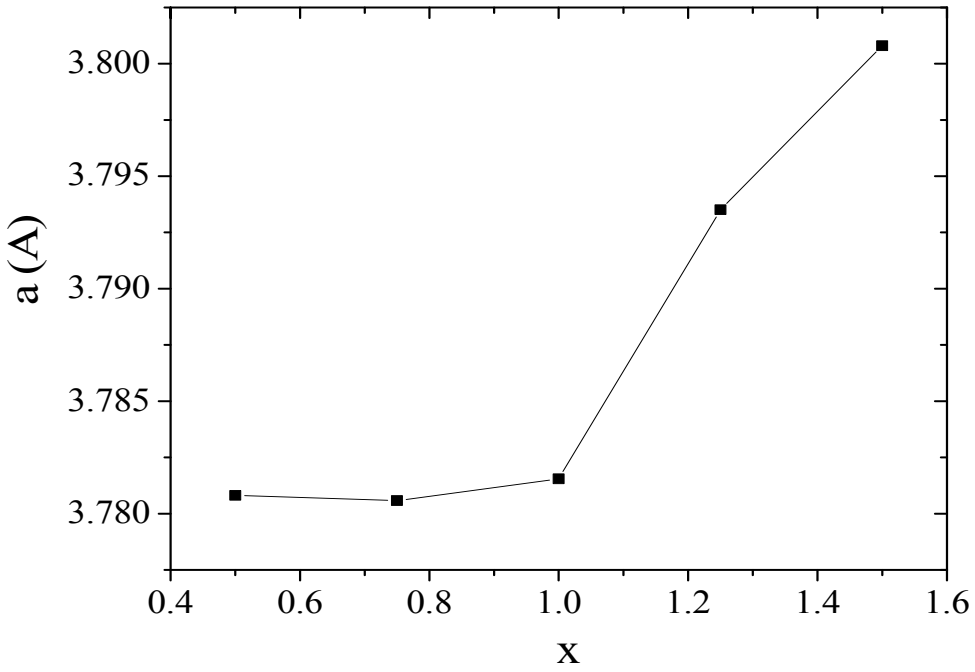

Fig. 3. 8 Lattice parameter a vs. x for $Sr_{2-x}Pr_xCoO_4$.

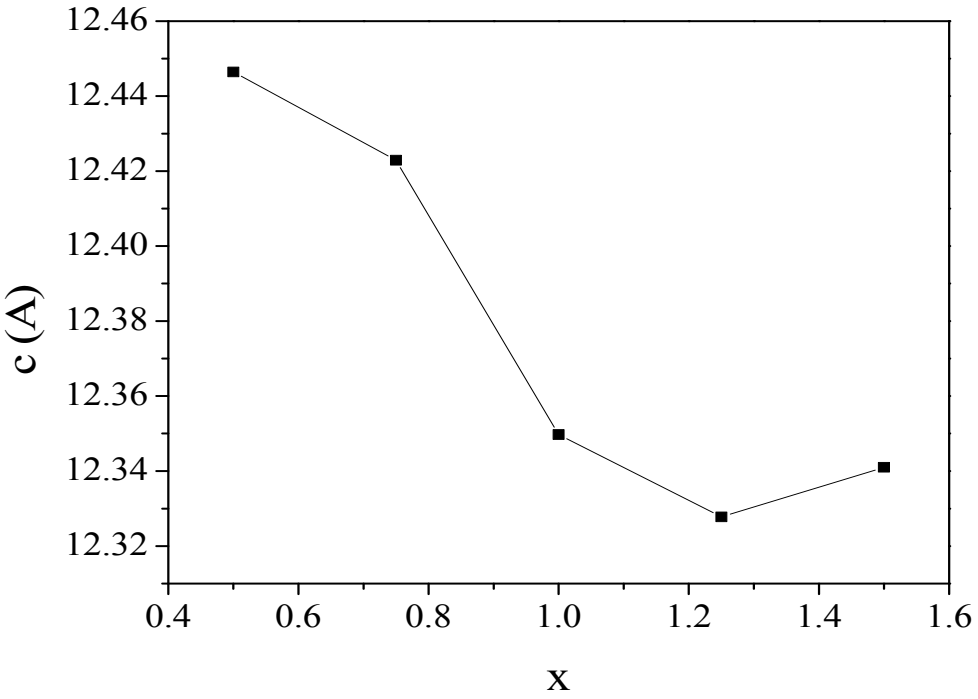

Fig. 3. 9 Lattice parameter c vs. x for $Sr_{2-x}Pr_xCoO_4$.

The unit cell volume as a function of doping level x is shown in Fig. 3.11. A closer comparison between the data for the Co-O(1) bond length (Fig. 3.10) and the cell volume gives a similar trend of change against the doping level: both cell volume and Co-O(1) values are gradually reduced as the Pr content increases from x = 0.5 to 1; as the Pr content further increases, the corresponding values start to increase. However, the in-plane Co-O(2) bond length increases very slightly as x increases. These results suggest that the Pr substitution for Sr mainly affects the out-of-plane Co-O(1) bond lengths.

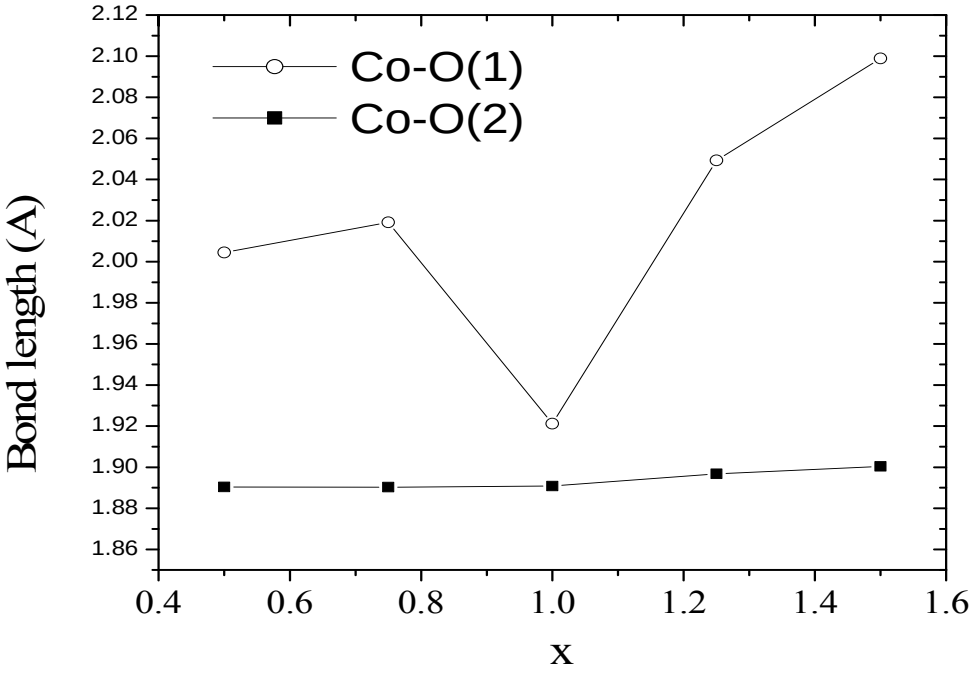

Fig. 3. 10 The Co-O bond length vs. x for $Sr_{2-x}Pr_xCoO_4$.

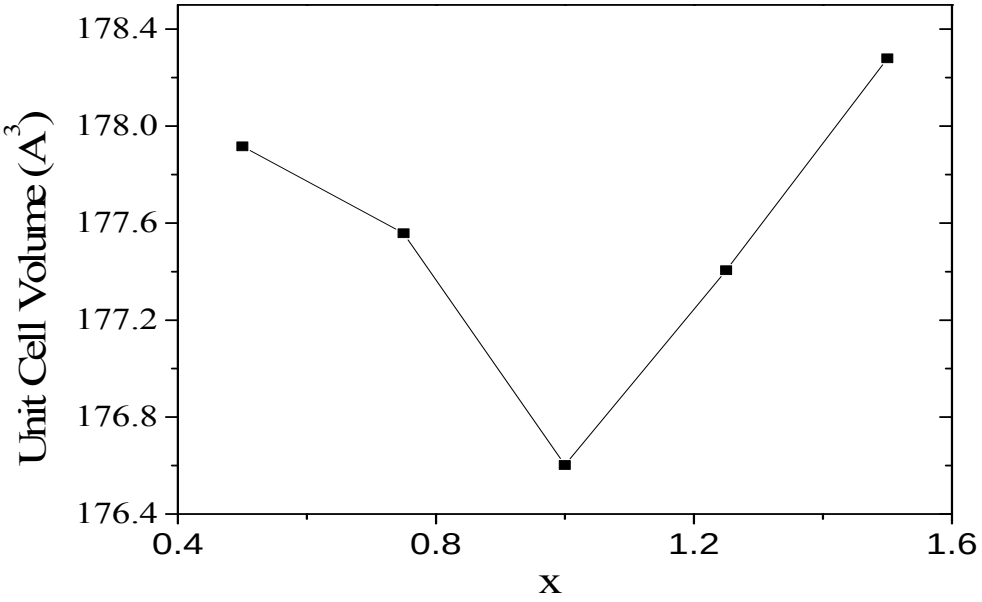

Fig. 3. 11 The unit cell volume vs. x for $Sr_{2-x}Pr_xCoO_4$.

The reduction of lattice parameter *c* and the unit cell volume by Pr doping for the $x \leq 1$ samples is in agreement with the fact that the Pr^{3+} ion has a smaller size (radius 1.06 Å) than that of the Sr^{2+} (radius 1.31 Å) ion. However, with further increases in the Pr doping level, both lattice parameter *a* and the unit cell volume increase instead of decreasing. As the Pr content increases, the valence of the Co ion is gradually reduced from 4+ to 3+ and becomes entirely 3+ when x reaches 1. It will be further reduced to a mixed state of Co^{3+} (radius 0.55 Å) and Co^{2+} (radius 0.73 Å) as a result of higher Pr doping content. The Co ion's size increases as its valence is reduced from 4+ (radius 0.53 Å) to 2+ (radius 0.73 Å). The increase in the atomic size of the Co ions is believed to be quicker than the decrease in the average size of the Sr and Pr ions for $x > 1$, so as a result, the unit cell volume increases.

From Table 3.2, we can see that the value for the in-plane Co-O(2) bond length is almost the same, around 1.89 Å, for all the doping levels. However, for all samples, the out-of-plane Co-O(1) bond length value is greater than 1.92 Å, and it increases with x, except at $x = 1$. These results indicate that the Pr doping causes distortion of the CoO_6 octahedron with elongation along the *c*-axis (the Co-O(1) direction).

3.4 TRANSPORT PROPERTIES

The temperature dependence of the resistivity for the $x = 1.25$ sample is shown in Fig. 3.12. It can be seen that this sample displays semiconductive behaviour. By measuring the resistance of all the samples, we have found that the resistivities of these samples increase with increasing doping levels of Pr.

The electrical resistivity for this compound can be well fitted by the equation $\rho = \rho_\infty \exp(T_0/T)^{1/3}$ over our measurement range, as shown in Fig. 3.13. This suggests the 2D variable-range hopping (VRH) mechanism [121]. For temperatures any lower than 165 K (where $(1/T)^{1/3} > 0.175$), the compound's resistivity becomes so large that it is out of the measurable range of our equipment.

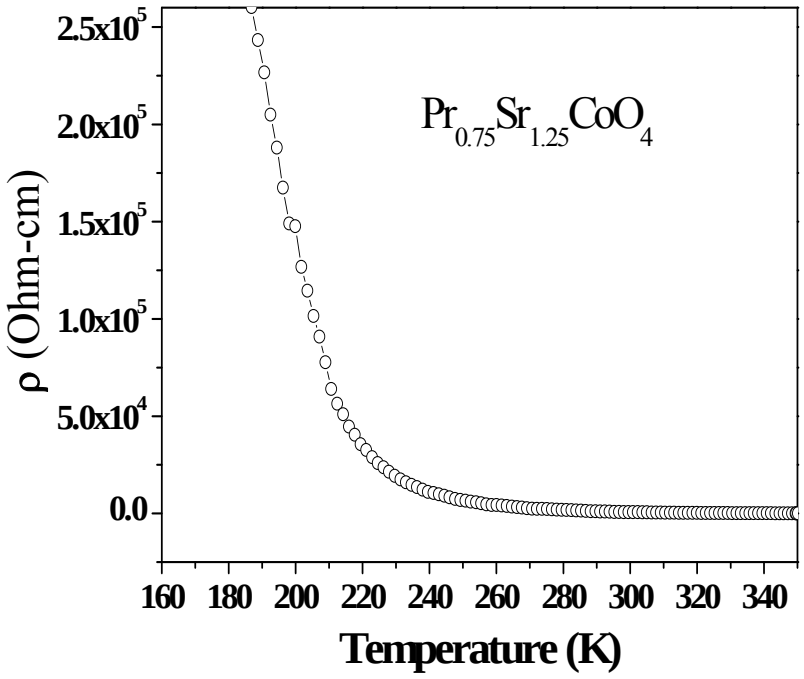

Fig. 3. 12 Resistance vs. temperature for $S_{r1.25}Pr_{0.75}CoO_4$.

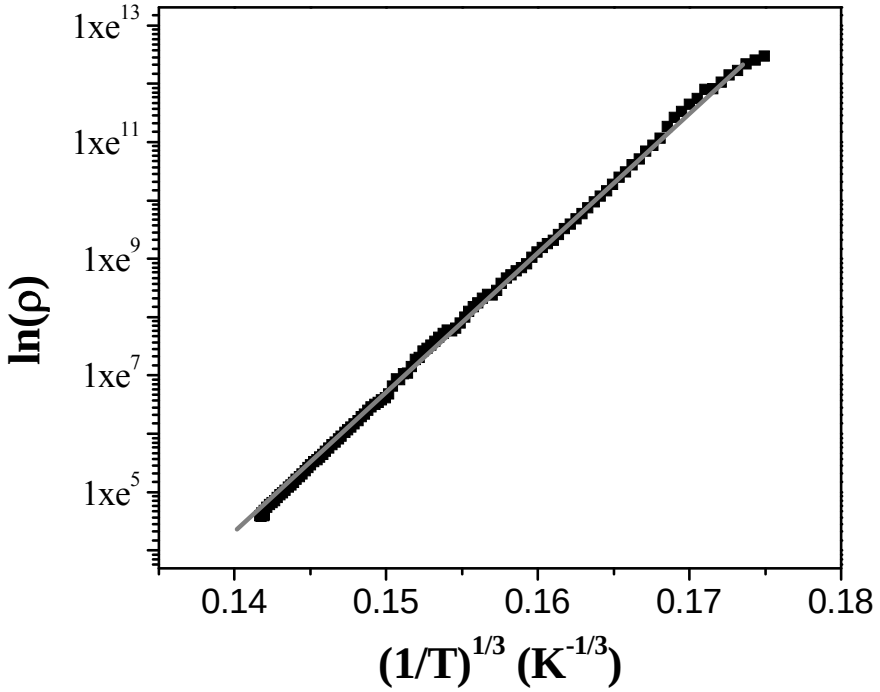

Fig. 3. 13 ρ vs. exp(1/T)$^{1/3}$ for $Sr_{1.25}Pr_{0.75}CoO_4$. Straight line is a linear fitting to the 2D VRH model.

3.5 MAGNETIZATION PROPERTIES

The temperature dependence of the field cooled and zero field cooled dc magnetization measured at 0.2 Tesla for all the samples is shown in Fig. 3.14. An enlargement of the temperature dependence of the $Sr_{2-x}Pr_xCoO_4$ samples' magnetization in the low temperature range is shown in Fig. 3.15. Generally, the Pr doping changes the system from ferromagnetic to paramagnetic. The magnetization decreases with increasing Pr doping levels. We found that ferromagnetic behavior in these samples is obvious for both the x = 0.25 and 0.5 samples, with a T_C around 200 K. As x increases, the ferromagnetism starts to weaken. For the samples with x > 0.75, paramagnetic behavior is dominant over a wide range of temperatures.

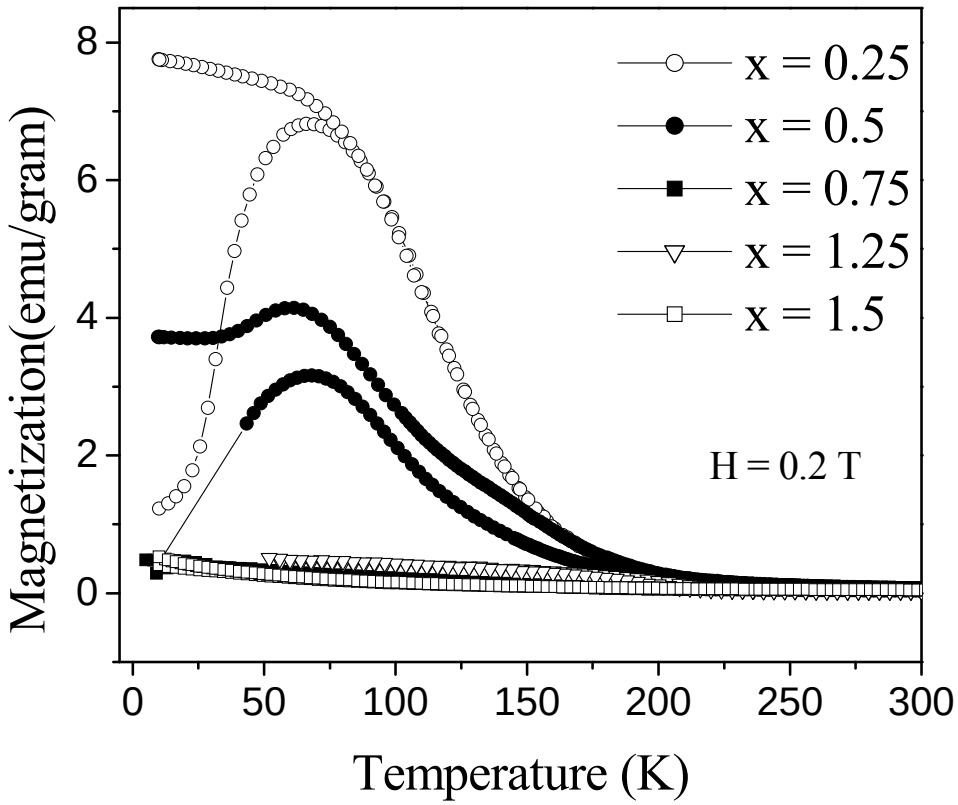

Fig. 3. 14 The temperature dependence from 5 K to 300 K of the magnetization of the $Sr_{2-x}Pr_xCoO_4$ samples with x = 0.25, 0.5, 0.75, 1, 1.25, measured in a magnetic field of 0.2 Tesla.

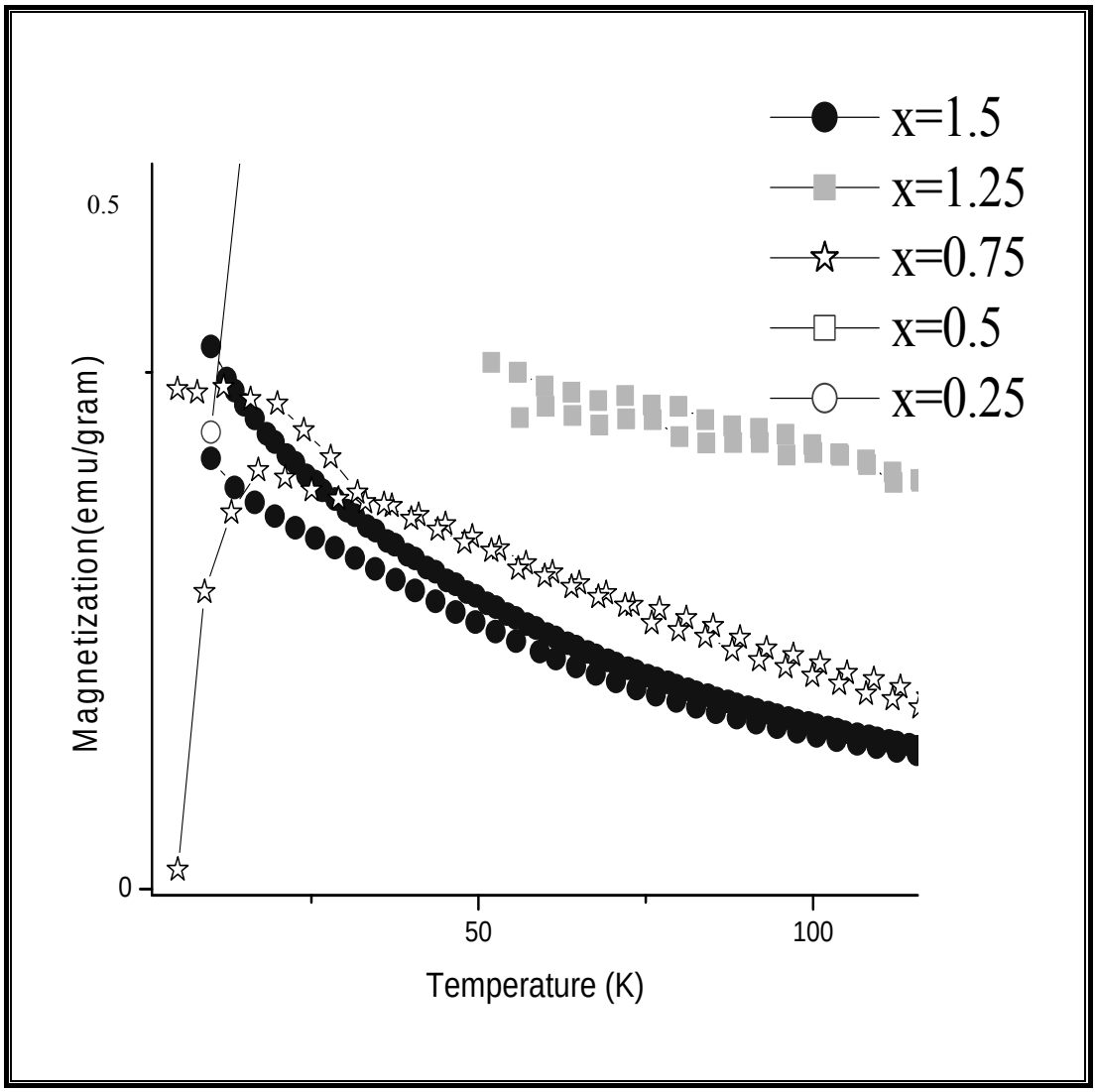

Fig. 3. 15 Temperature dependence of the $Sr_{2-x}Pr_xCoO_4$ samples' magnetization in the low temperature range.

Fig. 3.16 shows the inverse susceptibility (χ^{-1}) vs. temperature for $Sr_{2-x}Pr_xCoO_4$. It reveals a ferromagnetic transition for the sample with x = 1.25, with a T_C of about 230 K (at the point where the concavity of the graph changes). This indicates that a short range ferromagnetic interaction starts at this transition temperature. A similar transition is observed at around 180 K for both the x = 1.5 and the x = 0.75 samples. The Weiss temperatures obtained by fitting the Curie-Weiss linear law are 150, 130, and 75 K for the x = 1.25, 0.75, and 0.5 samples, respectively.

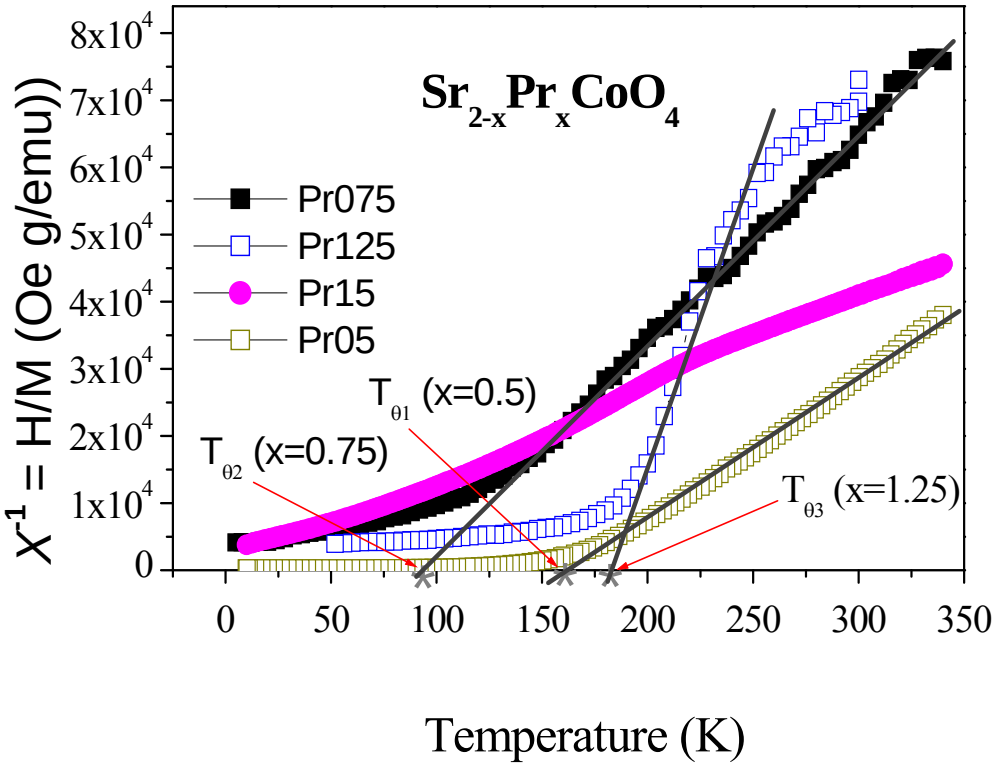

Fig. 3. 16 Temperature dependence of the inverse molar susceptibility (χ^{-1}) for $Sr_{2-x}Pr_xCoO_4$, measured at a magnetic field of 2 kOe. The straight lines show the relevant Curie-Weiss law fittings.

Fig. 3.17 shows the MH loops up to 50000 Oe for the x = 0.5 and 0.75 samples measured at 5 K. These MH loops further confirm the typical ferromagnetic behavior observed for the x = 0.5 sample in Fig. 2.14. The magnetic moment at 5 T and 5 K is about 16 emu/gram, and a coercive field of about 1 T exists for the x = 0.5 sample. However, for the x = 0.75 sample, the hysteretic behavior is drastically reduced compared to the x = 0.5 sample.

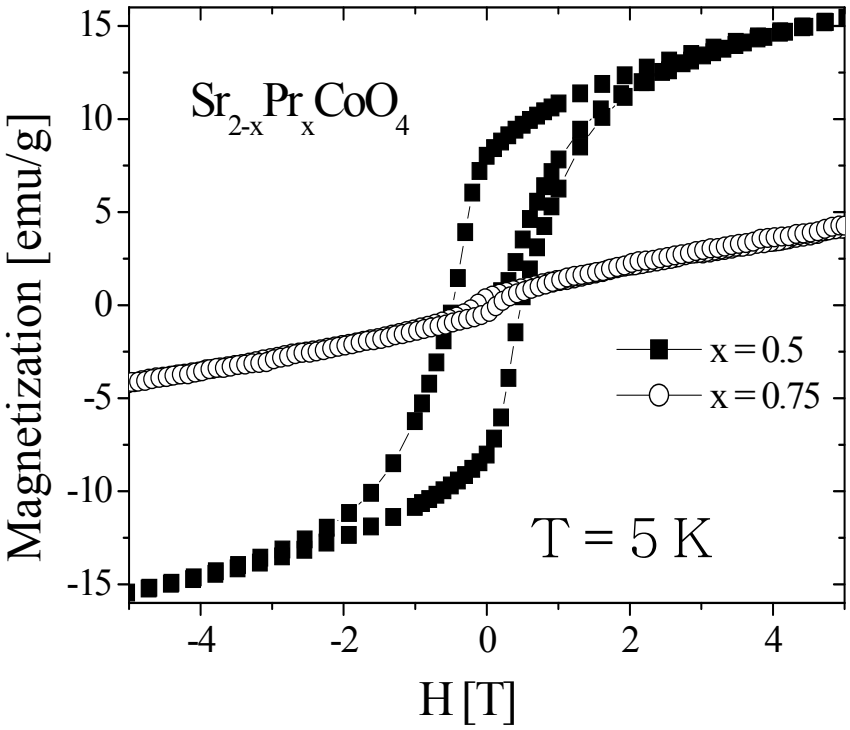

Fig. 3. 17 Magnetic hysteresis loops for $Pr_xSr_{2-x}CoO_4$.

3.6 DIELECTRIC PROPERTIES

The dielectric properties in the frequency range of 100 to 1.5×10^7 Hz were measured for samples with x = 1 and 1.25 at room temperature, as shown in Figs. 3.18 and 3.19. The values of the dielectric constant (ε) are over 2000 at low frequencies of less than 1 kHz (not shown here) and gradually decrease with increasing frequency. The ε of the x = 1 sample is greater than that of the x = 0.75 sample, indicating that the charge induced capacitance in the x = 1 sample is greater than that of the x = 0.75 sample, in agreement with the trend of their resistivity measurements. ε remains above 50 at frequencies up to 10 MHz for the x = 1 sample, in contrast to about 10 at 10 MHz for the x = 0.75 sample. The dielectric loss, δ, drops down to 2 - 3 at a frequency of 1 MHz and then increases

very smoothly with increasing frequency up to 10 MHz, indicating that an extra conducting mechanism may be responsible.

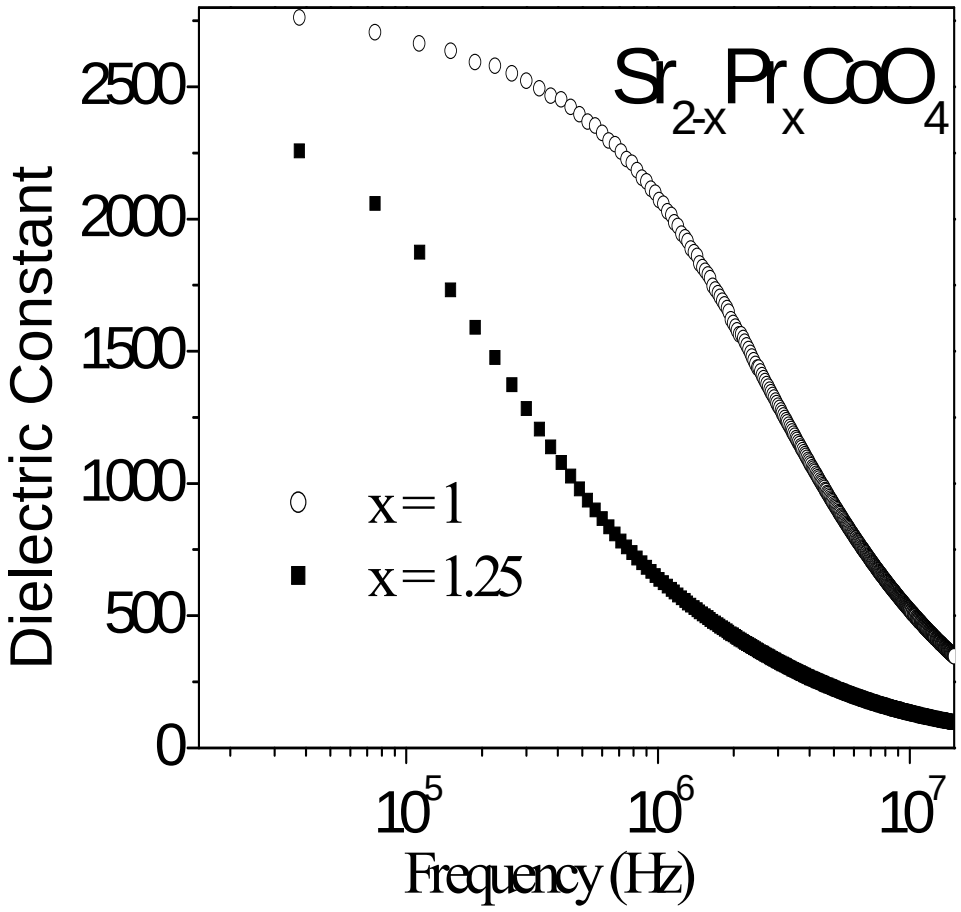

Fig. 3. 18 Frequency dependence of the dielectric constant for $Sr_{2-x}Pr_xCoO_4$ (x = 1, 1.25) at room temperature.

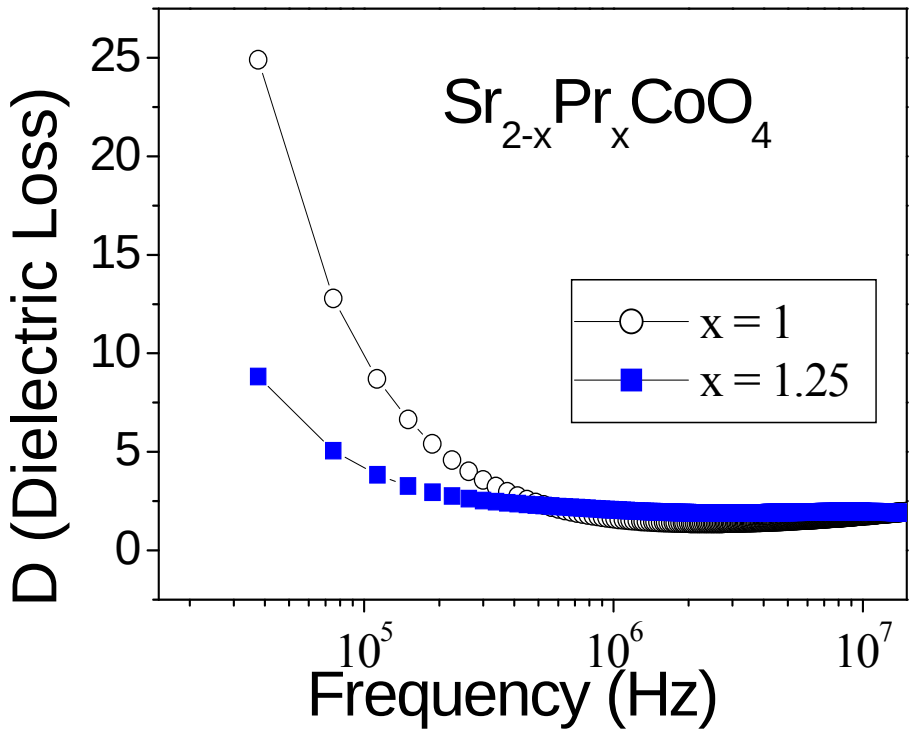

Fig. 3. 19 Frequency dependence of the dielectric loss for $Sr_{2-x}Pr_xCoO_4$ (x = 1, 1.25) at room temperature.

3.7 SUMMARY

It was found that the Pr doped $Sr_{2-x}Pr_xCoO_4$ samples crystallized in K_2NiF_4-type structures with space group I4/mmm. Lattice parameter *c* decreased with Pr doping level x. The Curie temperature (T_C) was found to be 200 K for $Sr_{1.5}Pr_{0.5}CoO_4$. The resistivities were found to increase with doping level x. A large coercive field of about 1 T was found for the sample with x = 0.75. The x = 1.25 sample shows semiconductor-like behavior in terms of resistivity in the low temperature range, and its conductivity can be described, based on the Variable Range Hopping mechanism. A large dielectric constant above 2000 is observed at 1 kHz, which may be caused by free charge effects.

CHAPTER 4. LA DOPED Sr_2CoO_4 ($Sr_{2-x}La_xCoO_4$, x = 0.5, 0.75, 1, 1.25)

4.1 INTRODUCTION

Ferromagnetic semiconducting behavior has been observed in $La_{1-x}Sr_{1+x}CoO_4$ compounds fabricated under ambient pressure in O_2 [113, 123]. With increasing Sr content, the system changes from antiferromagnetic insulator to ferromagnetic semiconductor. The Curie temperature is about 200 K for x = 1.25, as estimated from measurements of the temperature dependence of the magnetization [123], but $LaSrCoO_4$ seems to be a paramagnetic semiconductor. In this work, we report our investigations into the structural, the magnetic, and the magnetotransport properties of La doped Sr_2CoO_4 fabricated by the conventional solid state reaction method, and compare our results with what has been previously reported.

4.2 EXPERIMENTAL

Polycrystalline samples of $Sr_{2-x}La_xCoO_4$ (x = 0.5, 0.75, 1, 1.25) were synthesized by a conventional solid-state reaction method, as described in Chapter 2. Powders of La_2O_3, $SrCO_3$, and Co_3O_4 with high purity were used as starting materials. The phases and structures of the resulting samples at room temperature were studied using x-ray powder diffraction (XRD). Structure refinements were carried out by the Rietveld method using the RIETICA program. Magnetic and electrical transport properties were investigated using commercial Quantum Design Magnetic and Physical Properties Measurement Systems (MPMS and PPMS) in a temperature range from 5 to 330 K, and in magnetic fields up to 8 Tesla. Band structures were studied by first principles calculations using

the CASTEP package [122]. We adopted the standard generalized gradient approximation (GGA), with the Perdew-Burke-Ernzerhof functional.

4.3 STRUCTURAL PROPERTIES

The XRD patterns for samples with x = 0.75, 1, and 1.25 are shown in Fig. 4.1. From the XRD results, we found that samples with x = 1 and 1.25 are single Sr_2CoO_4 phase, while the x = 0.75 sample is almost single phase with a tiny amount of an unknown impurity made evident by a small peak between the two tallest peaks. The x = 0.5 sample is a mixture of Sr_2CoO_4 phase and $Sr_3Co_2O_7$ phase (not shown here). However, a single phase sample with x = 0.5 can be successfully obtained by using different starting materials [113, 124].

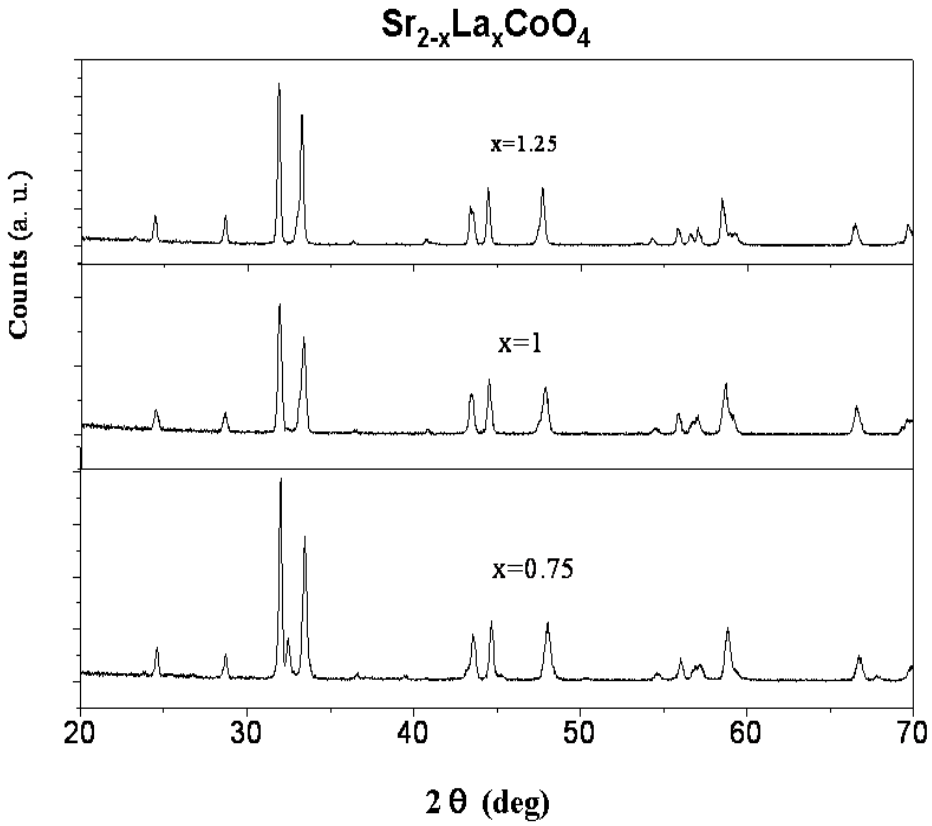

Fig. 4. 1 XRD patterns of $Sr_{2-x}La_xCoO_4$ with x = 0.75, 1, 1.25

Rietveld refinement was carried out based on the XRD results for the samples with x = 0.75, 1, and 1.25, which are shown in Figs. 4.2, 4.3, and 4.4, respectively. The observed (crosses), calculated (solid lines), and difference diffraction (bottom lines) profiles are plotted in each figure. It can be seen that the calculated results match well with the experimental data.

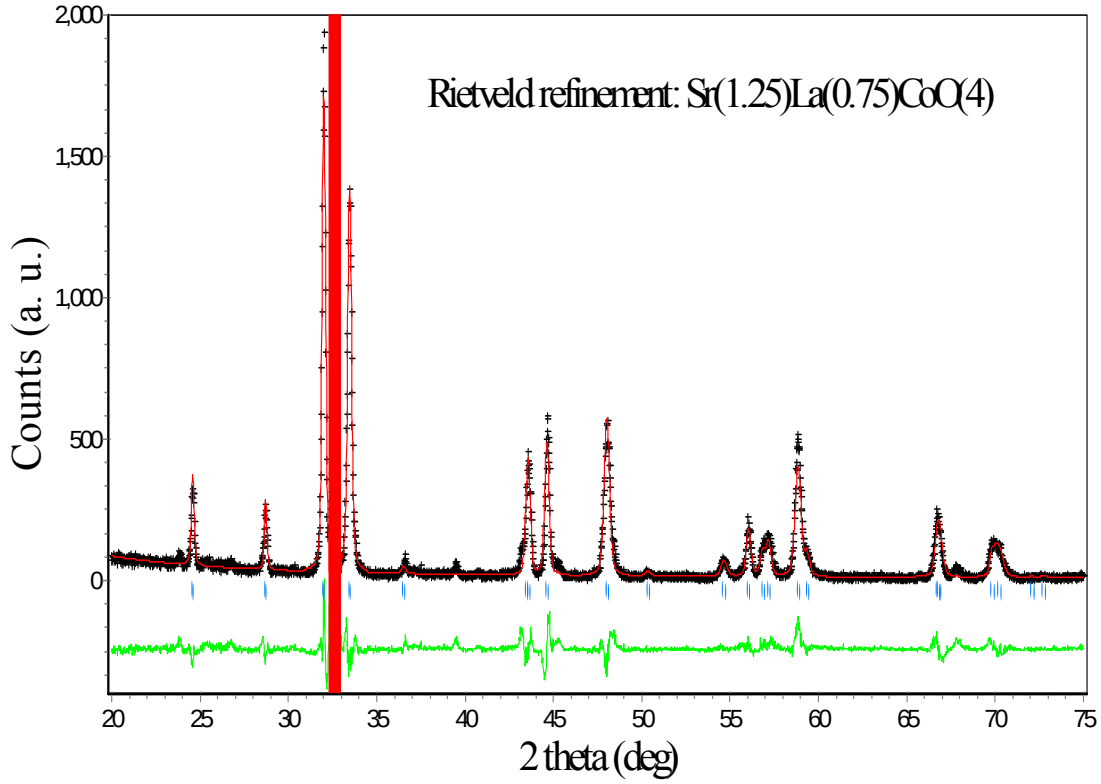

Fig. 4. 2 Rietveld refinement for $Sr_{1.25}La_{0.75}CoO_4$. The observed (crosses), calculated (solid line) and difference (bottom line) profiles at 300K for the x=0.75 sample (refinement factors Rp=14.8%, Rb=2.9%; blue-strip range was ignored in refinement).

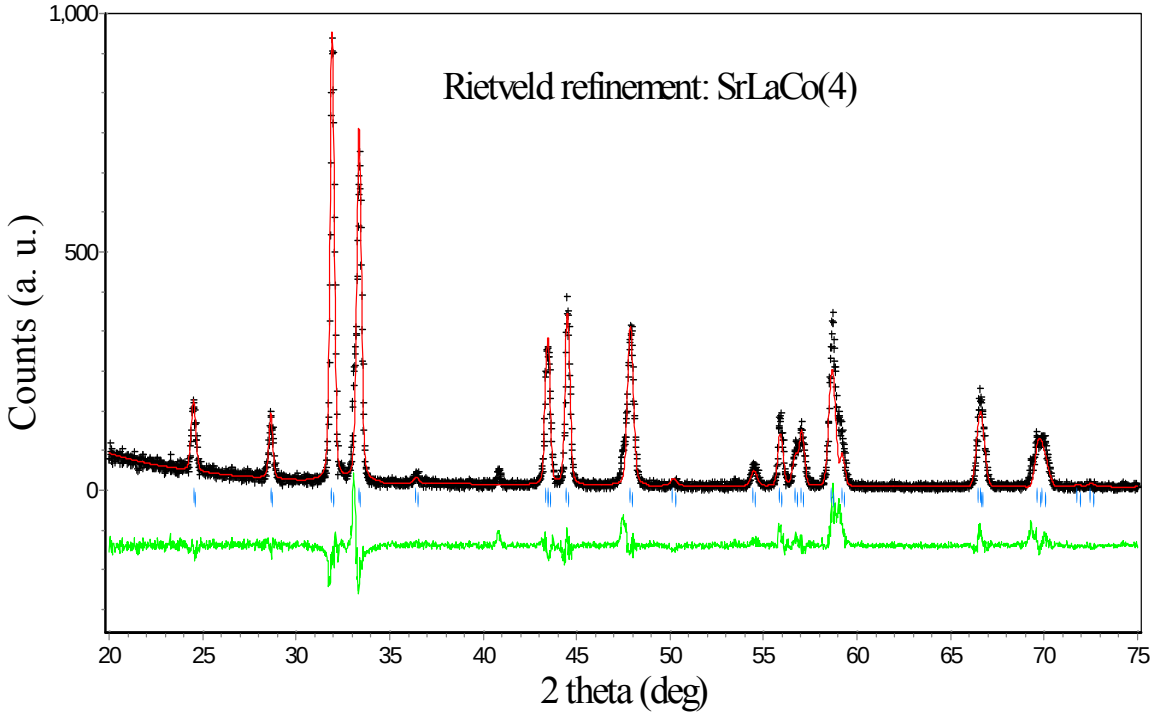

Fig. 4. 3 Rietveld refinement for $SrLaCoO_4$. The observed (crosses), calculated (solid line), and difference (bottom line) profiles at 300K for the x = 1 sample (refinement factors Rp=12.58%, Rb=7.3%).

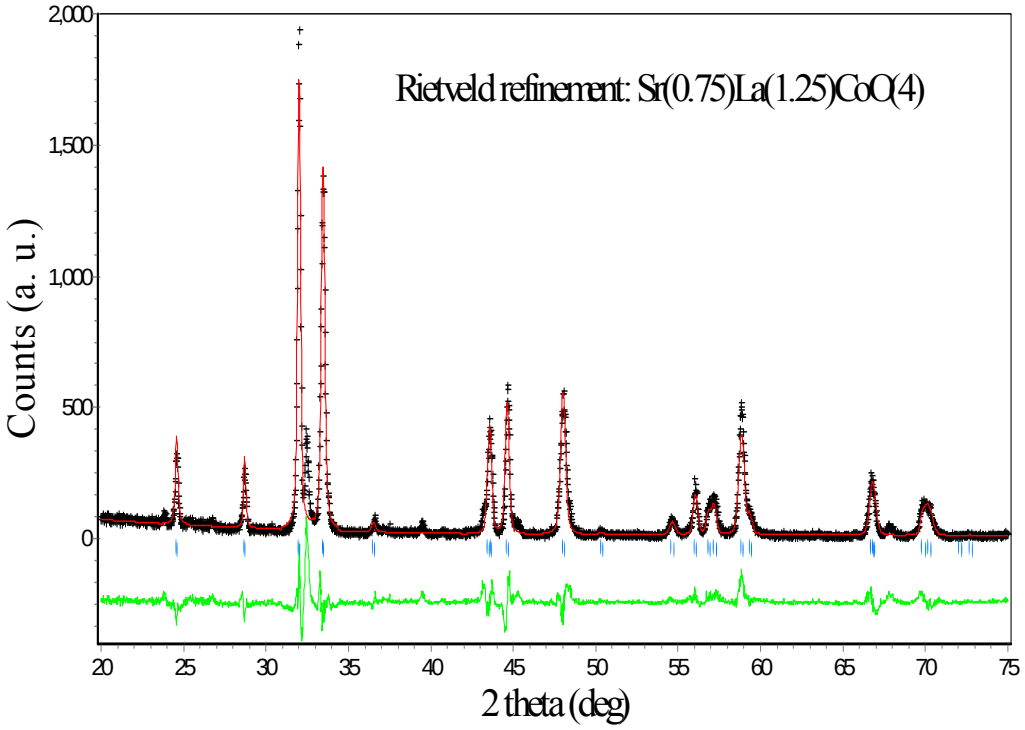

Fig. 4. 4 Rietveld refinement for $Sr_{0.75}La_{1.25}CoO_4$. The observed (crosses), calculated (solid line) and difference (bottom line) profiles at 300K (refinement factors Rp=12.58%, Rb=7.3% for the x = 1.25 sample).

The structural parameters shown in Table 4.1 were obtained from the Rietveld refinement of the XRD results on the $Sr_{2-x}La_xCoO_4$ samples with x = 0.75, 1, and 1.25. Lattice parameter *a* and the unit cell volume increase with increasing La content, while lattice parameter *c* increases as x increases from 0.75 to 1, then decreases slightly as x further increases to 1.25. Our refinement data is in accordance with the results on La doped Sr_2CoO_4 samples prepared using a solution method [39,113]. From Table 4.1, we can see that the atomic position for Sr/La is not sensitive to the La doping level. However, the O2 position varies with the individual doping levels. This is a reflection from the change in the Co-O(2) bond length, as will be discussed later on.

Structural parameters of $Sr_{2-x}La_xCoO_4$, with x = 0.75, 1, and 1.25, from the Rietveld refinement (space group I4/mmm) results are presented in Table 4.2, from which we can

see that the value for the out-of-plane Co-O(1) bond length is relatively stable against the La doping level x, retaining a value around 2.0 Å for all three samples. However, a steady increase in the in-plane Co-O(2) bond length is observed with increasing x. It is also obvious that the Co-O(1) bond length is greater than the corresponding Co-O(2) bond length for all three samples (Fig. 4.5). This indicates that La doping causes distortion of the CoO_6 octahedron with elongation along the *c*-axis (the Co-O(1) direction).

Table 4. 1 Crystal data on $Sr_{2-x}La_xCoO_4$ (x=0.75, 1, 1.25) - Space group: I4/mmm.

Atom	Sample	x	y	z	*B*iso[a]
Co	$Sr_{0.75}La_{1.25}CoO_4$	0	0	0	0.14
	$SrLaCoO_4$	0	0	0	0.14
	$Sr_{1.25}La_{0.75}CoO_4$	0	0	0	0.14
Sr/La	$Sr_{0.75}La_{1.25}CoO_4$	0	0	0.3605	0.11(La) 0.18(Sr)
	$SrLaCoO_4$	0	0	0.3605	0.14(Pr) 0.14(Sr)
	$Sr_{1.25}La_{0.75}CoO_4$	0	0	0.3605	0.09(Pr) 0.18(Sr)
O (1)	$Sr_{0.75}La_{1.25}CoO_4$	0	0.5	0	0.26
	$SrLaCoO_4$	0	0.5	0	0.29

	$Sr_{1.25}La_{0.75}CoO_4$	0	0.5	0	0.26
O (2)	$Sr_{0.75}La_{1.25}CoO_4$	0	0	0.1631	0.35
	$SrLaCoO_4$	0	0	0.1595	0.29
	$Sr_{1.25}La_{0.75}CoO_4$	0	0	0.1619	0.31

[a] *B*iso is an isotropic thermal parameter.

Table 4.2 Structural parameters of $Sr_{2-x}La_xCoO_4$ with x = 0.75, 1, and 1.25 from the Rietveld refinement (space group I4/mmm) results.

	x=0.75	*x=1*	*x=1.25*
a (Å)	*3.7936*	*3.8044*	*3.8169*
c (Å)	*12.4634*	*12.4904*	*12.4816*
Co-O(2) (Å)	*1.8968*	*1.9022*	*1.9084*
Co-O(1) (Å)	*2.0604*	*1.9925*	*2.0353*
V ($Å^3$)	*179.37*	*180.80*	*181.84*

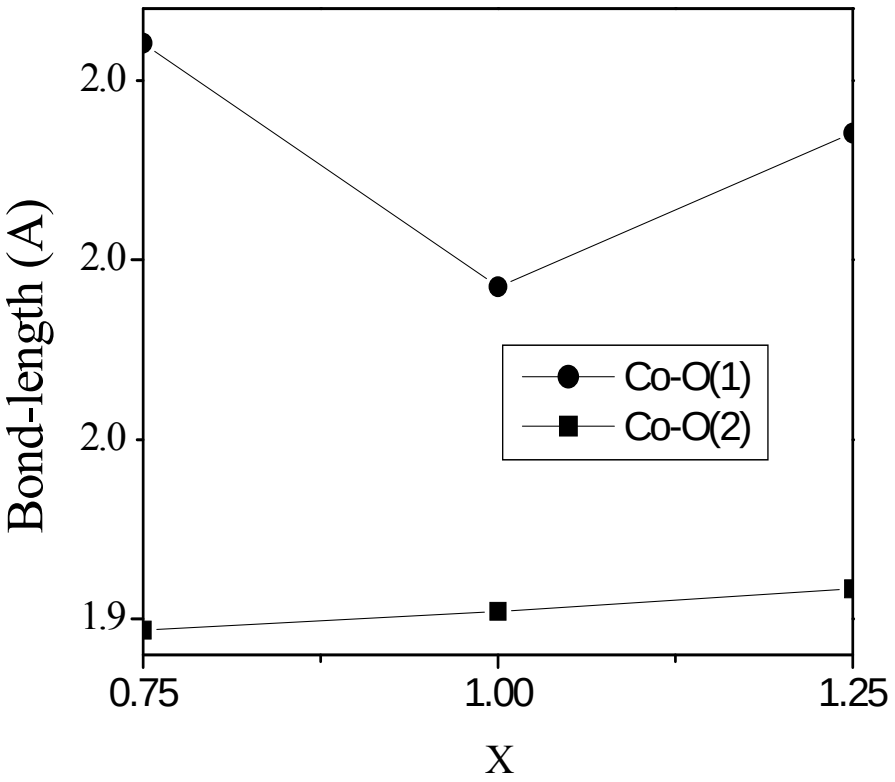

Fig. 4. 5 Co-O bond lengths vs. doping level x.

4.3 TRANSPORT PROPERTIES

The temperature dependence of the electrical resistivity in a temperature range of 5 K to 350 K for the $Sr_{2-x}La_xCoO_4$ samples with x = 0.75, 1, and 1.25 is shown in Fig. 4.6. The x = 1 sample exhibits semiconductor-like behavior over a wide range of temperatures below 350 K, in agreement with Ref. [113]. A metal-insulator transition was seen around 250 K when the x = 1.25 sample was heated up. However, the x = 0.75 sample reveals an increase in resistivity at T = 150 K. The resistivity of the samples increases with decreasing La doping level in the high temperature regime above 150 K. At room temperature, the resistivities for the x = 1 and 1.25 samples have approximately the

same value, which is about 10 Ohm-cm, while the resistivity of the x = 0.75 sample is about one order of magnitude larger than for the other two samples. In the lower temperature range (below 150 K), the rapid increase in resistivity with decreasing temperature for the x = 1 sample indicates more electron localization than in the x = 0.75 and 1.25 samples.

Resistivity (ρ) vs. $\exp(1/T)^{1/3}$ for the $Sr_{2-x}La_xCoO_4$ samples with x = 0.75, 1, and 1.25 is shown in Fig. 4.7. It was found that these three samples fit the VRH model in different temperature ranges, as shown by the straight line fittings. For the x = 0.75 compound, the VRH mechanism only occurs at temperatures below 95°C (where $(1/T)^{1/3} > 0.22$). For the sample with x = 1, the VRH model fits well over the whole measured temperature range. For the sample with x = 1.25, the VRH model fits well for temperatures below 200 K (where $(1/T)^{1/3} > 0.17$).

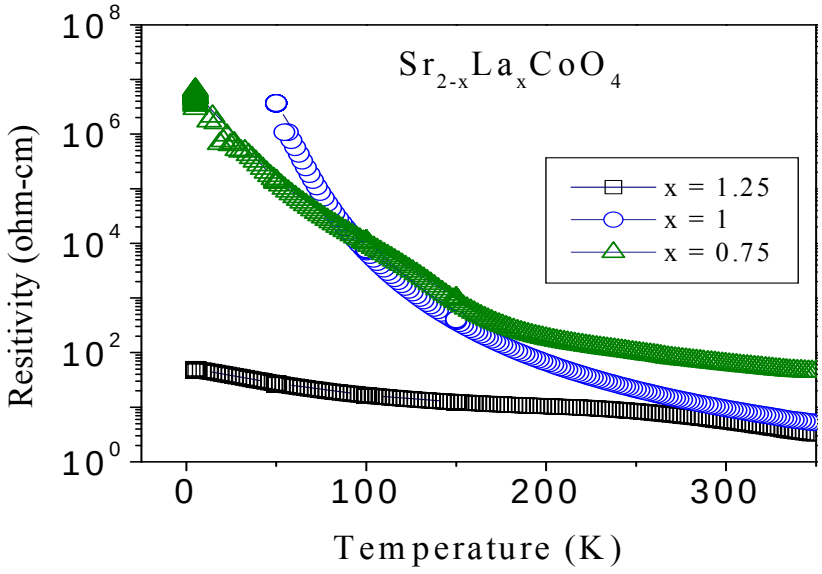

Fig. 4. 6 The temperature dependence of the electrical resistivity (ρ) of the $Sr_{2-x}La_xCoO_4$ samples with x = 0.75, 1, 1.25, from 5 K to 350 K, measured in zero field.

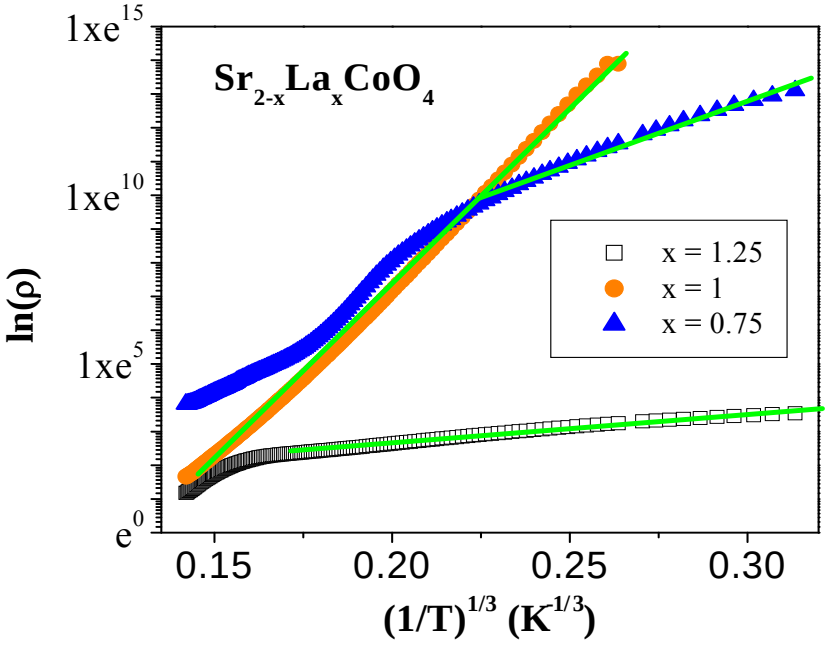

Fig. 4. 7 ln(ρ) vs. exp(1/T)$^{1/3}$ for $Sr_{2-x}La_xCoO_4$. Straight lines are linear fittings to the 2D VRH model.

4.4 MAGNETIZATION PROPERTIES

Fig. 4.8 shows the temperature dependence from 5 K to 350 K of the magnetization of the $Sr_{2-x}La_xCoO_4$ samples with x = 0.75, 1, and 1.25, measured in a magnetic field of 0.2 Tesla. Samples exhibited a paramagnetic to ferromagnetic transition at temperatures of about 250, 230, and 220 K for the x = 1.25, 1, and 0.75 samples, respectively. It is observed that La doping in $Sr_{2-x}La_xCoO_4$ drives the Curie temperature to higher values. The kink at about 160 K for the x = 0.75 sample is in accordance with the upturn in the temperature dependence of the resistivity observed at 160 K.

Fig. 4.9 shows the temperature dependence of the inverse susceptibility (χ^{-1}) for $Sr_{2-x}La_xCoO_4$, measured at a magnetic field of 2000 Oe. From this figure, the Curie temperature was determined to be 190 K, 230 K, and 250 K for the x = 0.75, 1, and 1.25 samples, respectively. The Weiss temperatures obtained by fitting to the Curie Weiss linear law were found to be 175 K, 220 K, and 240 K for the samples with x = 0.75, 1, and 1.25, respectively.

The magnetic hysteresis (MH) loops measured at 10 K for the $Sr_{2-x}La_xCoO_4$ samples with x = 0.75, 1, and 1.25 are shown in Fig. 4.10. The x = 0.75 sample shows a large coercive field of 1 Tesla. This implies a large crystal anisotropy energy. As for the other two samples, their coercive fields are much smaller (0.05 Tesla for the x = 1 and 0.1 Tesla for the x = 1.25 samples). The magnetization values at 5 Tesla and 10 K for the $Sr_{2-x}La_xCoO_4$ samples with x = 0.75, 1, and 1.25 were about 8, 7, and 7 emu/gram, respectively.

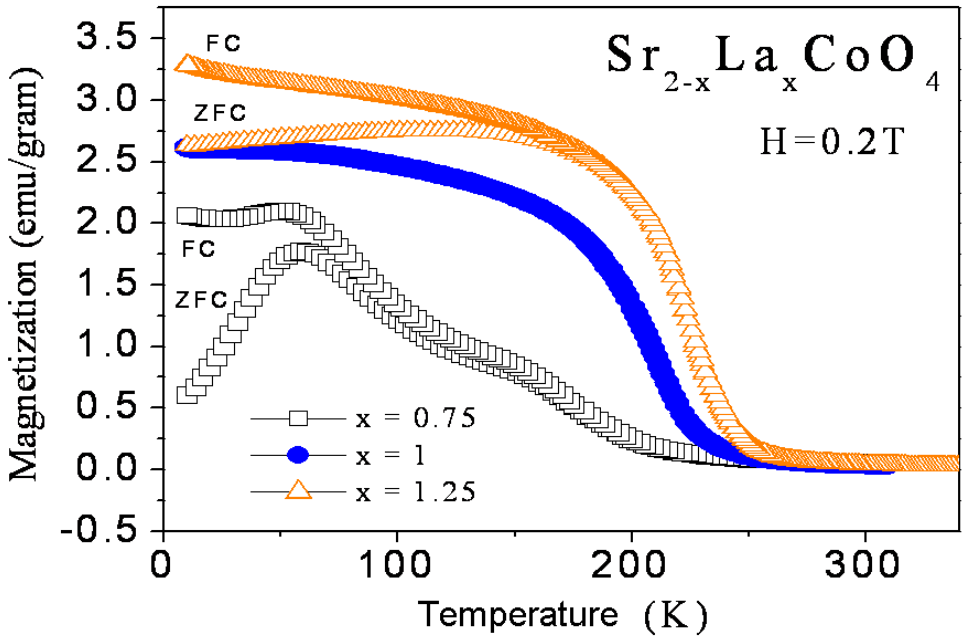

Fig. 4. 8 The temperature dependence from 5 K to 350 K of the magnetization of the $Sr_{2-x}La_xCoO_4$ samples with x = 0.75, 1, 1.25, measured in a magnetic field of 0.2 Tesla.

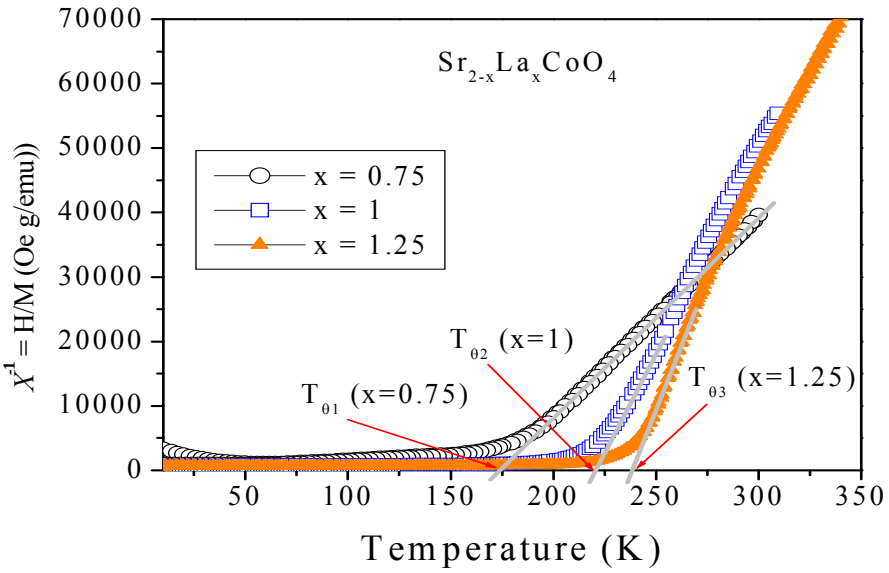

Fig. 4. 9 Temperature dependence of the inverse susceptibility (χ^{-1}) for the $Sr_{2-x}La_xCoO_4$ samples, measured at a magnetic field of 2000 Oe.

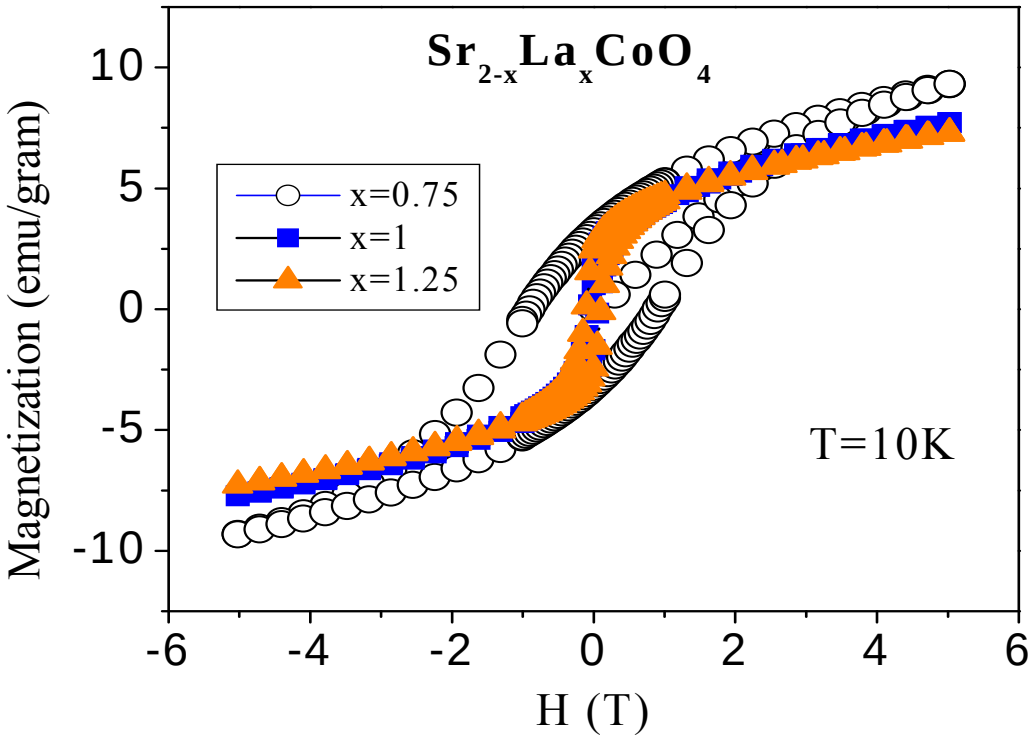

Fig. 4. 10 Magnetization hysteresis loops for the $Sr_{2-x}La_xCoO_4$ samples with x = 0.75, 1, and 1.25, measured at 10 K.

4.5 MAGNETORESISTANCE

The magnetoresistance (MR) effect is observed for all three samples. The MR values (defined as (ρ(*H*)- ρ(*H*=0)) /ρ(*H*=0)) at 6 Tesla are 1%, 2%, and 3% at 150 K for the x = 1, 0.75, and 1.25 samples, respectively, as shown in Fig. 4.11. The MR is enhanced to 7% at 5 K and at 6 Tesla for the x = 1.25 sample (Figs. 4.12 and 4.13). The MR values at 10 K were not measurable for the samples with x = 0.75 and 1, as their resistance rapidly increases beyond the measurement range of the equipment. Magnetoresistance hysteresis behavior is also observed for the x = 0.75 sample, which is in accordance with the observed magnetic hysteresis loop for this sample, as mentioned above.

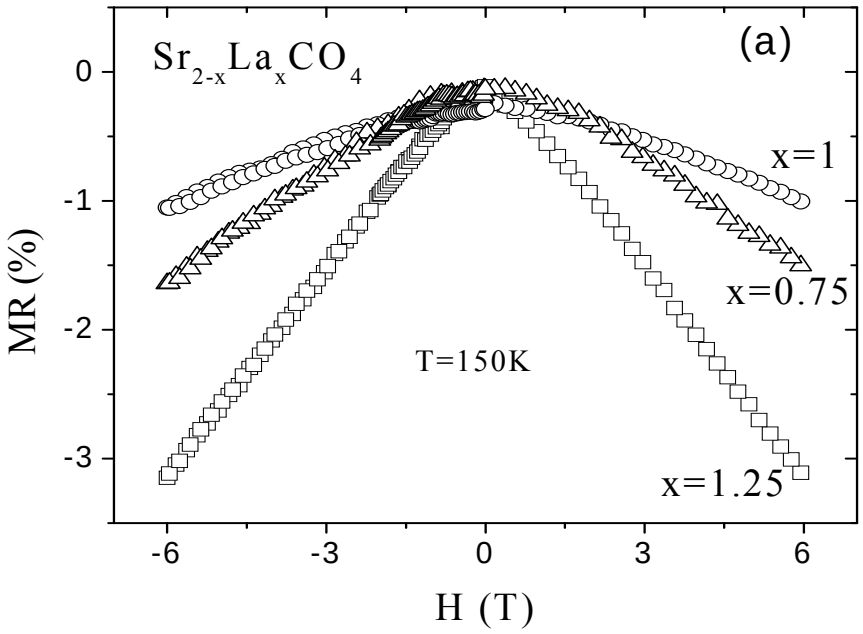

Fig. 4. 11 Field hysteretic magnetoresistance for $Sr_{1.25}La_{0.75}CoO_4$ at 150 K.

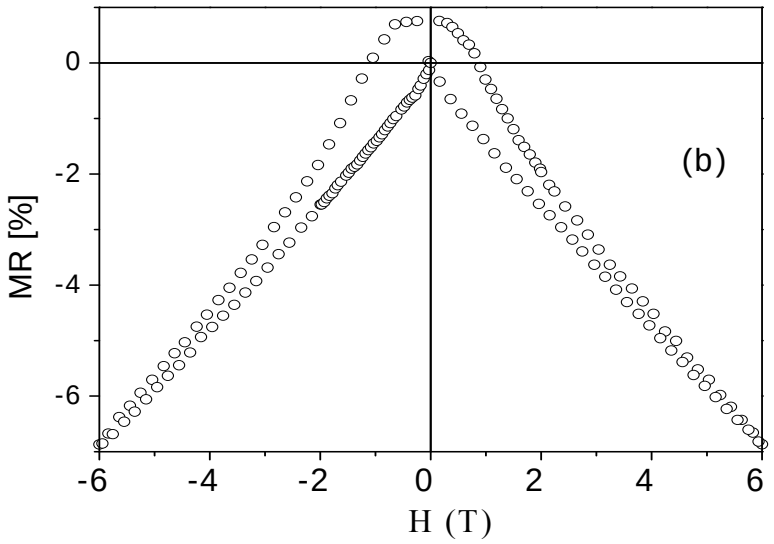

Fig. 4. 12 Magnetoresistance hysteresis for $Sr_{0.75}La_{1.25}CoO_4$ at 5 K.

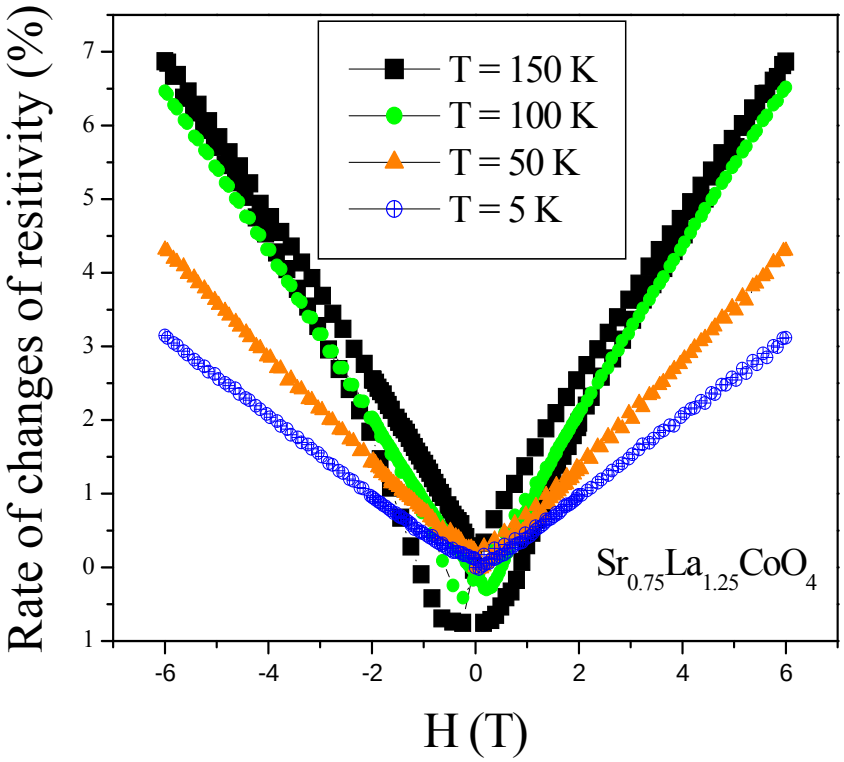

Fig. 4. 13 Rate of change of the resistivity for the sample with x = 1.25 at various temperatures in magnetic field.

4.6 BAND STRUCTURE

We performed band structure calculations for the $Sr_{1.5}La_{0.5}CoO_4$ compound, as shown in Fig 4.14. The object was to determine the total density of states (DOS) and the partial density of states (PDOS) for the Co atom and the in-plane and apical oxygen atoms. It can be seen that the compound shows a metallic nature, which is in accordance with the calculated result for pure Sr_2CoO_4 [1]. A significant density of states for the spin-down electrons is formed at the Fermi surface (E_F), indicating that this compound is spin polarized at the Fermi surface. The PDOS reveals that Co 3d electrons and planar

oxygen electrons are responsible for the high spin polarization at the Fermi surface in this compound.

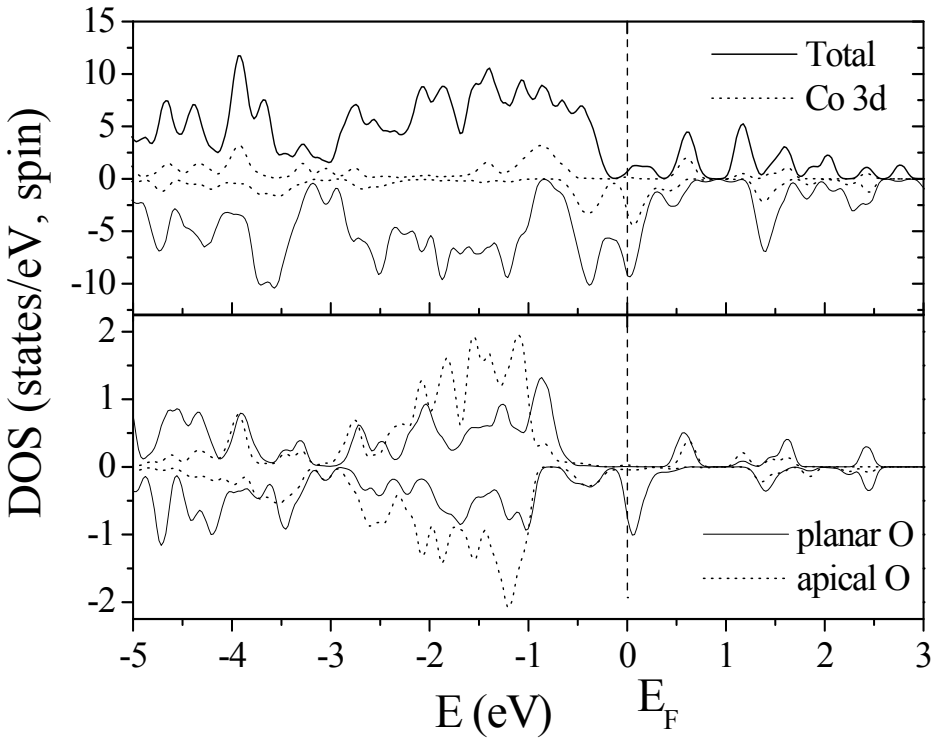

Fig. 4. 14 Calculated total density of states of $Sr_{1.5}La_{0.5}CoO_4$ compound and the partial density of states of Co 3d (upper panel); and the partial density of states of planar and apical oxygen (lower panel), with the Fermi energy set at zero.

4.7 SUMMARY

La doped Sr_2CoO_4 compounds are crystallized in the K_2NiF_4-type structures with space group *I*4/*mmm*. The temperature dependence of the resistivity shows semiconductor-like behavior over a wide range of temperatures, a metal-insulator transition at 240 K, and an upturn at 160 K for the x = 1, 1.25, and 0.75 samples. The coercive field is about 1 T for the sample with x = 0.75, while it is about 0.05 T for the x = 0.75 and 0.1 T for the x

= 1.25 samples. A negative field hysteresis in the magnetoresistance in close correlation with the coercive field has been observed and can be explained by the grain boundary tunneling effect. First-principles band structure calculations were carried out for $Sr_{1.5}La_{0.5}CoO_4$, and the results indicate that the system is metallic with a high spin polarization, which is responsible for the observed large magnetoresistance. The band structure calculations for $Sr_{1.5}La_{0.5}CoO_4$ compound indicate that this compound is spin polarized at the Fermi surface. The PDOS reveals that the Co 3d electrons and planar oxygen electrons are responsible for the high spin polarization at the Fermi surface in this compound.

CHAPTER 5. EU DOPED Sr_2CoO_4 ($Sr_{2-x}Eu_xCoO_4$, x = 0.25, 0.75, 1, 1.25)

5.1 INTRODUCTION

Polycrystalline samples of $Sr_{2-x}Eu_xCoO_4$ (x = 0.25, 0.75, 1, 1.25) were synthesized by a conventional solid-state reaction method as mentioned in section II. Powders of Eu_2O_3, $SrCO_3$, and Co_3O_4 with high purity were used as starting materials. The phases and structures of the resulting samples at room temperature were studied using x-ray powder diffraction (XRD). Structure refinements were carried out by the Rietveld method using the RIETICA program. Magnetic and electrical transport properties were investigated using commercial Quantum Design Magnetic and Physical Properties Measurement Systems (MPMS and PPMS) in a temperature range from 5 to 350 K, and in magnetic fields up to 8 Tesla.

5.2 STRUCTURAL PROPERTIES

The XRD patterns of the samples of $Sr_{2-x}Eu_xCoO_4$ (where x = 0.25, 0.75, 1, 1.25) for the 2 θ range from 25 to 65 degrees, measured at room temperature, are shown in Fig. 5.1. It can be seen that the diffraction peaks of the samples with x = 0.75 and 1 fit well with the XRD pattern of the Sr_2CoO_4 phase, indicating that pure phase was obtained for these two doping levels. All the diffraction peaks were indexed and labeled for the sample with x = 1. However, the other two samples with x = 0.25 and 1.25 contain diffraction peaks of unknown impurities with the sample with x = 0.25 containing more impurities than the sample with x = 1.25. These results shows that both a low doping level (x =

0.25) and a high doping level (x = 1.25) of Eu will introduce impurities into the samples. Pure K_2NiF_4 phase of Sr_2CoO_4 can be obtained when x is from 0.75 to 1, indicating that Sr_2CoO_4 is quite sensitive to the Eu doping level.

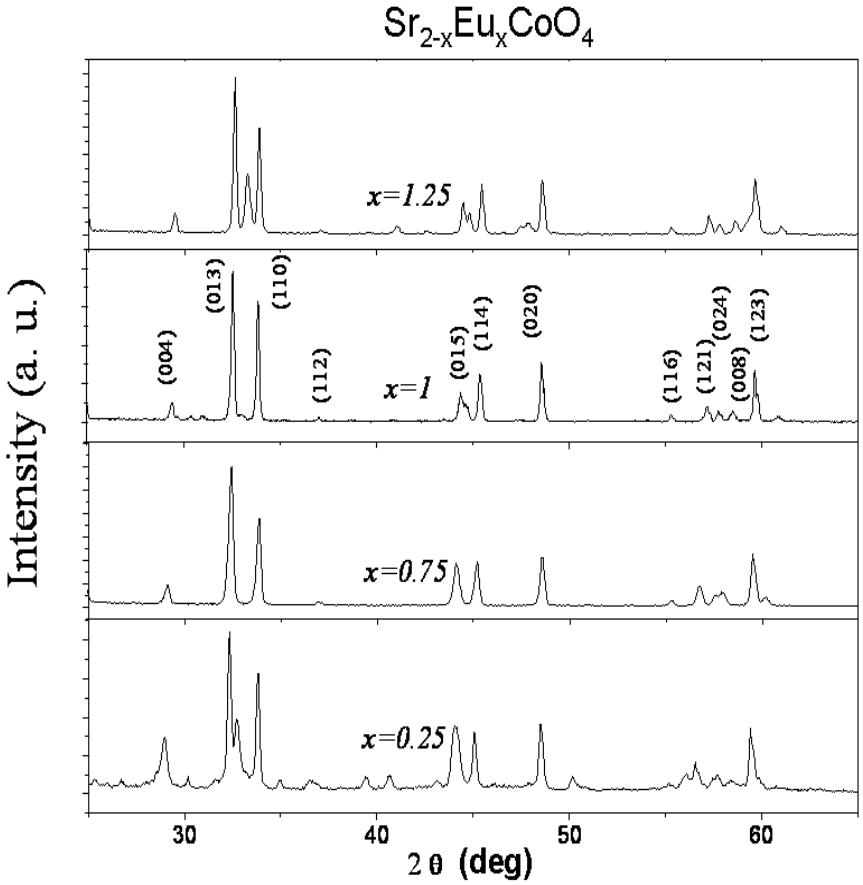

Fig. 5. 1 XRD patterns of the $Sr_{2-x}Eu_xCoO_4$ samples with x = 0.25, 0.75, 1, 1.25, measured at room temperature.

Rietveld refinement was carried out based on the XRD results for the $Sr_{2-x}Eu_xCoO_4$ samples with x = 0.75, 1, and 1.25, which are shown in Figs. 5.2, 5.3, and 5.4, respectively. The observed (crosses), calculated (solid lines), and difference diffraction (bottom lines) profiles were plotted in each figure. It can be seen that the calculated results match well with the experimental data for all the three samples. Our refinement shows that the samples of $Sr_{2-x}Eu_xCoO_4$ with x = 0.75, 1, 1.25 have the K_2NiF_4 structure.

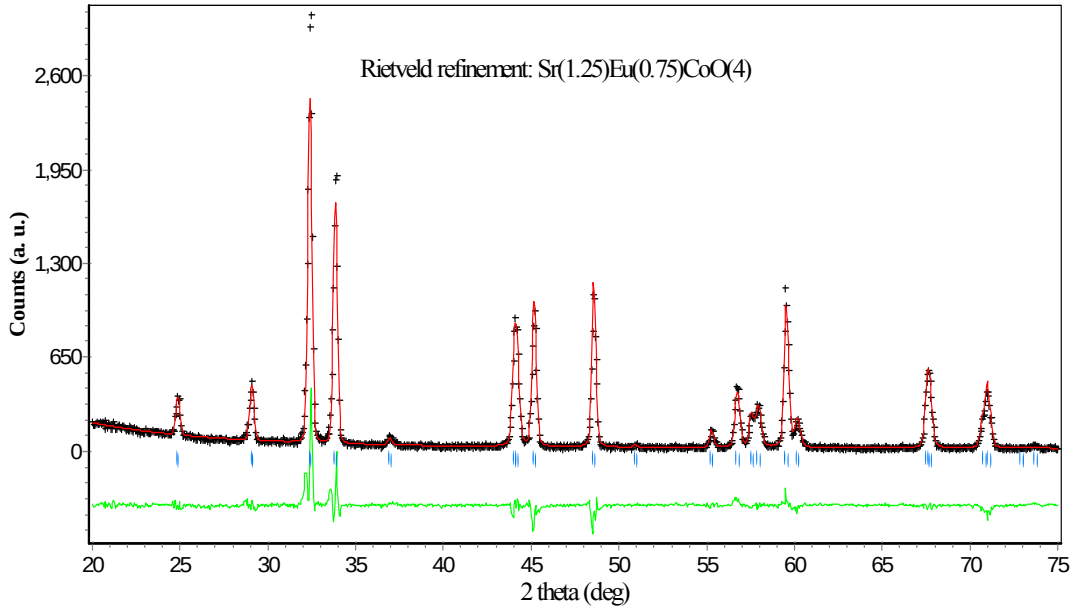

Fig. 5. 2 Rietveld refinement for $Sr_{1.25}Eu_{0.75}CoO_4$ showing the observed (crosses), calculated (solid line) and difference (bottom line) profiles at 300K (refinement factors Rp=11.4%, Rb=2.9%).

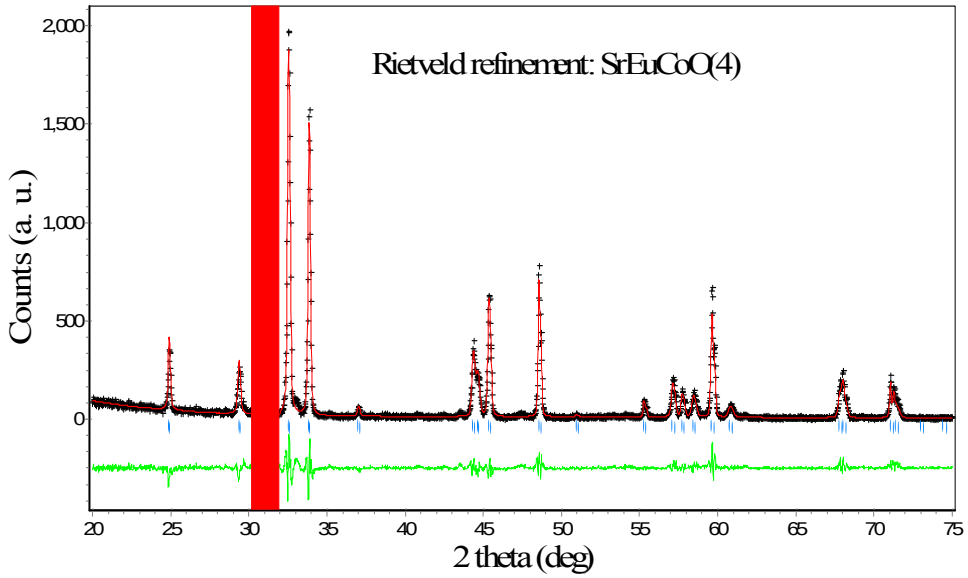

Fig. 5. 3 Rietveld refinement for $SrEuCoO_4$ showing the observed (crosses), calculated (solid line) and difference (bottom line) profiles at 300K (refinement factors Rp=13.4%, Rb=2.1%;, blue-strip range was ignored in refinement).

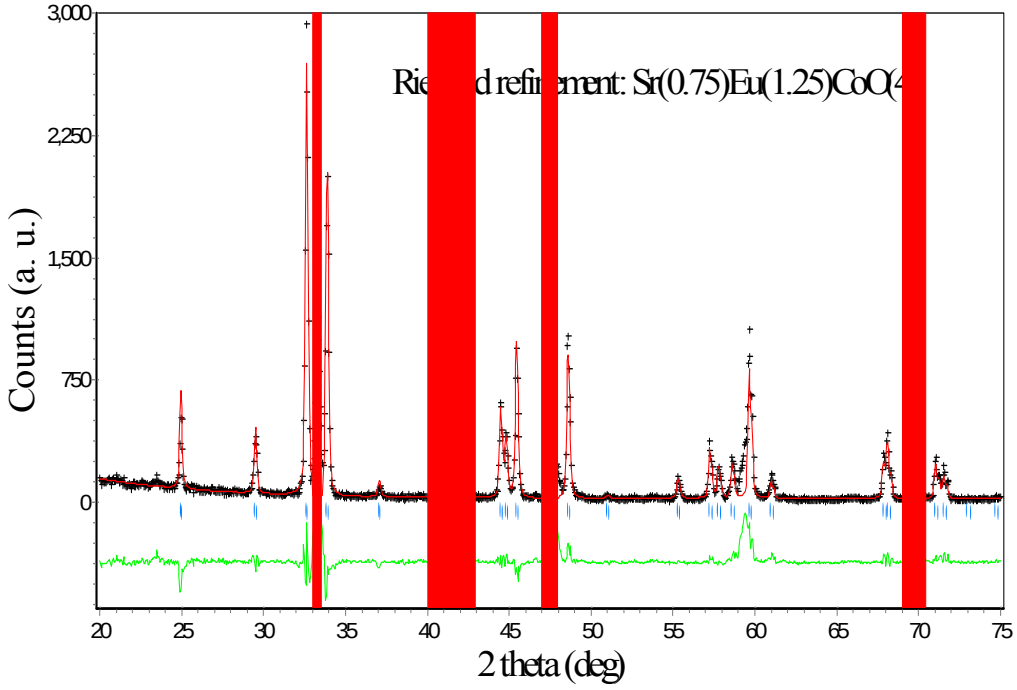

Fig. 5. 4 Rietveld refinement for $Sr_{0.75}Eu_{1.25}CoO_4$ showing the observed (crosses), calculated (solid line) and difference (bottom line) profiles at 300K (refinement factors Rp=13.8%, Rb=4.6%; blue-strip ranges were ignored in refinement).

The atomic parameters, isotropic temperature factors, Co-O bond lengths and unit cell volumes obtained from the refinement results are summarized in Tables 5.1 and 5.2. From Table 5.1, we can see that the atomic position for Sr/Eu is not sensitive to the Eu doping level. However, the O2 position changes slightly for the sample with x = 1. From Table 5.2, it is observed that lattice parameter *a* is not sensitive to the doping level of Eu. Table 5.2 also reveals a close correlation with respect to the doping level of Eu between lattice parameter *c* and the Co-O(1) bond length: they are at a maximum for x = 0.75, but as x increases to 1, there is an obvious decrease in both lattice parameter *c* and the Co-O(1) bond length. As x further increases to 1.25, both values show no significant changes.

The values for the in-plane Co-O(2) bond length remain at around 1.87 Å for all the

doping levels. However, for all the samples, the out-of-plane Co-O(1) bond length values are greater than 1.96 Å, and they decrease with x (Fig. 5.5). These results indicate that the Eu doping causes distortion of the CoO_6 octahedron with elongation along the *c*-axis (the Co-O(1) direction).

Table 5.1 Crystal data of $Sr_{2-x}Eu_xCoO_4$ (x = 0.75, 1, 1.25) - Space group: I4/mmm.

Atom	Samples	x	y	z	*B*iso[a]
Co	$Sr_{0.75}Eu_{1.25}CoO_4$	0	0	0	0.14
	$SrEuCoO_4$	0	0	0	0.14
	$Sr_{1.25}Eu_{0.75}CoO_4$	0	0	0	0.14
Sr/Eu	$Sr_{0.75}Eu_{1.25}CoO_4$	0	0	0.3605	-0.33(Eu) 0.72(Sr)
	$SrEuCoO_4$	0	0	0.3605	0.14(Eu) 0.14(Sr)
	$Sr_{1.25}Eu_{0.75}CoO_4$	0	0	0.3605	0.09(Eu) 0.18(Sr)
O (1)	$Sr_{0.75}Eu_{1.25}CoO_4$	0	0.5	0	0.26
	$SrEuCoO_4$	0	0.5	0	0.30
	$Sr_{1.25}Eu_{0.75}CoO_4$	0	0.5	0	0.29
O (2)	$Sr_{0.75}Eu_{1.25}CoO_4$	0	0	0.1618	0.24

	$SrEuCoO_4$	0	0	0.1664	0.32
	$Sr_{1.25}Eu_{0.75}CoO_4$	0	0	0.1618	0.29

[a] *B*iso is an isotropic thermal parameter.

Table 5.2 Structural parameters of $Sr_{2-x}Eu_xCoO_4$ with x = 0.75, 1 & 1.25 from the Rietveld refinement (space group I4/mmm) results.

	x=0.75	*x=1*	*x=1.25*
a (Å)	*3.76*	*3.77*	*3.76*
c (Å)	*12.32*	*12.17*	*12.17*
Co-O(2) (Å)	*1.8776*	*1.8766*	*1.8784*
Co-O(1) (Å)	*1.9929*	*1.9732*	*1.9691*
V ($Å^3$)	*173.7*	*171.8*	*171.8*

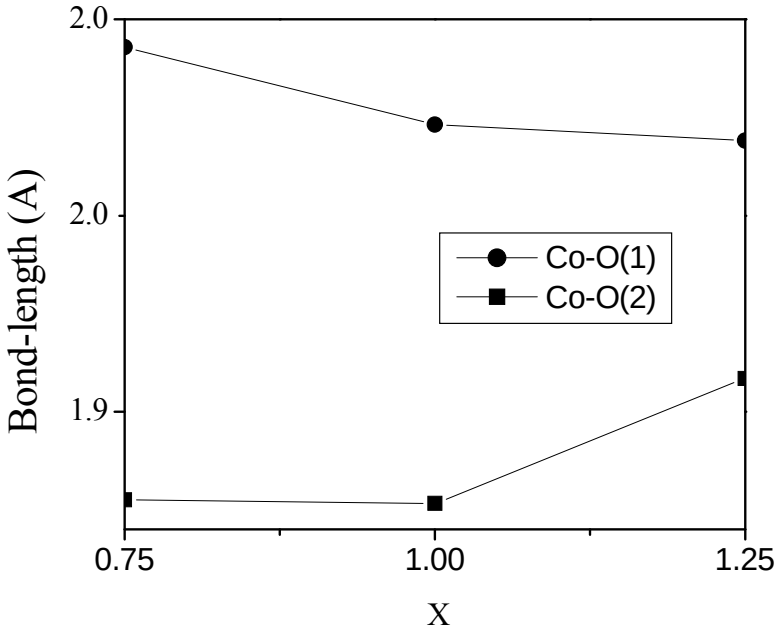

Fig. 5. 5 Co-O bond lengths vs. doping level x.

5.3 TRANSPORT PROPERTIES

The temperature dependence of the electrical resistivity in the temperature range of 5 K to 350 K for the $Sr_{2-x}Eu_xCoO_4$ samples with x = 0.75, 1, 1.25 is shown in Fig. 5.6. It can be seen that all the samples show semiconductor-like behaviour. However, the values of the resistivity are quite different for the three samples with different doping levels. The samples with x = 0.75 and 1.25 have very low resistivities that are less than 20 Ohms·cm in the high temperature range above 150 K. However, the sample with x = 1 is much more insulating than the other two samples (with a resistivity value of about 10^5 Ohm·cm at 150 K). Therefore, regularity in the samples' resistivity corresponding to the

Eu doping level is not observed in this case.

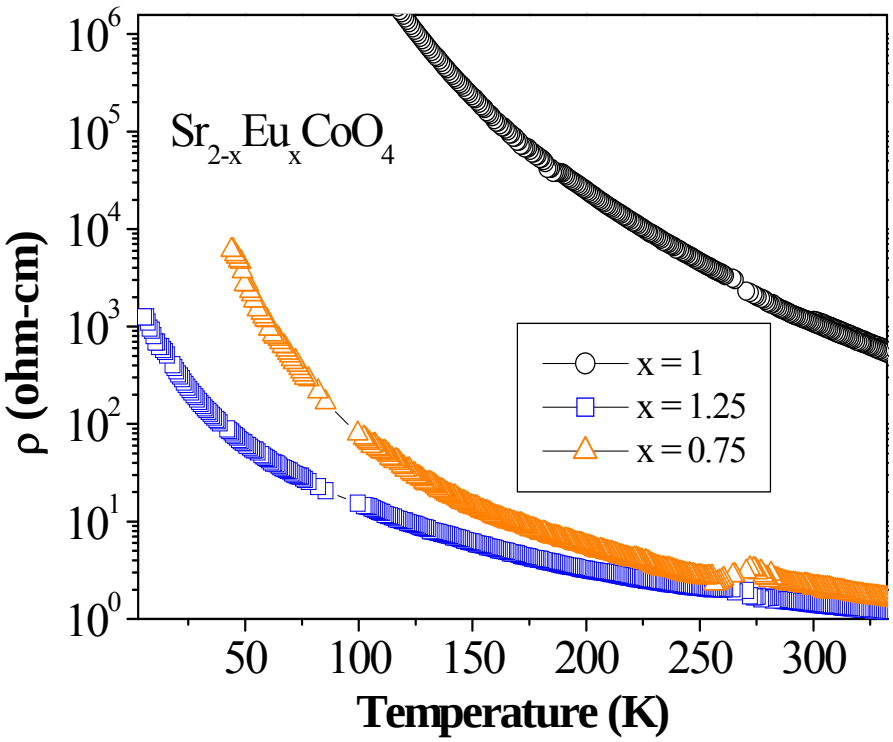

Fig. 5. 6 Temperature dependence of the resistivity of $Sr_{2-x}Eu_xCoO_4$ with x = 0.75, 1, 1.25.

Log of the resistivity (ρ) vs. $\exp(1/T)^{1/3}$ for the $Sr_{2-x}Eu_xCoO_4$ samples with x = 0.75, 1, and 1.25 is shown in Fig. 5.7. These three compounds are observed to behave differently in the VRH 2D model fitting. For x = 1, the compound is well fitted by the VRH model for the entire measurable range of its resistivity over a temperature range from 100 K to 300 K (where $0.15 < (1/T)^{1/3} < 0.21$). For x = 0.75, the compound does not really follow the VRH mechanism. For the x = 1.25 compound, the VRH mechanism is only observed in the small low temperature range of 7 K to 15 K (where $0.4 < (1/T)^{1/3} < 0.55$).

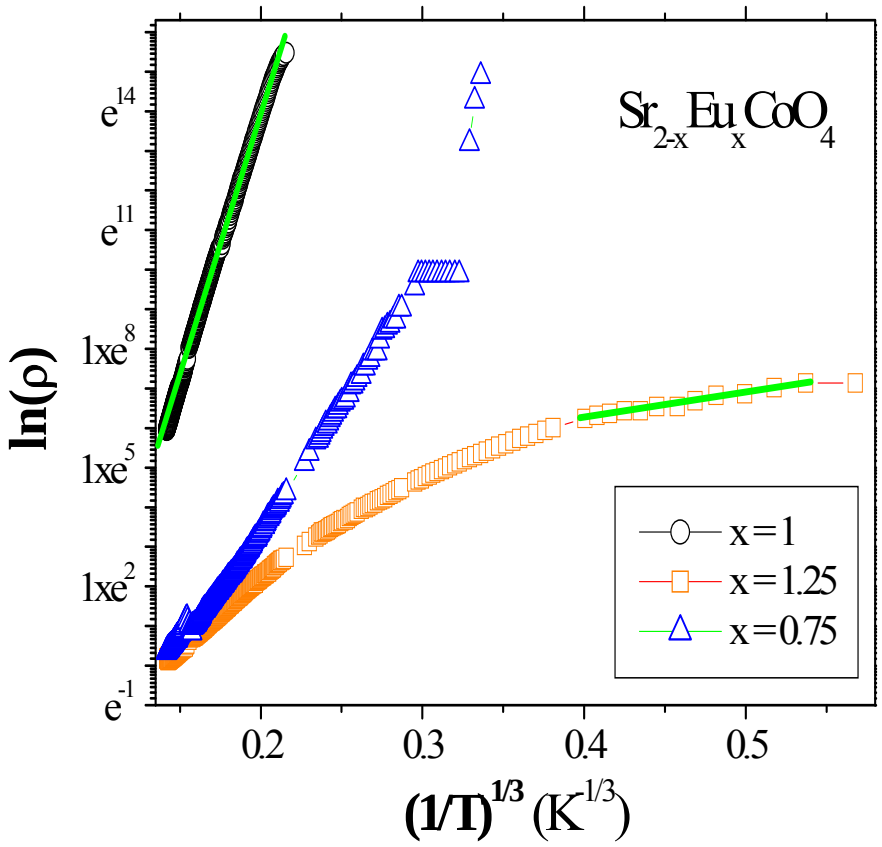

Fig. 5. 7 ln(ρ) vs. exp(1/T)$^{1/3}$ for $Sr_{2-x}Eu_xCoO_4$ with x = 0.75, 1, 1.25. Straight lines are linear fittings to the 2D VRH model.

5.4 MAGNETIZATION PROPERTIES

Fig. 5.8 shows the temperature dependence from 5 K to 350 K of the magnetization of the $Sr_{2-x}Eu_xCoO_4$ samples with x = 0.75 and 1, measured in a magnetic field of 0.2 Tesla. The sample with x = 0.75 exhibits a paramagnetic to ferromagnetic transition at around 200 K. However, the sample with x = 1 shows paramagnetic behavior down to 5 K, although a weak, but wide hump was observed in the temperature range from 100 K to

180 K, which may relate to an antiferromagnetic transition, as both ZFC and FC results show the same decrease.

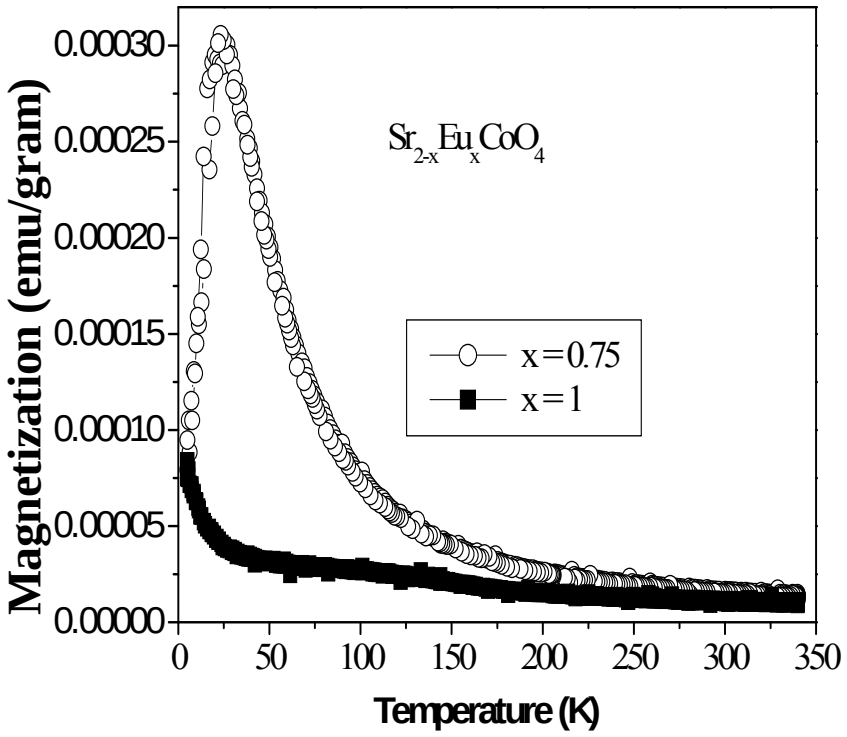

Fig. 5. 8 Field cooled and zero field cooled temperature dependence of magnetization for $Sr_{2-x}Eu_xCoO_4$ with x = 0.75 and 1.

5.5 MAGNETORESISTANCE

Figs. 5.9, 5.10 and 5.11 respectively show the field dependence of the magnetoresistance (MR) effect (defined as (ρ(*H)* - ρ(*H*=0)) /ρ(*H*=0)), measured at a temperature of 100 K for the samples with x = 0.75, 1, and 1.25. It is observed that these samples have large MR values. For example, for the sample with x = 1.25, the MR value is about 46% at 8 Tesla at 100 K.

The unusual large magnetoresistance value for these samples is encouraging with regards to the potential application of colossal MR (CMR) materials.

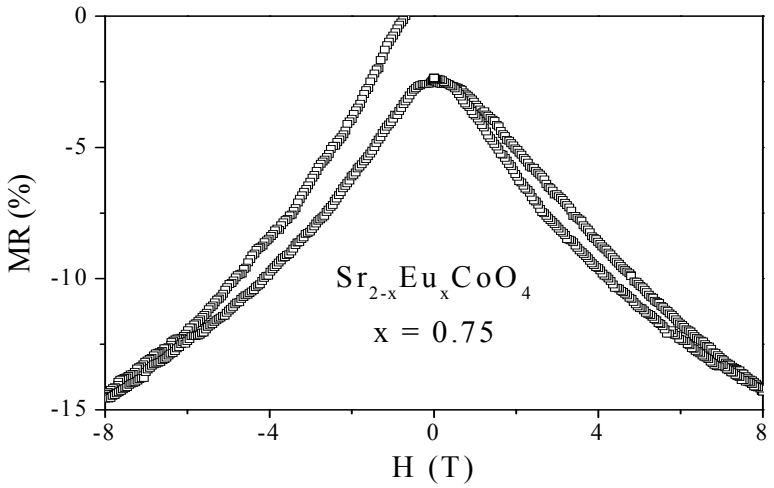

Fig. 5. 9 Magnetoresistance hysteresis for the $Sr_{1.25}Eu_{0.75}CoO_4$ sample at 100 K.

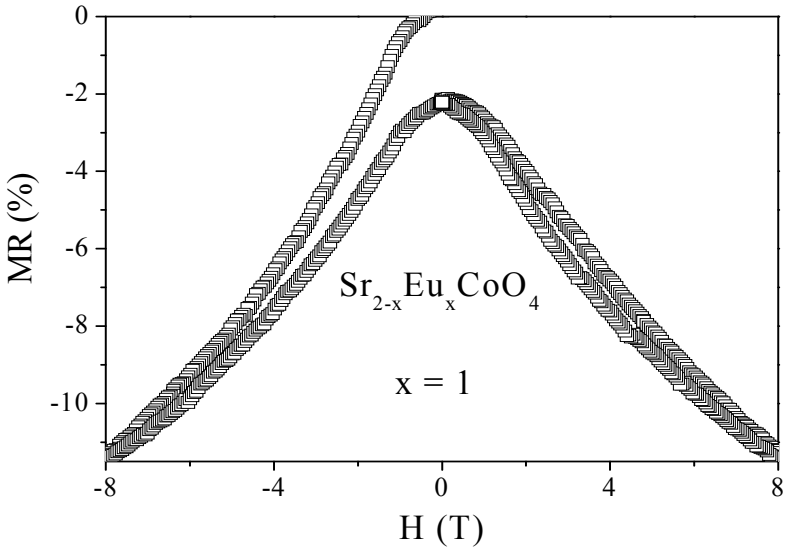

Fig. 5. 10 Magnetoresistance hysteresis for the $SrEuCoO_4$ sample at 100 K.

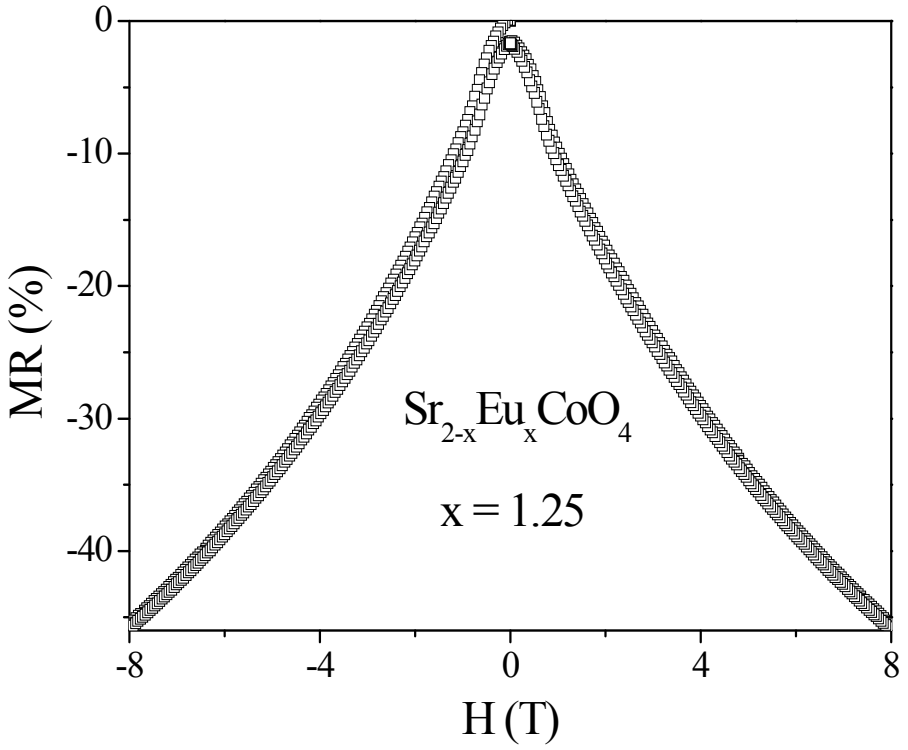

Fig. 5. 11 Magnetoresistance hysteresis for the $Sr_{0.75}Eu_{1.25}CoO_4$ sample at 100 K.

5.6 SUMMARY

For the Eu doped compounds of Sr_2CoO_4, single 214 phase was achieved for x = 0.75 - 1. Lattice parameter *c* decreases with Eu doping levels. The Curie temperatures were found to be around 160-200 K for samples with x = 0.75 and 1. An antiferromagnetic transition is observed at 35 K for the x = 0.75 sample. Magnetic semiconductor features are observed for all the doped samples. The existence of the unusual high magnetoresistance in these compounds make them stands out compared to the rest of the other RE doped compounds in this regard. For example, the sample with x = 1.25 shows a MR value of about 46% at 8 Tesla at 100 K. Finding such unusual large

magnetoresistance values for these samples is encouraging, as regards to the potential applications of CMR materials.

CHAPTER 6. GD DOPED Sr_2CoO_4 ($Sr_{2-x}Gd_xCoO_4$, x = 0.5, 0.75, 1, 1.25)

6.1 INTRODUCTION

Polycrystalline samples of $Sr_{2-x}Gd_xCoO_4$ (x = 0.5, 0.75, 1, 1.25) were synthesized by a conventional solid-state reaction method as mentioned in section II. Powders of Gd_2O_3, $SrCO_3$, and Co_3O_4 with high purity were used as starting materials. The phases and structures of the resulting samples at room temperature were studied using x-ray powder diffraction (XRD). Structure refinements were carried out by the Rietveld method using the RIETICA program. Magnetic and electrical transport properties were investigated using commercial Quantum Design Magnetic and Physical Properties Measurement Systems (MPMS and PPMS) in a temperature range from 5 to 350 K, and in magnetic fields up to 8 Tesla.

6.2 STRUCTURAL PROPERTIES

The XRD patterns of the $Sr_{2-x}Gd_xCoO_4$ samples (where x = 0.5, 0.75, 1, 1.25) for the 2 θ range from 30 to 70 degrees, measured at room temperature, are shown in Fig. 6.1. It can be seen that the diffraction peaks of all the four samples fit well with the XRD profile of Sr_2CoO_4 single phase, However, there is an unknown impurity shown in the

range of 32.5 to 33 degrees in the XRD patterns. For each of the samples, the unknown peak is marked with an asterisk.

Rietveld refinement was carried out based on the XRD results for all four samples of $Sr_{2-x}Gd_xCoO_4$. They are shown in Figs. 6.2, 6.3, 6.4, and 6.5, respectively. The observed (crosses), calculated (solid lines), and difference diffraction (bottom lines) profiles were plotted in each figure. It can be seen that the calculated results match well with the experimental data for all four samples. Our refinement shows that these samples have the K_2NiF_4 structure.

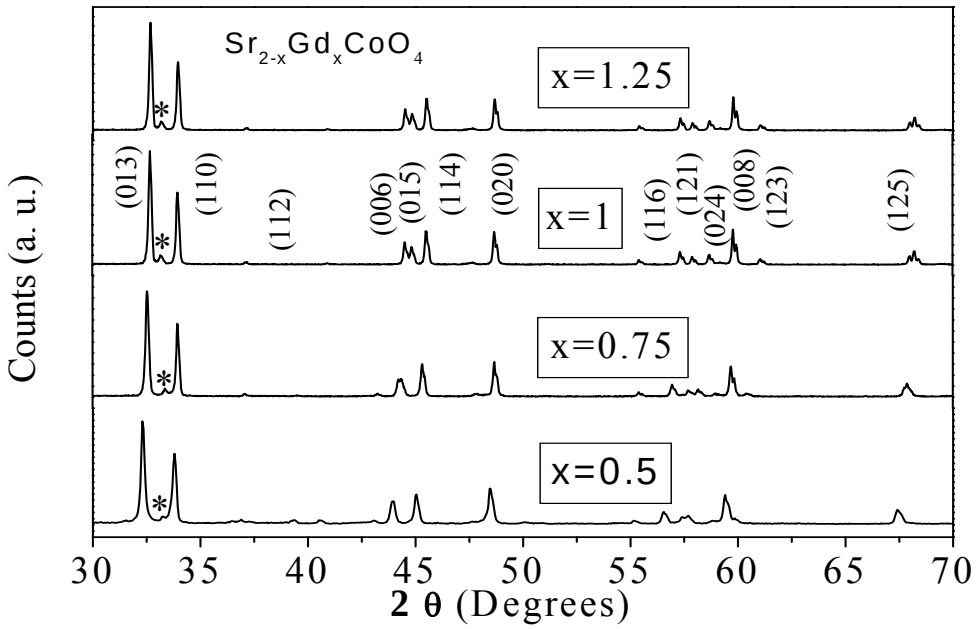

Fig. 6. 1 XRD patterns of $Sr_{2-x}Gd_xCoO_4$ with x = 0.5, 0.75, 1, 1.25 (indicates unknown impurity).*

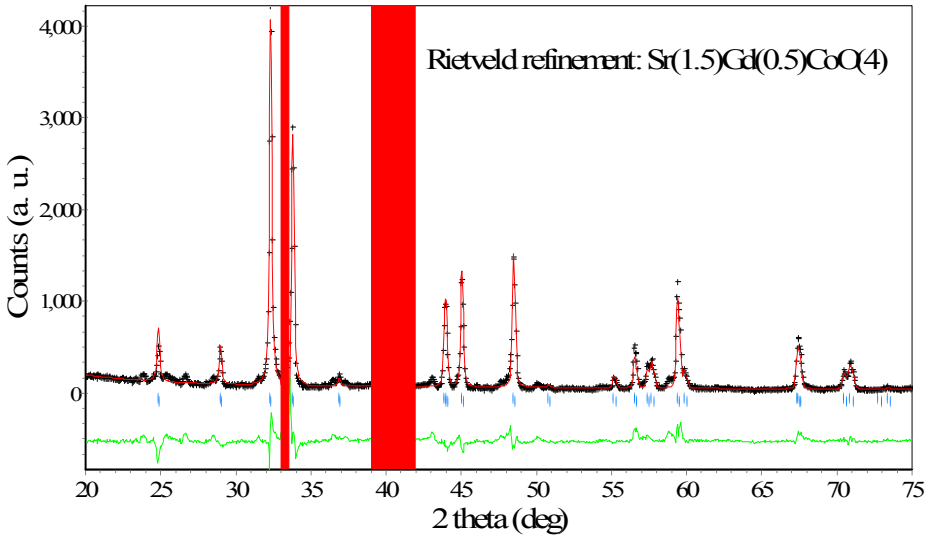

Fig. 6. 2 Rietveld refinement for $Sr_{1.5}Gd_{0.5}CoO_4$ showing the observed (crosses), calculated (solid line) and difference (bottom line) profiles at 300K (refinement factors Rp=14.5%, Rb=5.6%; blue-strip ranges were ignored in refinement).

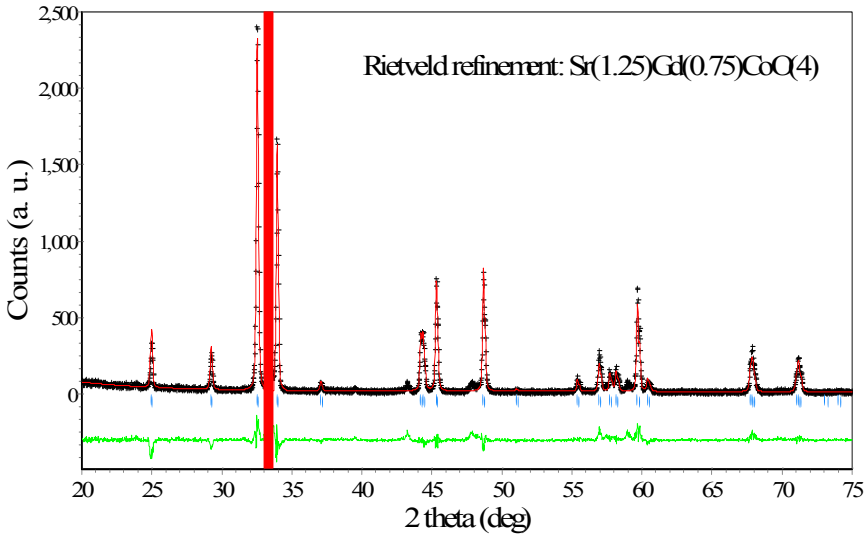

Fig. 6. 3 Rietveld refinement for $Sr_{1.25}Gd_{0.75}CoO_4$ showing the observed (crosses), calculated (solid line) and difference (bottom line) profiles at 300K (refinement factors Rp=14.3%, Rb=6.2%;, blue-strip range was ignored in refinement).

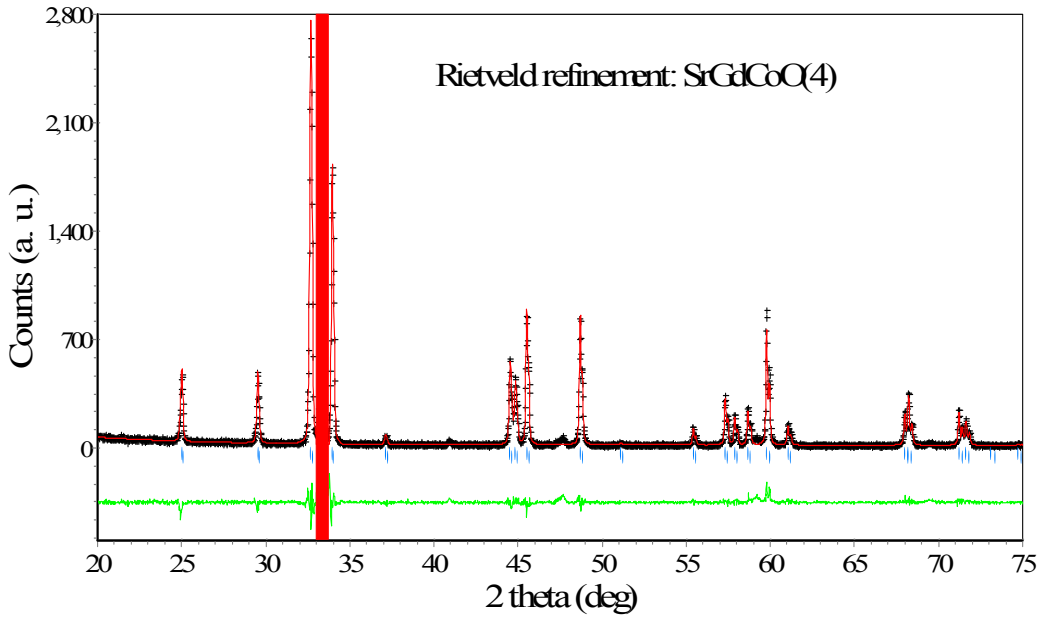

Fig. 6. 4 Rietveld refinement for $SrGdCoO_4$ showing the observed (crosses), calculated (solid line) and difference (bottom line) profiles at 300K (refinement factors Rp=12.0%, Rb=3.2%; blue-strip range was ignored in refinement).

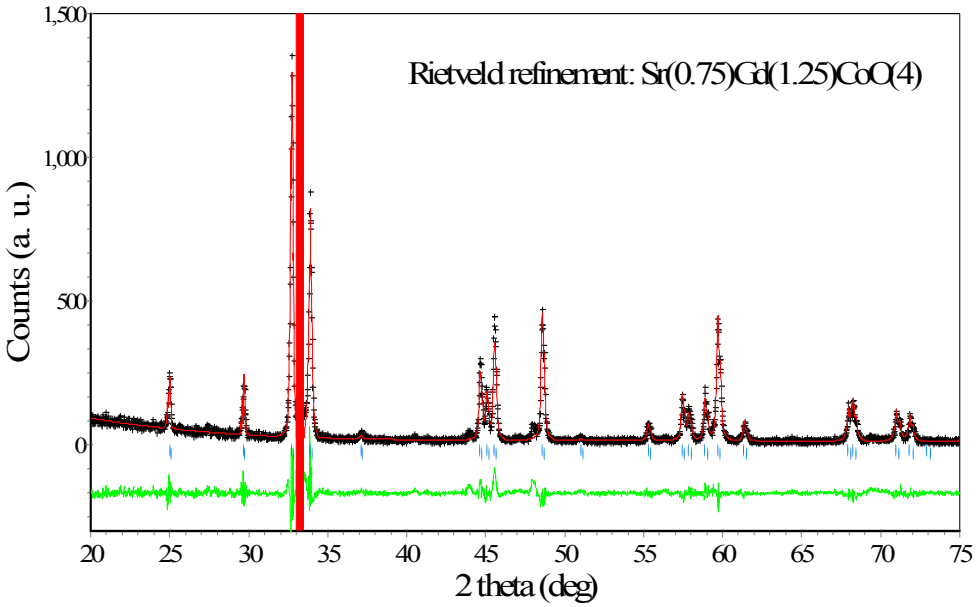

Fig. 6. 5 Rietveld refinement for $Sr_{0.75}Gd_{1.25}CoO_4$ showing the observed (crosses), calculated (solid line) and difference (bottom line) profiles at 300K (refinement factors Rp=16.6%, Rb=7.6%; blue-strip range was ignored in refinement).

The atomic parameters, isotropic temperature factors, Co-O bond lengths, and unit cell volumes obtained from the refinement results are summarized in Tables 6.1 and 6.2. From Table 6.1, we can see that the atomic position for Sr/Gd is not sensitive to the Gd doping level. However, the O2 position changes for each of the doping levels.

The refined results on lattice parameters *a* and *c* are plotted in Fig. 6.6. It can be seen clearly that lattice parameter *a* is not sensitive to the Gd doping level, and it changes very slightly for different doping level x, while lattice parameter *c* decreases as the doping level x increases. This is in agreement with the fact that the ion size of Gd^{3+} (radius 0.94 Å) is smaller than the ion size of Sr^{2+} (radius 1.32 Å).

The value for the in-plane Co-O(2) bond length has almost the same value, around 1.88 Å, for all the doping levels, while the out-of-plane Co-O(1) bond length values vary for different doping level x. It was also observed that for all the samples, the out-of-pane Co-O(1) bond length is at least 0.1 Å greater than the corresponding in-plane bound length. This indicates that the Gd doping causes a distortion of the CoO_6 octahedron with elongation along the *c*-axis (the Co-O(1) direction) (Fig. 6.7).

Table 6.1 Crystal data of $Sr_{2-x}Gd_xCoO_4$ (x = 0.5, 0.75, 1, 1.25) - Space group: I4/mmm.

Atom	Samples	x	y	z	*B*iso[a]
Co	$Sr_{0.75}Gd_{1.25}CoO_4$	0	0	0	0.14
	$SrGdCoO_4$	0	0	0	0.14

	$Sr_{1.25}Gd_{0.75}CoO_4$	0	0	0	0.14
	$Sr_{1.5}Gd_{0.5}CoO_4$	0	0	0	0.14
Sr/Gd	$Sr_{0.75}Gd_{1.25}CoO_4$	0	0	0.3605	0.14(Gd) 0.14(Sr)
	$SrGdCoO_4$	0	0	0.3605	0.14(Gd) 0.14(Sr)
	$Sr_{1.25}Gd_{0.75}CoO_4$	0	0	0.3605	0.14(Gd) 0.14(Sr)
	$Sr_{1.5}Gd_{0.5}CoO_4$	0	0	0.3605	0.14(Gd) 0.14(Sr)
O (1)	$Sr_{0.75}Gd_{1.25}CoO_4$	0	0.5	0	0.32
	$SrGdCoO_4$	0	0.5	0	0.23
	$Sr_{1.25}Gd_{0.75}CoO_4$	0	0.5	0	0.28
	$Sr_{1.5}Gd_{0.5}CoO_4$	0	0.5	0	0.23
O (2)	$Sr_{0.75}Gd_{1.25}CoO_4$	0	0	0.1742	0.22
	$SrGdCoO_4$	0	0	0.1657	0.30
	$Sr_{1.25}Gd_{0.75}CoO_4$	0	0	0.1619	0.27
	$Sr_{1.5}Gd_{0.5}CoO_4$	0	0	0.1632	0.25

[a] *B*iso is an isotropic thermal parameter.

Table 6.2 Structural parameters of $Sr_{2-x}Gd_xCoO_4$ with x = 0.5, 0.75, 1, 1.25 from the Rietveld refinement (space group I4/mmm) results.

	x=0.5	x=0.75	*x=1*	*x=1.25*
a (Å)	*3.761*	*3.759*	*3.750*	*3.762*
c (Å)	*12.3669*	*12.307*	*12.163*	*12.118*
Co-O(2) (Å)	*1.881*	*1.880*	*1.875*	*1.881*
Co-O(1) (Å)	*2.019*	*1.993*	*2.015*	*2.111*
V ($Å^3$)	*175.0*	*171.9*	*171.0*	*171.5*

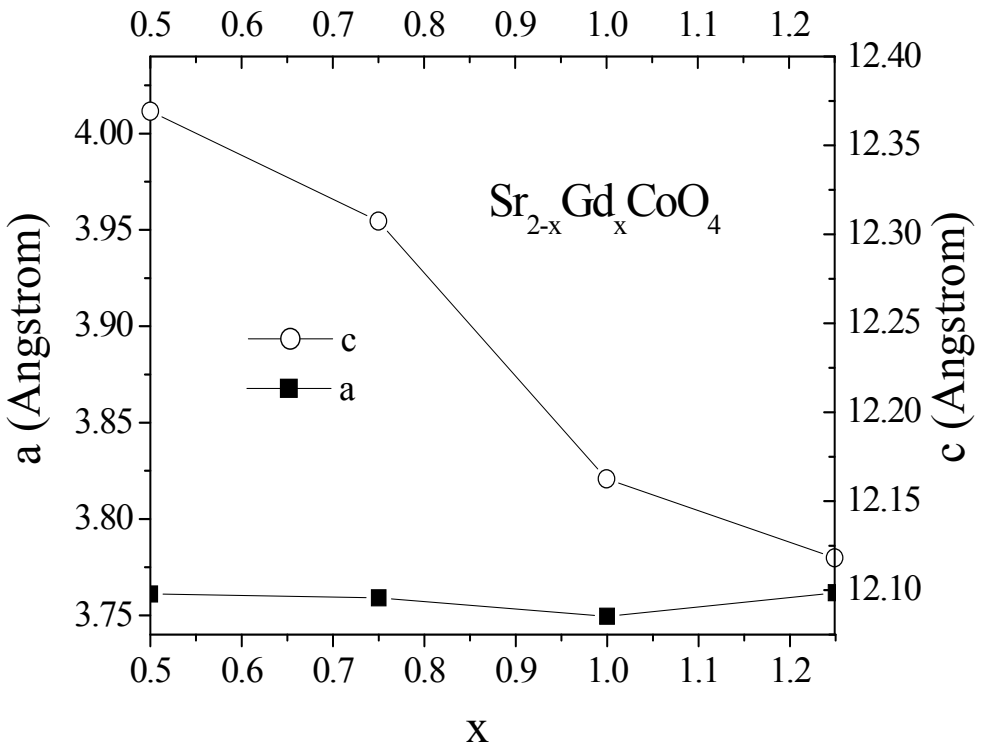

Fig. 6. 6 Lattice parameters a and c vs. x for $Sr_{2-x}Gd_xCoO_4$.

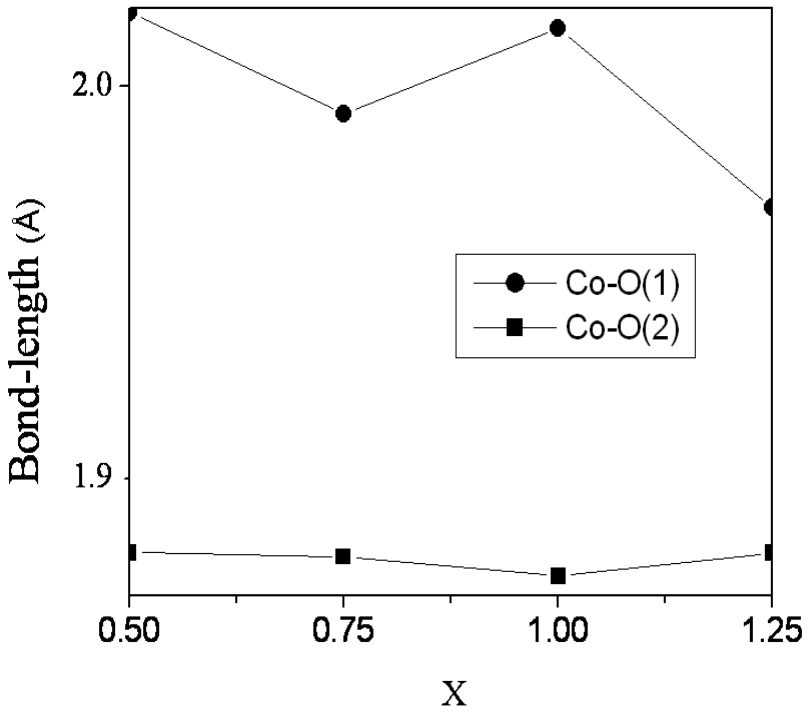

Fig. 6. 7 Co-O bond lengths vs. doping level x.

6.3 TRANSPORT PROPERTIES

The temperature dependence of the electrical resistivity in the temperature range from 25 K to 350 K for the $Sr_{2-x}Gd_xCoO_4$ samples with x = 0.75, 1, and 1.25 is shown in Fig. 6.8. The resistivity of all these samples in temperatures below 25 K became too large that they were beyond the measurable range of the PPMS. All three samples exhibited semiconductor-like behavior over the measurable range of temperatures below 350 K. The resistivity of the sample with x = 0.75 is in the typical conductor range at higher temperatures. For example, for temperatures greater than 200 K, the resistivity of this sample is less than 10 Ohm-cm. The resistivity of samples increases with increasing Gd doping level over the entire temperature range. At room temperature, the resistivities for the x = 0.75, 1, and 1.25 samples are about 2.5, 119, and 263 Ohm-cm, respectively.

The log of the resistivity (ρ) vs. $\exp(1/T)^{1/3}$ for the $Sr_{2-x}La_xCoO_4$ samples with x = 0.75, 1, and 1.25 is shown in Fig. 6.9. It can be seen that the data for the sample with x = 1.25 fit well with the VRH model in the range of 170 K to 350 K (where $0.14 < (1/T)^{1/3} < 0.18$). For the samples with x = 1 and 0.75, the data fit well to the VRH model for the entire measured temperature range.

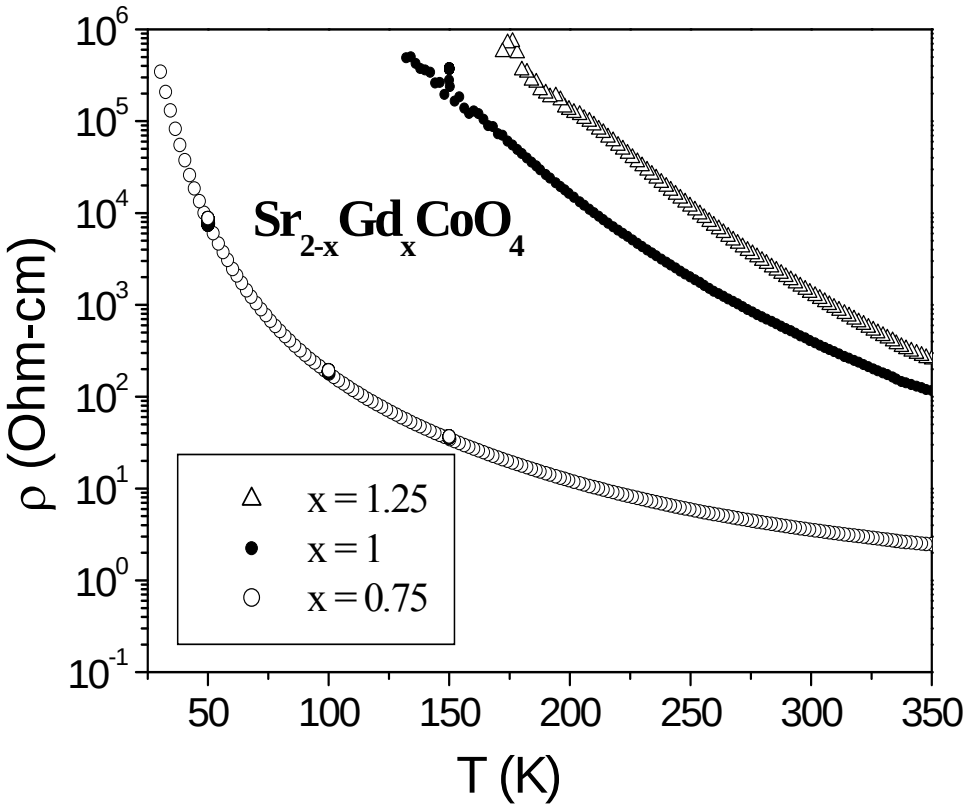

Fig. 6. 8 Temperature dependence of the resistivity of $Sr_{2-x}Gd_xCoO_4$ with x = 0.75, 1, 1.25.

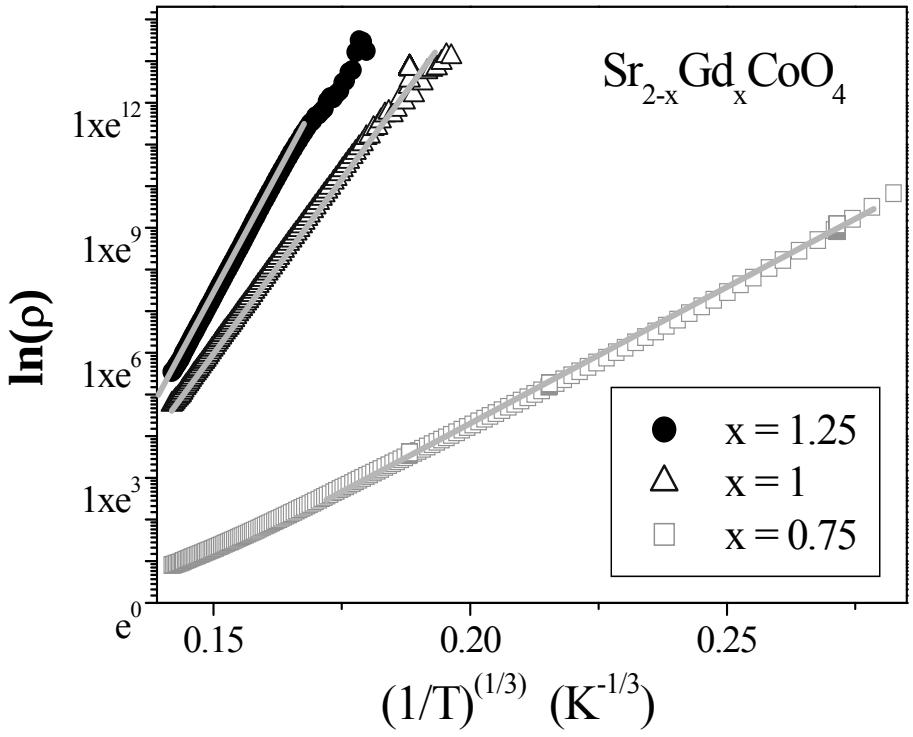

Fig. 6. 9 ln(ρ) vs exp(1/T)$^{1/3}$ for $Sr_{2-x}Gd_xCoO_4$ with x = 0.75, 1, 1.25. Straight lines are linear fittings to the 2D VRH model.

6.4 MAGNETIZATION PROPERTIES

Fig. 6.10 shows the temperature dependence from 5 K to 340 K of the magnetization of the $Sr_{2-x}Gd_xCoO_4$ samples with x = 0.75 and 1, measured in a magnetic field of 0.2 Tesla. Both samples appear to be in the paramagnetic state over the whole measured temperature range. The x = 1 sample shows typical features of a paramagnet.

Fig. 6.11 shows the temperature dependence of the inverse susceptibility (χ^{-1}) for the samples with x = 0.75 and 1, measured at a magnetic field of 0.2 T. A slight concavity

in the temperature dependence is observed at around 120 K for the sample with x = 0.75, indicating a short range ferromagnetic state change at this point for this compound.

Magnetization hysteresis measurements for the $Sr_{2-x}Gd_xCoO_4$ samples with x = 0.75 and 1, measured at 10 K, are shown in Fig. 6.12. As expected, no magnetic hysteresis is observed for either sample. However, the x = 1 sample shows typical features of paramagnetism, while the x = 0.75 sample exhibits a weak ferromagnetic interaction in the low field range, which is in agreement with what is expected from the temperature dependence of the magnetization.

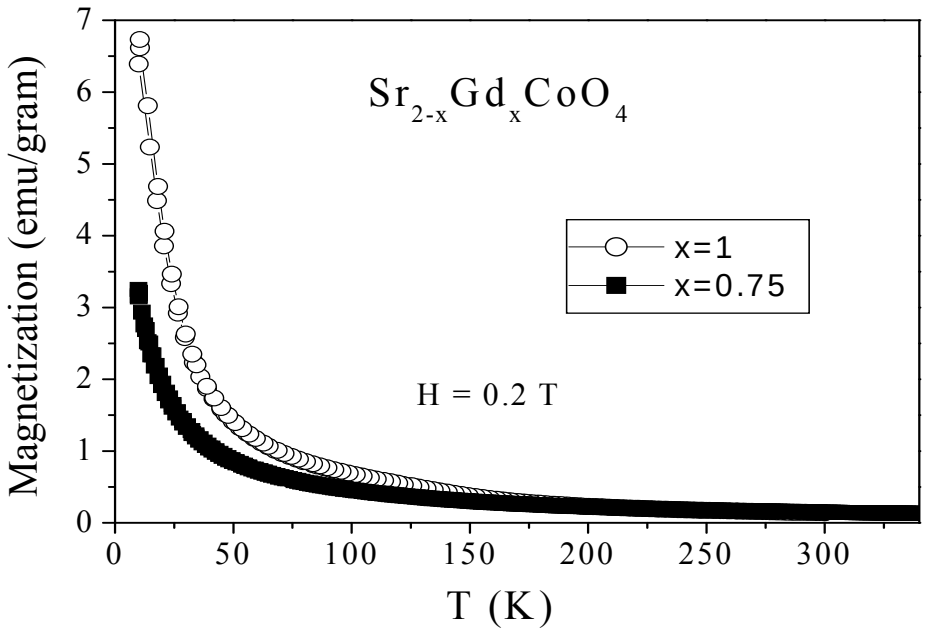

Fig. 6. 10 Temperature dependence of the magnetization for $Sr_{2-x}Gd_xCoO_4$ with x = 0.75 and 1.

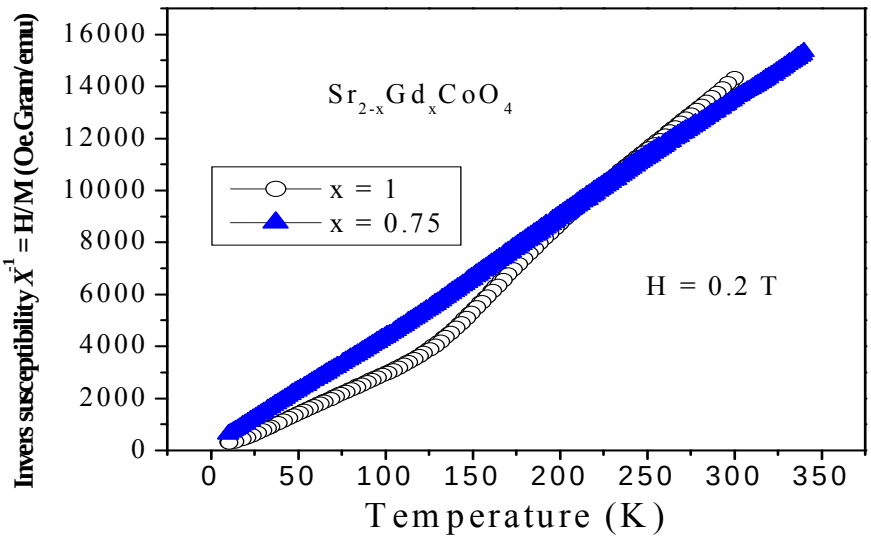

Fig. 6. 11 Temperature dependence of the inverse susceptibility (χ^{-1}) for $Sr_{2-x}Gd_xCoO_4$, measured at a magnetic field of 2000 Oe.

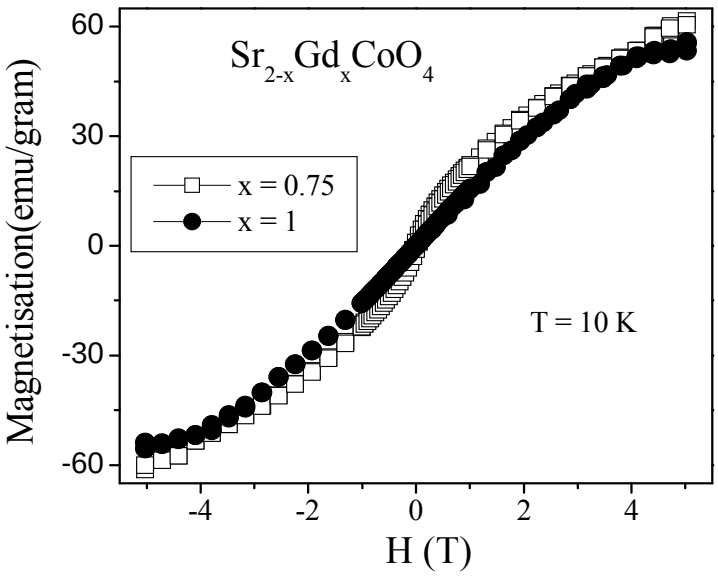

Fig. 6. 12 Magnetization hysteresis measurements for $Sr_{2-x}Gd_xCoO_4$ with x = 0.75 and 1, measured at 10 K.

6.5 MAGNETORESISTANCE

Figs. 6.13 and 6.14 show the field dependence of the magnetoresistance (MR) effect measured at a temperature of 100 K (defined as (ρ(*H*) - ρ(*H*=0)) /ρ(*H*=0)) for the samples with x = 0.75 and 1, respectively. As expected, these samples have small MRs that are less than 5%. It is interesting to note that although the MR is only 3 or 5%, both compounds are dominated by the paramagnetic state, especially for the x = 1 sample, which is a pure paramagnetic semiconductor.

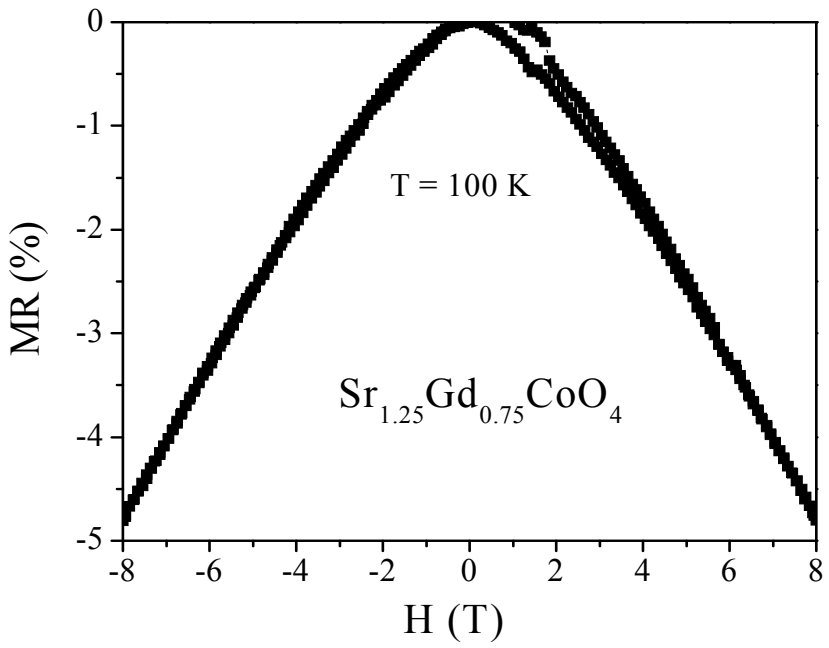

Fig. 6. 13 Magnetoresistance hysteresis for $Sr_{1.25}Gd_{0.75}CoO_4$ at 100 K.

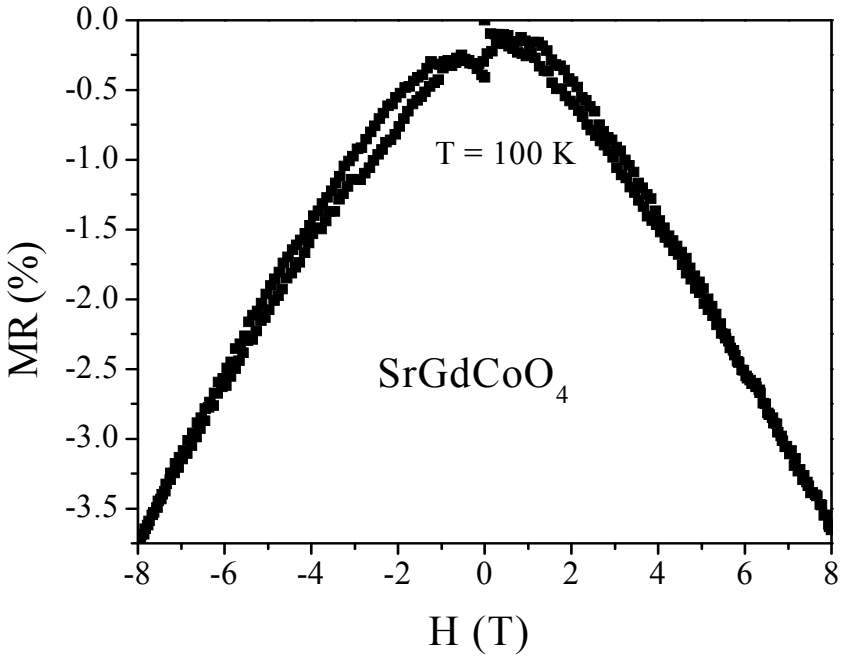

Fig. 6. 14 Magnetoresistance hysteresis for $SrGdCoO_4$ at 100 K.

The band structure of the $Sr_{1.5}Gd_{0.5}CoO_4$ sample was obtained by first-principles calculations in the framework of density functional theory (Fig. 6.15). The calculations were performed using the plane-wave pseudo-potential method based on density functional theory (DFT) with the generalized gradient approximation (GGA) in the scheme of Perdew-Burke-Ernzerhof. The ion-electron interaction was modeled by ultra-soft Vanderbilt-type pseudo-potentials. An experimental lattice parameter obtained through structure refinement was used in this calculation.

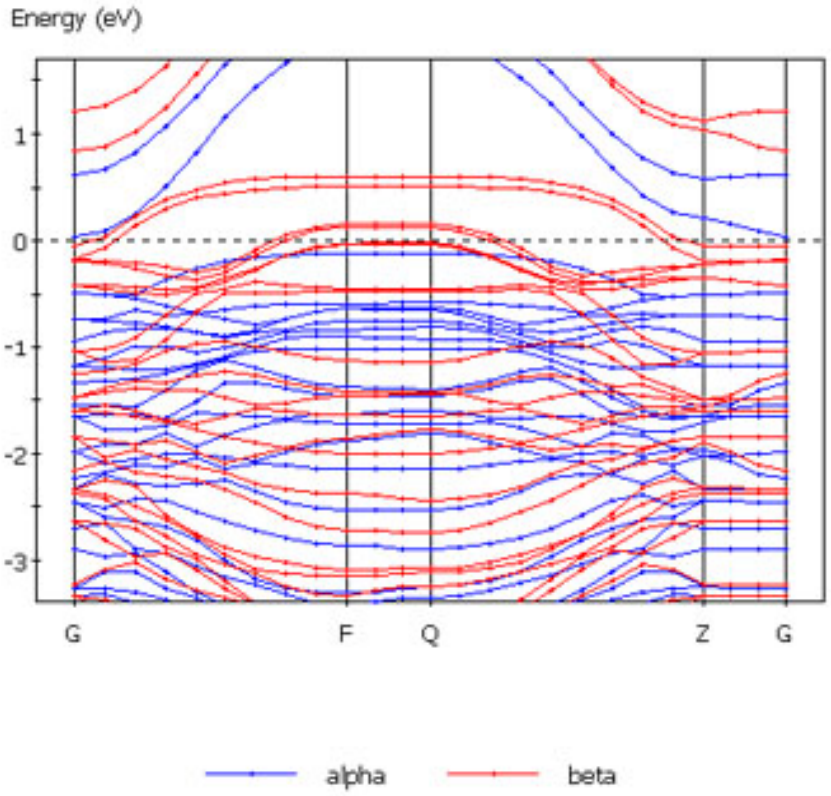
Energy (eV)
1
0
-1
-2
-3
G
F
Q
Z
G
alpha
beta

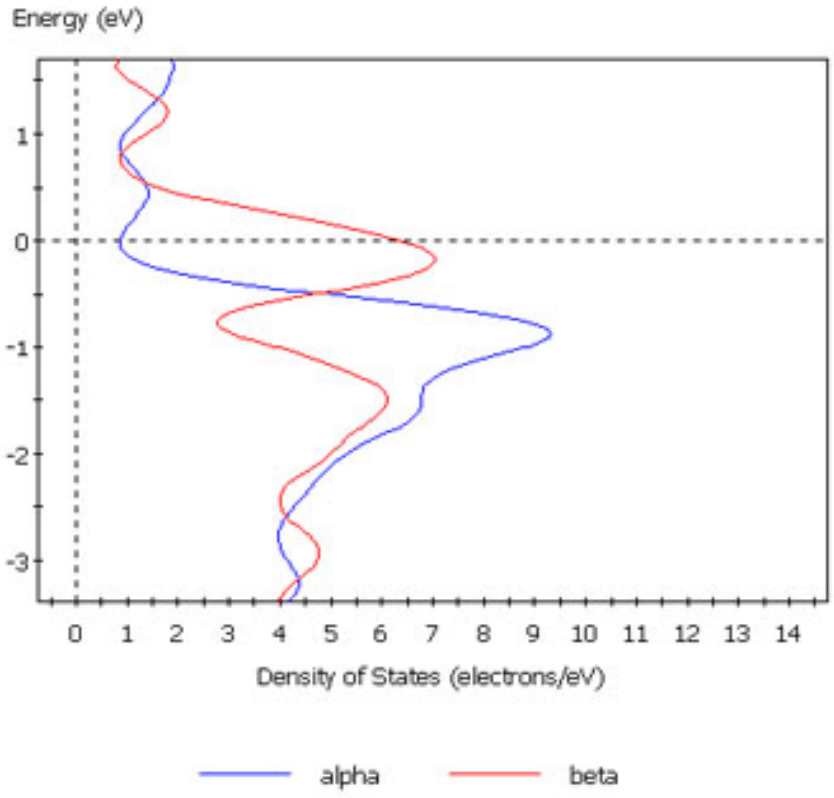
Energy (eV)
1
0
-1
-2
-3
0 1 2 3 4 5 6 7 8 9 10 11 12 13 14
Density of States (electrons/eV)
alpha
beta

Fig. 6. 15 The band structure (upper panel) and density of states (lower panel) of the $Sr_{1.5}Gd_{0.5}CoO_4$ sample.

The band structure and DOS clearly show that the material is metallic, as evidenced by the large number density of states penetrating the Fermi surface. Furthermore, the electrons around the Fermi surface are mainly spin-down electrons, indicating a strong half-metallic nature.

The partial density of states of Co (Fig. 6.16) shows that the density of states for both the majority and minority carriers around the Fermi surface arises from the 3d electrons of Co. The half-metallic nature of this compound is also determined by the Co 3d electrons.

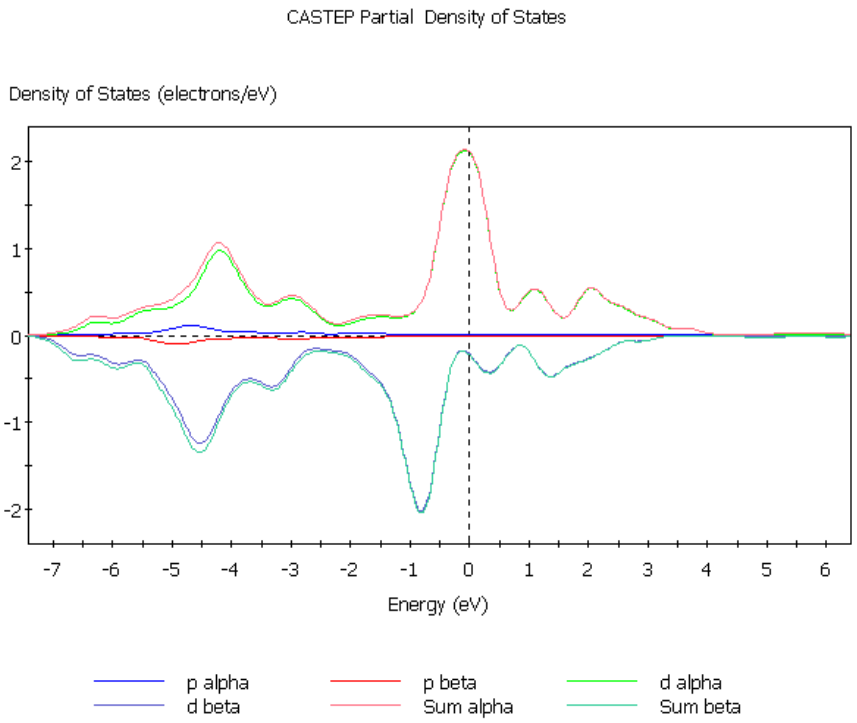

Fig. 6. 16 Partial density of states of Co in the $Sr_{1.5}Gd_{0.5}CoO_4$ sample.

6.6 SUMMARY

The Gd-doped Sr_2CoO_4 samples were found to be paramagnetic semiconductors with MR of only 3 or 5%. Their transport properties can be described by the hopping model for semiconductors. Band structure calculations indicate that the spin polarization is high in the Gd-doped Sr_2CoO_4.

CHAPTER 7. ND DOPED Sr_2CoO_4 ($Sr_{2-x}Nd_xCoO_4$, x = 0.5, 0.75, 1, 1.25)

7.1 INTRODUCTION

Polycrystalline samples of $Sr_{2-x}Nd_xCoO_4$ (x = 0.5, 0.75, 1, 1.25) were synthesized by a conventional solid-state reaction method, as described in section II. Powders of Nd_2O_3, $SrCO_3$, and Co_3O_4 with high purity were used as starting materials. The phases and structures of the resulting samples were studied at room temperature using x-ray powder diffraction (XRD). Structure refinements were carried out by the Rietveld method using the RIETICA program. Magnetic and electrical transport properties were investigated using commercial Quantum Design Magnetic and Physical Properties Measurement Systems (MPMS and PPMS) over a temperature range from 5 to 350 K, and in magnetic fields up to 8 Tesla.

7.2 STRUCTURAL PROPERTIES

The XRD patterns of the $Sr_{2-x}Nd_xCoO_4$ samples (where x = 0.5, 0.75, 1, 1.25) for the 2 θ range from 30 to 70 degrees, measured at room temperature, are shown in Fig. 7.1. It can be seen that the diffraction peaks of all the four samples fit well with the of the Sr_2CoO_4 single phase XRD pattern. However there is a peak of an unknown impurity that appears in the range of 32.5 to 33 degrees in the XRD patterns. For the three samples where x = 0.5, 0.75, and 1, the unknown peak is marked with an asterisk. The sample with x = 1.25 is a single phase compound with the structure of Sr_2CoO_4.

Rietveld refinement was carried out based on the XRD results for all four samples. They are shown in Figs. 7.2, 7.3, 7.4 and 7.5, respectively. The observed (crosses), calculated (solid lines), and difference diffraction (bottom lines) profiles are plotted in each figure. It can be seen that the calculated results match well with the experimental data for all the samples. Our refinement shows that these samples have the basic K_2NiF_4 structure.

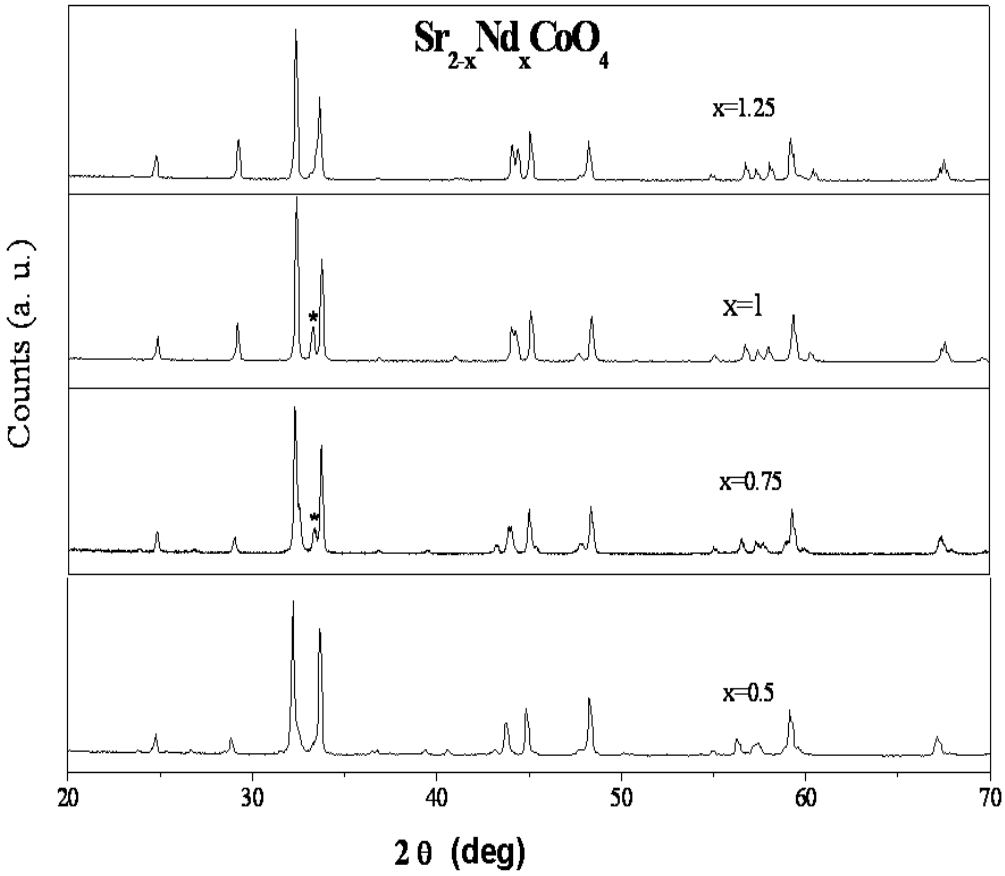

Fig. 7. 1 XRD patterns of $Sr_{2-x}Nd_xCoO_4$ with x = 0.5, 0.75, 1, 1.25.

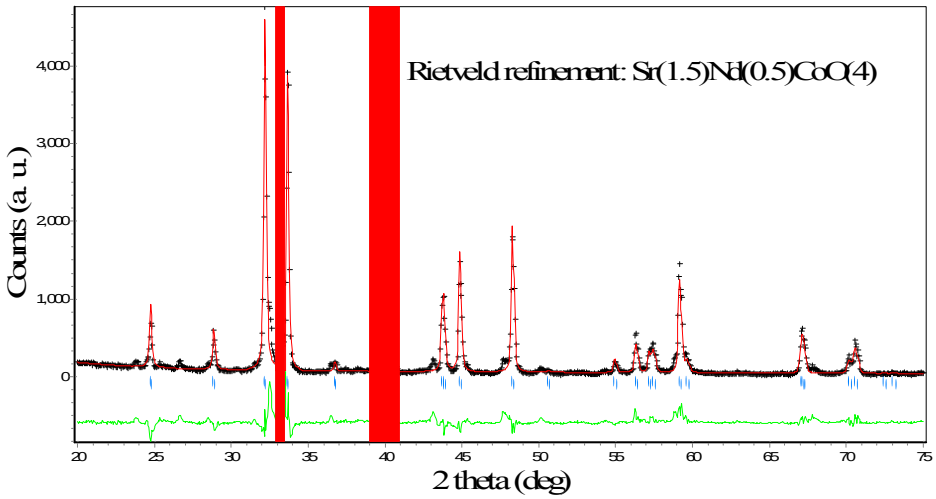

Fig. 7. 2 Rietveld refinement for $Sr_{1.5}Nd_{0.5}CoO_4$ showing the observed (crosses), calculated (solid line) and difference (bottom line) profiles at 300K for the x = 0.5 sample (refinement factors Rp=14. 9%, Rb=7.4%; blue-strip ranges were ignored in refinement).

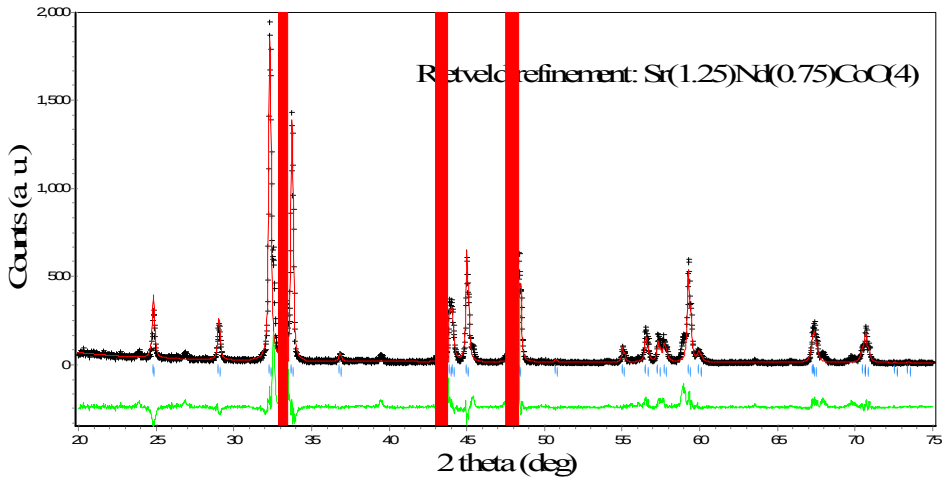

Fig. 7. 3 Rietveld refinement for $Sr_{1.25}Nd_{0.75}CoO_4$ shpwing the observed (crosses), calculated (solid line) and difference (bottom line) profiles at 300K for the x = 0.75 sample (refinement factors Rp=18. 4%, Rb=11.5%; blue-strip ranges were ignored in refinement).

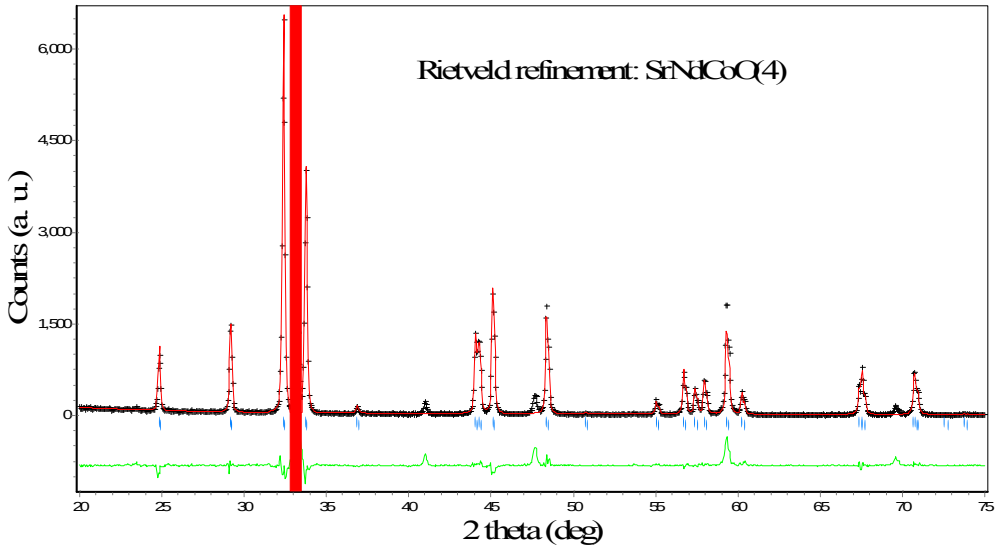

Fig. 7. 4 Rietveld refinement for $SrNdCoO_4$ showing the observed (crosses), calculated (solid line) and difference (bottom line) profiles at 300K for the x = 1 sample (refinement factors Rp=10. 9%, Rb=6.4%; blue-strip range was ignored in refinement).

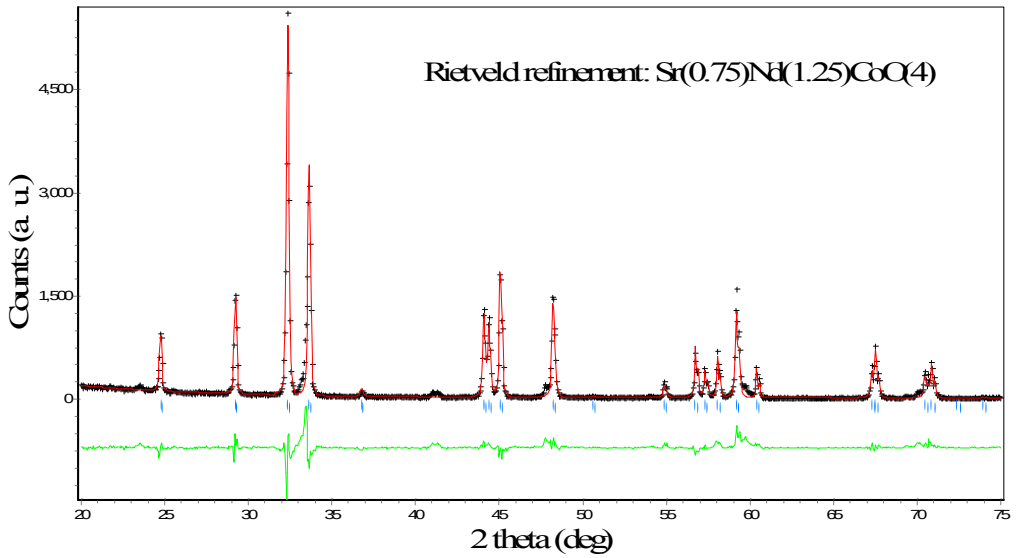

Fig. 7. 5 Rietveld refinement for $Sr_{0.75}Nd_{1.25}CoO_4$ showing the observed (crosses), calculated (solid line) and difference (bottom line) profiles at 300K for the x = 1 sample (refinement factors Rp=13. 9%, Rb=8.4%).

The atomic parameters, isotropic temperature factors, Co-O bond lengths and unit cell volumes obtained from the refinement results are summarized in Tables 7.1 and 7.2.

From Table 7.1, we can see that the atomic position for Sr/Nd is not sensitive to the Nd doping level. However, the O2 position changes for each of the doping levels.

The refined results for lattice parameters *a* and *c* are plotted in Fig. 7.7. It can be seen clearly that lattice parameter *a* is not sensitive to the doping level of Nd and remains around 3.7 Å for the different doping levels x, while lattice parameter *c* decreases as the doping level x increases This is in agreement with the fact that the ion size of Nd^{3+} (radius 0.98 Å) is smaller than the ion size of Sr^{2+} (radius 1.32 Å).

The value for the in-plane Co-O(2) bond length are almost the same, around 1.8 Å for all the doping levels, while the out-of-plane Co-O(1) bond length values vary for different doping level x.

Fig. 7.6 shows the Co-O(1) and Co-O(2) bond lengths vs. the doping level x. It can be seen that all the samples' out-of-plane Co-O(1) bond lengths are greater than their corresponding in-plane bond lengths. This indicates that the Nd doping causes a distortion of the CoO_6 octahedron with elongation along the *c*-axis (the Co-O(1) direction). Fig. 7.8 shows the unit cell volume vs. x for $Sr_{2-x}Nd_xCoO_4$. Generally speaking, the Nd doping reduces the unit cell volume of S_2CoO_4.

Table 7.1 Crystal data of $Sr_{2-x}Nd_xCoO_4$ (x = 0.5, 0.75, 1, 1.25) - Space group: I4/mmm.

Atom	Samples	x	y	z	*B*iso[a]

Co	$Sr_{0.75}Nd_{1.25}CoO_4$	0	0	0	0.14
	$SrNdCoO_4$	0	0	0	0.14
	$Sr_{1.25}Nd_{0.75}CoO_4$	0	0	0	0.14
	$Sr_{1.5}Nd_{0.5}CoO_4$	0	0	0	0.14
Sr/Nd	$Sr_{0.75}Nd_{1.25}CoO_4$	0	0	0.3605	0.14(Nd) 0.14(Sr)
	$SrNdCoO_4$	0	0	0.3605	0.14(Nd) 0.14(Sr)
	$Sr_{1.25}Nd_{0.75}CoO_4$	0	0	0.3605	0.14(Nd) 0.14(Sr)
	$Sr_{1.5}Nd_{0.5}CoO_4$	0	0	0.3605	0.14(Nd) 0.14(Sr)
O (1)	$Sr_{0.75}Nd_{1.25}CoO_4$	0	0.5	0	0.26
	$SrNdCoO_4$	0	0.5	0	0.27
	$Sr_{1.25}Nd_{0.75}CoO_4$	0	0.5	0	0.32
	$Sr_{1.5}Nd_{0.5}CoO_4$	0	0.5	0	0.32
O (2)	$Sr_{0.75}Nd_{1.25}CoO_4$	0	0	0.1618	0.33
	$SrNdCoO_4$	0	0	0.1625	0.31
	$Sr_{1.25}Nd_{0.75}CoO_4$	0	0	0.1568	0.26
	$Sr_{1.5}Nd_{0.5}CoO_4$	0	0	0.1640	0.28

Table 7.2 Structural parameters of $Sr_{2-x}Nd_xCoO_4$ with x = 0.5, 0.75, 1, 1.25 from the Rietveld refinement (space group I4/mmm) results.

	x=0.5	x=0.75	*x=1*	*x=1.25*
a (Å)	*3.776*	*3.774*	*3.774*	*3.783*
c (Å)	*12.417*	*12.370*	*12.313*	*12.275*
Co-O(2) (Å)	*1.888*	*1.887*	*1.887*	*1.891*
Co-O(1) (Å)	*2.036*	*1.939*	*2.001*	*1.986*
V ($Å^3$)	*177.1*	*176.2*	*175.4*	*175.6*

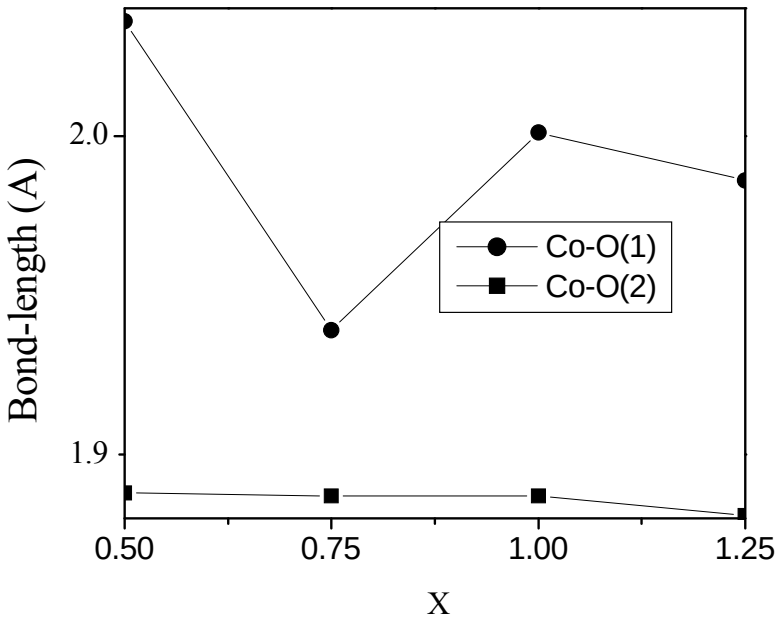

Fig. 7. 6 Co-O bond lengths v.s doping level x

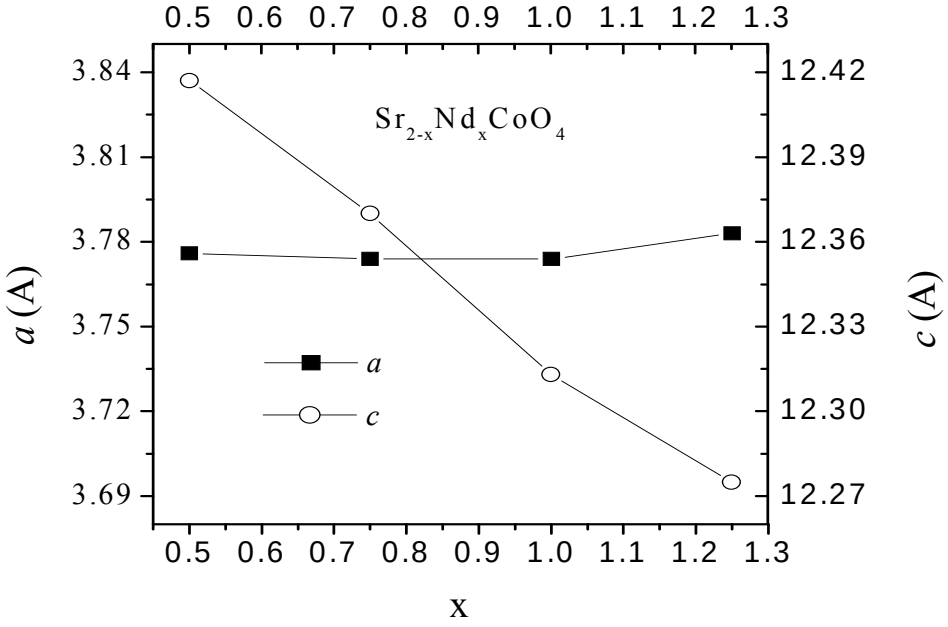

Fig. 7. 7 Lattice parameters a and c vs. x for $Sr_{2-x}Nd_xCoO_4$.

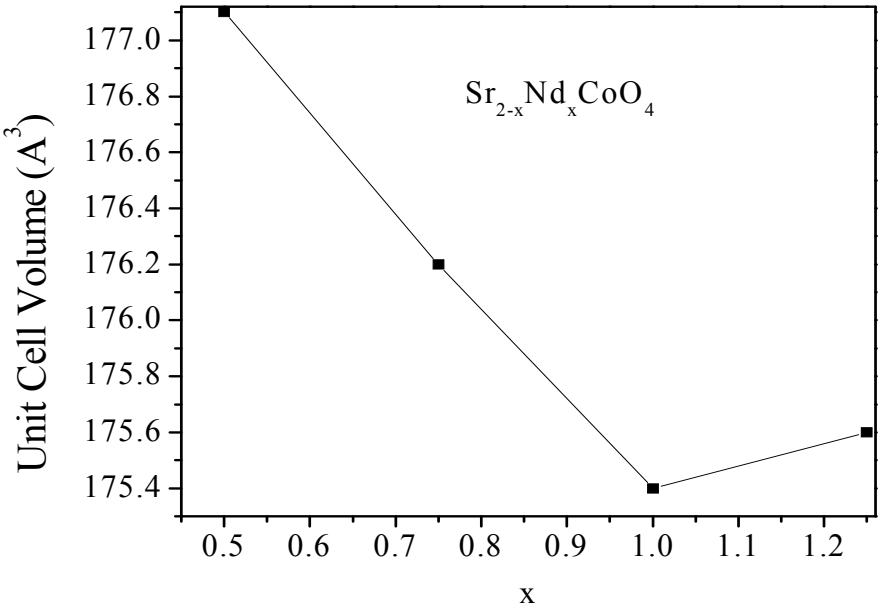

Fig. 7. 8 The unit cell volume vs. x for $Sr_{2-x}Nd_xCoO_4$.

7.3 TRANSPORT PROPERTIES

The temperature dependence of the electrical resistivity in a temperature range of 5 K to 340 K for the $Sr_{2-x}Nd_xCoO_4$ samples with x = 0.75 and 1 is shown in Fig. 7.9. The resistivity of the x = 1 sample is always greater than the resistivity of the sample with x = 0.75 at the same temperature. This clearly indicates that the Nd doping increases the resistivity of the compound. At room temperature, 300 K, the resistivity for the samples with x = 0.75 and 1 are 0.6 and 4 Ohm-cm, respectively. Both samples show semiconductor-like behaviour over the whole measured temperature range.

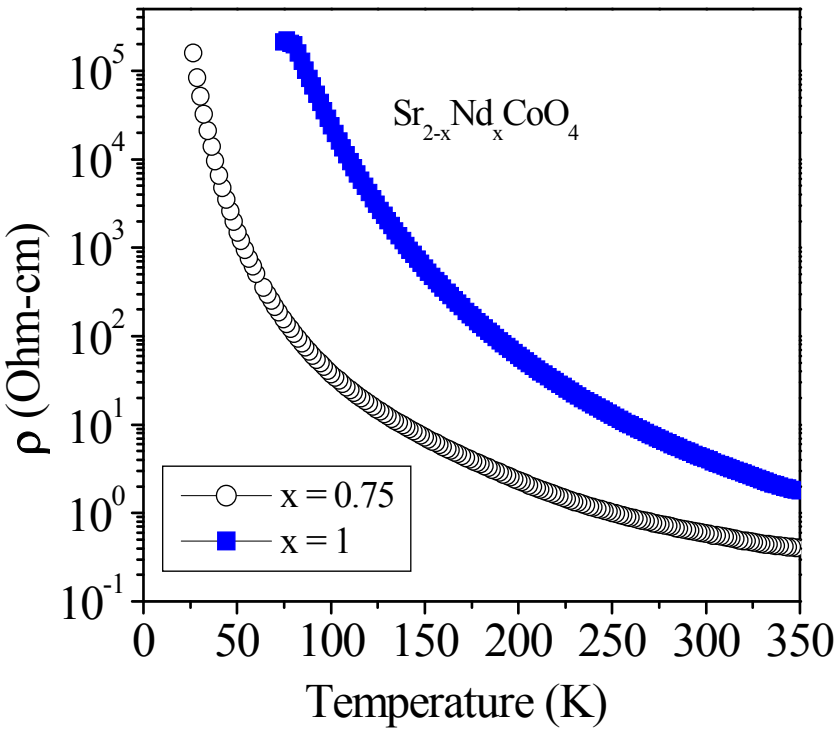

Fig. 7. 9 Resistance vs. temperature for $Sr_{2-x}Nd_xCoO_4$ (x = 0.75, 1).

The log of the resistivity (ρ) vs. $\exp(1/T)^{1/3}$ for the $Sr_{2-x}Nd_xCoO_4$ samples with x = 0.75 and 1 is shown in Fig. 7.10. Both samples can be well fitted by the VRH model $\rho = \rho_o \exp(T_0/T)^{1/3}$. This again suggests that the 2D variable-range hopping (VRH) mechanism could be used to account for the conducting mechanism for both of these samples.

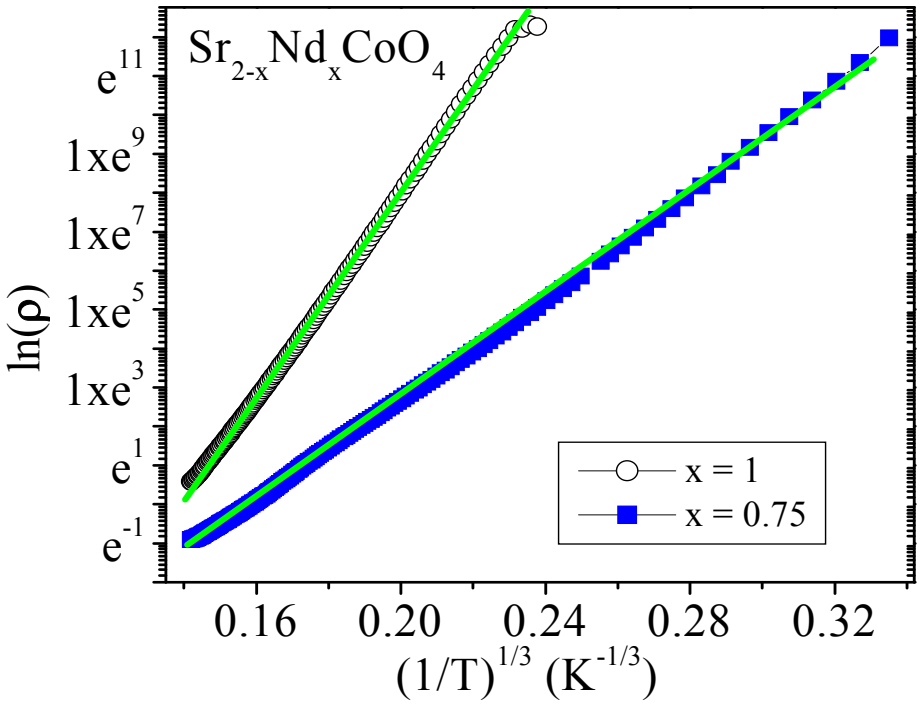

Fig. 7. 10 ln(ρ) vs. exp(1/T)$^{1/3}$ for $Sr_{2-x}Nd_xCoO_4$ (x = 0.75, 1). Straight lines are linear fittings to the 2D VRH model.

7.4 MAGNETIZATION PROPERTIES

Fig. 7.11 shows the temperature dependence for field-cooled and zero-field-cooled measurements from 5 K to 340 K of the magnetization of the $Sr_{2-x}Nd_xCoO_4$ samples with x = 0.75 and 1, measured in a magnetic field of 0.2 Tesla. It is obvious that both of the samples are ferromagnetic in the low temperature range. Samples exhibit a paramagnetic to ferromagnetic transition at temperatures of about 250, 170 K for the x = 1 and 0.75 samples, respectively, It is observed that the Nd doping in $Sr_{2-x}Nd_xCoO_4$ drives the critical temperature to a higher value. The magnetization value at 100 K is 0.7 emu/gram for the x = 0.75 sample and 2.9 emu/gram for the sample with x = 1.

It should be noted that the resistivity monotonically increases with decreasing temperature from 340 to 5 K (Fig. 7.8), and no anomaly occurs at magnetic transition temperatures for either of the samples with x = 0.75 and 1. Both show a semiconducting character. This reveals that the variation in the resistivity with temperature for these compounds is not dominated by spin-dependent scattering of carriers, but by carrier concentration. [94]

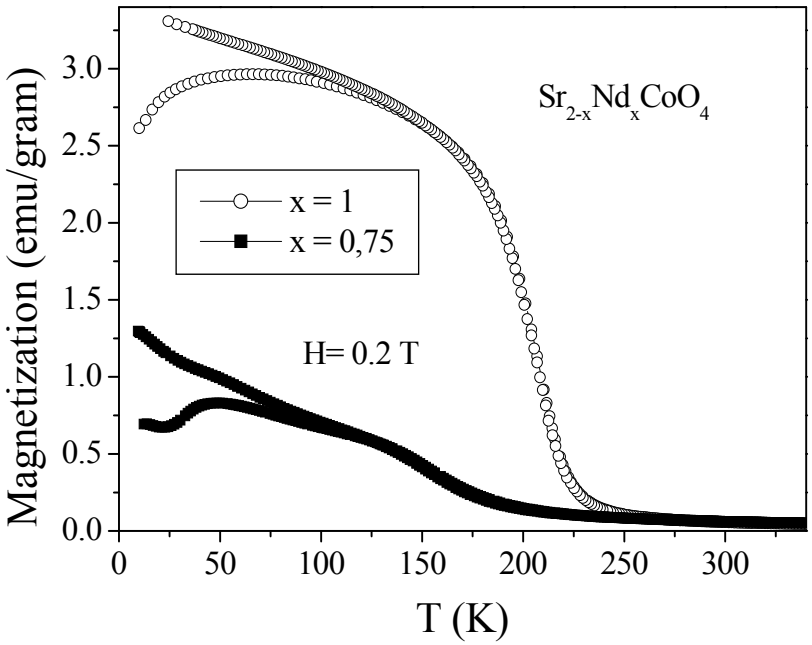

Fig. 7. 11 The temperature dependence from 10 K to 340 K of the magnetization of the $Sr_{2-x}Nd_xCoO_4$ samples with x = 0.75, 1, measured in a magnetic field of 0.2 Tesla.

Fig. 7.12 shows the temperature dependence of the inverse susceptibility (χ^{-1}) for $Sr_{2-x}Nd_xCoO_4$, measured at a magnetic field of 2000 Oe. From this figure, the Curie-Weiss

temperatures obtained by fitting to the Curie Weiss linear law were found to be 130 K, 210 K, for the samples with x = 0.75 and 1, respectively.

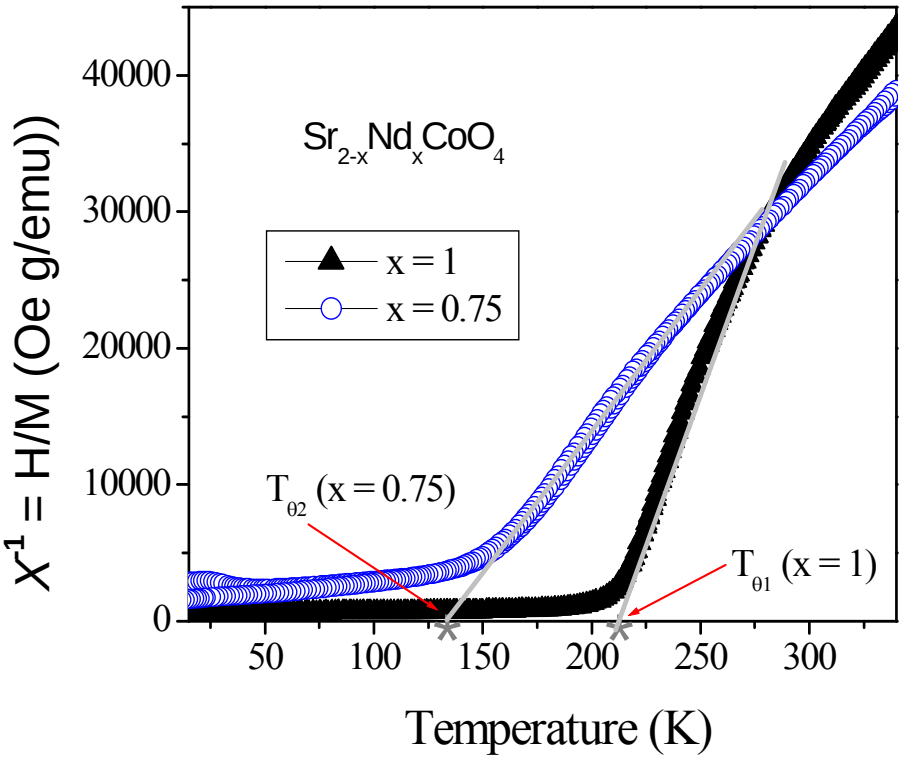

Fig. 7. 12 Temperature dependence of the inverse susceptibility (χ^{-1}) for $Sr_{2-x}Nd_xCoO_4$, measured at a magnetic field of 2000 Oe.

The magnetic hysteresis (MH) loops for the $Sr_{2-x}Nd_xCoO_4$ samples with x = 0.75 and 1, measured at 10 K are shown in Fig. 7.13. The x = 0.75 sample shows a large coercive field of about 0.5 Tesla. This implies large crystal anisotropy energy. As for the sample with x = 0.75, its coercive field is about 0.21 Tesla. The magnetization values at 5 Tesla and 10 K for the $Sr_{2-x}Nd_xCoO_4$ sample with x = 0.75, 1 are around 12 emu/gram for both of them.

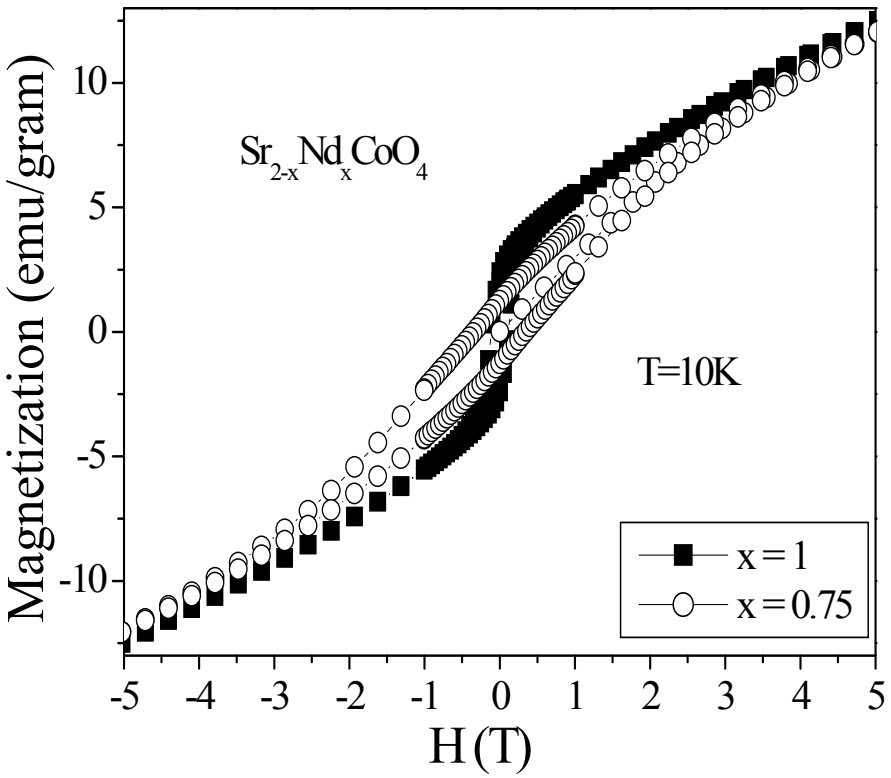

Fig. 7. 13 Magnetic hysteresis loops for $Sr_{2-x}Nd_xCoO_4$ with x = 0.75, 1.

7.5 MAGNETORESISTANCE

Figs. 7.14 and 7.15 show the field dependence of the magnetoresistance (MR) effect, measured at a temperature of 100 K (defined as (ρ(*H)* - ρ(*H*=0)) /ρ(*H*=0)) for the samples with x =1 and 0.75, respectively. These samples have small MRs that are less than 5%.

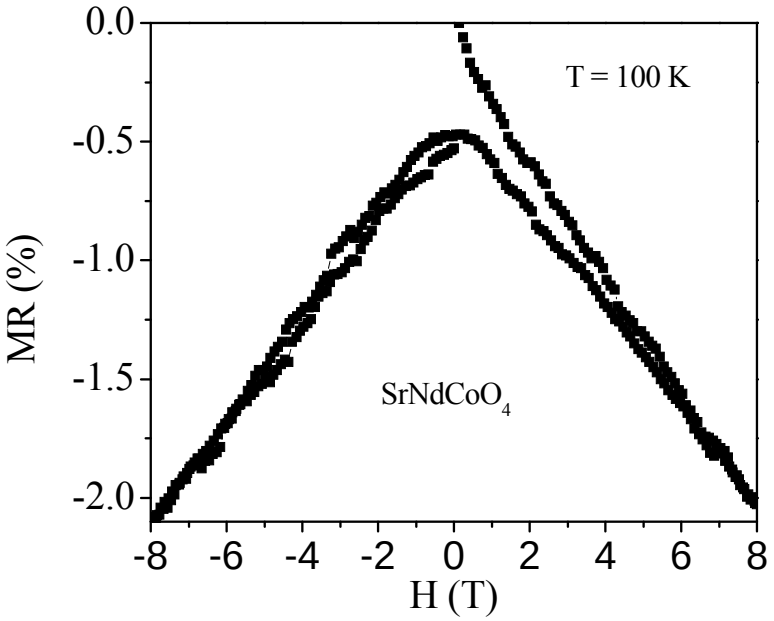

Fig. 7. 14 Magnetoresistance hysteresis for $SrNdCoO_4$ at 100 K.

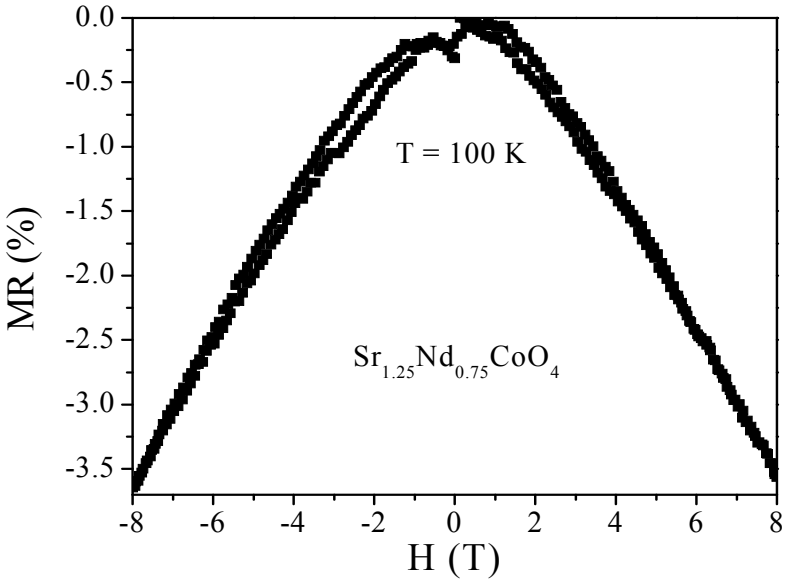

Fig. 7. 15 Magnetoresistance hysteresis for $Sr_{1.25}Nd_{0.75}CoO_4$ at 100 K.

7.6 SUMMARY.

Nd doped compounds become ferromagnetic semiconductors at temperatures of about 250 and 170 K for the x = 1 and 0.75 samples, respectively. Their MR values are about 5 %, the same as for Gd-doped samples. The Nd doping raises the Curie temperature of Sr_2CoO_4, and it reaches 210 K for doping with Nd up to 50%.

CHAPTER 8. SUMMARY FOR VARIES DOPED COMPOUNDS

A summary of the properties for the different doped compounds is presented in Table 8.1.

Table 8.1 Summary of the properties for different doped compounds.

Values for x = 1	Pr doped	La doped	Eu doped	Gd doped	Nd doped
Doped-ion radii Sr2+ 1.32 Å	Pr3+ 1.06 Å	La3+ 1.03 Å	Eu2+ 0.95 Å	Gd3+ 0.94 Å	Nd3+ 0.98 Å
a (Å)	3.78	3.80	3.77	3.75	3.77
c (Å)	12.35	12.49	12.17	12.16	12.31
Co-O(2) (Å)	1.89	1.90	1.88	1.88	1.89
Co-O(1) (Å)	1.92	1.99	1.97	2.02	2.00
V ($Å^3$)	176.6	180.8	171.8	171.0	175.4
X values for single 214 phase	0.5 – 1.5	1 – 1.25	0.75 - 1	non	1.25
Ferromagnetic behavior	X=0.25-0.75	X=0.75-1.25	X=0.75-1, but negligible	negligible	X=0.75-1
Resistivity behaviour	Semiconductive 1000 Ohm.cm at room temp	Semiconductive, 10 Ohm-cm at	Semiconductive, 1060 Ohm-cm at	Semiconductive, 360 Ohm-	Semiconductive, 4 Ohm-cm at room

		room temp	room temp	cm at room temp	temp
Coercive field (T)	1 T (x=0.5)	1 T (x=0.75)	negligible	negligible	0.75 T (x=0.75)
MR Values	Not available	≤7% for T below 150K	Large MR values found (up to 48%)	≤5% for T below 100K	≤5% for T below 100K
Dielectric constant	Above 2000 at 1 kHz	Not available	Not available	Not available	Not available

From Table 8.1, it is observed that lattice parameter *a* remains relatively stable around the value of 3.7 to 3.8 Å for x = 1, for various RE doping compounds of $Sr_{2-x}RE_xCoO_4$. The Co-O(2) in-plane bond length was also not sensitive to the particular type of RE doping, for the x = 1 doping level. However, lattice parameter *c*, as well as the out-of-plane bond length Co-O(1), varies with different RE doping, for the doping level of x = 1, and consequently, the unit cell volume also changes with the type of RE doping.

Among the various RE dopings that we have examined, we have only presented five types of doping in this thesis, as these five types of doping seem to have the best potential for applications. We have found that Sr_2CoO_4 compound is most tolerant to Pr doping. For x value from 0.5 to 1.5, we can achieve single phase Sr_2CoO_4 structured samples, while La doping could achieve a single phase compound for x = 1 – 1.25 and, for Eu doping, single phase compounds are formed for x = 0.75 – 1. For both Gd and Nd doping compounds, near single phase is formed for all the tested x values (x = 0.5 –

1.25), but an extra unknown peak is found im the 2 θ range of 32.5 to 33 degrees in the XRD patterns. The 2D VRH mechanism is only observed for compounds in a relatively high resistivity state. The VRH model does not apply to some of the compounds with very low resistivity.

FURTHER WORK

It would be useful to examine more of the detailed trends in changes to each of the RE doped Sr_2CoO_4 compound series, by adding more intermediate values of x to each of the doped compounds. For example, for the Pr doped compounds, x values can be chosen to have these values for a more detailed study of this compound: x = 0.25, 0.375, 0.5, 0.625, 0.75, 0.875, 1, 1.125, 1.25, 1.375, 1.5. The same is true for the other RE doped series.

PUBLICATION LIST

1. Q.W. Yao, X.L. Wang, J. Horvat, S.X. Dou, "Cu and nano-SiC doped MgB_2 thick films on Ni substrates processed using a very short-time in situ reaction,", Physica C, 402 (2004) 38-44.

2. Q.W. Yao, X.L. Wang, S. Soltania, A.H. Li, J. Horvat, and S.X. Dou, "Fabrication, microstructure and critical current density of pure and Cu doped MgB_2 thick films on stainless substrate by short-time in-situ reaction," Ceramic International, 30 (2004) 1603-1606.

3. Q.W. Yao, X.L. Wang, P.R. Munroe, and S.X. Dou, "Effect of nano-Y-ZrO_2 addition on the microstructure and critical current density of MgB_2 superconductors", International Journal of Nanoscience. 4&5 (2004) 1-7.

4. Q.W. Yao, X.L. Wang, S. Soltania, A.H. Li, J. Horvat, and S.X. Dou,"Fabrication and characterization of MgB_2 thick films grown on Ag, Cu, Ni, and stainless steel substrates by in-situ reaction," presented at M2S-HTSC RIO International Conference, May 2003, Brazil. Conference Presentation.

5. Q.W. Yao, X.L. Wang and S.X. Dou, "Structure, Magnetism, and Spin Dependent Magnetoresistance in Doped Two-Dimensional Sr_2CoO_4 Compounds," 2006 International Conference on Nanoscience and Nanotechnology (3 – 7 July 2006),

Brisbane Convention & Exhibition Centre, Queensland, Australia. Conference Presentation.

6. Q.W. Yao, X.L. Wang, D.Q. Shi and S.X. Dou, "Structure, transport and magnetic properties in a new layered ferromagnetic perovskite cobalt oxide $Sr_{2-x}Pr_xCoO_4$," Physica C 460–462 (2007) 481–482.

7. Q.W. Yao, X.L. Wang, Z.X. Cheng, G. Peleckis, and S.X. Dou, "Band structure calculations, structures, magnetic, and transport properties of doped two dimensional Sr_2CoO_4," Journal of Applied Physics (2007), 101, 09N515 (2007).

8. Q. W. Yao, X.L. Wang, and S. X. Dou, "Dielectric, magnetic, and magnetotransport properties in Sr doped two-dimensional RE_2CoO_4 (RE=Pr,Eu) compounds," Journal of Applied Physics, 103, 07B904 (2008)

Some co-authored articles

1. Polyanskii, A., Wang, X., Q.W. Yao, Dou, S. X., Lin, Z. & Zhu, J. (2006). Magneto-optical imaging of the magnetization process in colossal magnetoresistive lanthanum manganite. Journal of Applied Physics, 99 (8), 08A704 (2006).

2. Alvarez, G. A., Iguchi, I., Wang, X., Dou, S. X. & Yao, Q. (2006). Spectroscopic measurements of Zeeman splitting of the density of states in high temperature superconducting tunneling junctions. Journal of Applied Physics, 99 (8), 08C912.

3. Alvarez, G. A., Iguchi, I., Wang, X., Dou, S. X. & Yao, Q. (2006). Quantum effects in small-capacitance high temperature superconducting tunneling junctions. Journal of Applied Physics, 99 (8), 08M514.

REFERENCES

[1] X. L. Wang and E. Takayama-Muromachi, Phys. Rev. B 72, 064401 (2005).

[2] W.M. Witzel and S. Das Sarma, Phys. Rev. B 76, 045218 (2007).

[3] D.J. Priour, Jr., E.H. Hwang, and S. Das Sarma, Phys. Rev. Lett. 95, 037201 (2005).

[4] S.X. Zhang, W. Yu, S.B. Ogale, S.R. Shinde, D.C. Kundaliya, W.K. Tse, S.Y. Young, J.S. Higgins, L.G. Salamanca-Riba, M. Herrera, L.F. Fu, N.D. Browning, R.L. Greene, and T. Venkatesan, Phys. Rev. B 76, 085323 (2007).

[5] E.H. Hwang and S. Das Sarma, Phys. Rev. B 72, 085455 (2005).

[6] M.J. Manfra, E.H. Hwang, S. Das Sarma, L.N. Pfeiffer, K.W. West, and A.M. Sergent, Phys. Rev. Lett. 99, 236402 (2007).

[7] S.B. Ogale, R.J. Choudhary, J.P. Buban, S.E. Lofland, S.R. Shinde, S.N. Kale, V.N. Kulkarni,J. Higgins, C. Lanci, J.R. Simpson, N.D. Browning, S. Das Sarma, H.D. Drew, R.L. Greene, and T. Venkatesan, Phys. Rev. Lett. 91, 077205 (2003).

[8] Y. G. Zhao, S.R. Shinde, S.B. Ogale, J. Higgins, S.E. Lofland, C. Lanci, J.P. Buban, N.D. Browning, S. Das Sarma, A.J. Millis, V.N. Kulkarni, R.J. Choudhary, R.L. Greene, and T. Venkatesan, App. Phys. Lett. 83, 2199 (2003).

[9] S Young, D-Q Liao, R-F Yang, Z-H Cheng. Physica B, vol.394 (2007).

[10] H Dery, P Dalal, L Cywinski, LJ Sham. Nature,.447, 7144, (2007).

[11] Kavli Inst. for Theor. Phys., Phys. Rev. B, 71, (2005).

[12] N. Samarth. Nature Mat., 6, 6, (2007).

[13] Norberg NS, Dalpian GM, Chelikowsky JR, Gamelin DR. Nano Lett., 6, 12, (2006).

[14] GY Gao, KL Yao, ZL Liu, YL Li, JL Jiang, YC Li. Physica B, 382, (2006).

[15] W Gehlhoff, D Azamat, A Hoffmann, N Dietz, OV Voevodina. Physica B, 376-377, (2006).

[16] A Murayama, Sakuma, Appl. Phys. Lett., 88, 12, (2006).

[17] D. Hagele, M. Oestreich. Appl. Phys. Lett. 87, 091108 (2005).

[18] K Nomura, J Wunderlich, J Sinova, B Kaestner, AH MacDonald, T Jungwirth. Phys. Rev. B. 72, 24, (2005).

[19] X Jiang, R Wang, RM Shelby, RM Macfarlane, SR Bank, JS Harris, SSP Parkin. Phys. Rev. Lett., 94, 5, (2005).

[20] J Sinova, D Culcer, Q Niu, NA Sinitsyn, T Jungwirth, AH MacDonald. Phys. Rev. Lett., 92, 12, (2004).

[21] K Sato, PH Dederichs, H Katayama-Yoshida, J Kudrnovsky. Physyca. B, 340-342, (2003).

[22] ZH Xiong, ZV Vardeny, Jing Shi. Nature, 427, 6977, (2004).

[23] KC Hall, WH Lau,K Gundogdu, ME Flatte,TF Boggess. Appl. Phys. Lett., 83, 14, (2003).

[24] H Katayama-Yoshida, K Sato. Physica B, 327, (2003).

[25] F Matsukura, D Chiba, Y Ohno, T Dietl, H Ohno. Physica E, 16, (2003).

[26] I Zutic, J Fabian, S Das Sarma. Appl. Phy. Lett., 82, 2, (2003).

[27] A Tsukada, H Yamamoto, M Naito. Phys. Rev. B 74, 17, (2006).

[28] MH Jung, AM Alsmadi, S Chang, MR Fitzsimmons, Y Zhao, AH Lacerda, H Kawanaka, S El-Khatib, H Nakotte. J. Appl. Phys., 97, 10, (2005).

[29] C Autret, G Andre, F Bouree, C Martin, M Hervieu, A Maignan, R Retoux, B Raveau. Appl. Phys. A A74,(2002).

[30] VV Kharton, AA Yaremchenko, AL Shaula, MV Patrakeev, EN Naumovich, DI Logvinovich, JR Frade, FMB Marques. J.of Solid State Chem., 177, 1 (2004).

[31] H Taguchi. Solid State Sci., 9, 9, (2007).

[32] K. Takada, H. Sakurai, E. Takayama-Muromachi, F. Izumi, R. A. Dilanian, T. Sasaki, Nature 422 (2003) 53.

[33] Manuel Sánchez-Andújar, María Antonia Señarís-Rodríguez. Solid State Sciences 6 (2004) 21–27

[34] J. Matsuno,T, Y. Okimoto, Z. Fang, X.Z. Yu, Y. Matsui, N. Nagaosa, H. Kumigashira,M. Oshima, M. Kawasaki, Y. Tokura, Thin Solid Films 486 (2005) 113–116.

[35] G. Herzer, M. Vazquez, M. Knobel, A. Zhukov, T. Reininger, H.A. Davies,R. Grossinger, J.L. Sanchez L, Journal of Magnetism and Magnetic Materials 294 (2005) 252–266.

[36] C. Belouet, Appl. Surf. Sci., 96, 630 (1996).

[37] Ian W. Boyd and Wei Zhang, Appl. Surf. Sci. 127-139, 410 (1998).

[38] S. Jin, T.H. Tiefel, M. McCormack, R.A. Fastnacht, R. Ramesh and L. H Chen,, Science 264 (1994) 413.

[39] R. von Helmholt, J. Wecker, B. Holzapfel, L. Schultx, and K. Samwer, Phys. Rev. Lett. 71 (1993) 2331.

[40] W. Thomson, Proceedings of the Royal Society of London, **8**, pp. 546–550 (1856–1857).

[41] The Discovery of Giant Magnetoresistance, the Class for Physics of the Royal Swedish Academy of Sciences.

[42] G. Binasch, P. Grünberg, F. Saurenbach, and W. Zinn, Phys. Rev. B **39**, 4828 (1989).

[43] M.N. Baibich, J.M. Broto, A. Fert, F. Nguyen van Dau, F. Petroff, P. Eitenne, G. Creuzet, A. Friederich, and J. Chazelas, Phys. Rev. Lett. **61**, 2472 (1988).

[44] H. L. Ju, C. Kwon, R. L. Greene, and T. Venkatesan, Appl. Phys. Lett. **65**, 2108 (1994).

[45] G. Xiao, E. J. McNiff, Jr., G. Q. Gong, A. Gupta, C. L. Canedy, and J. Z. Sun, Phys. Rev. B 54, 6073 (1996).

[46] M. F. Hundley, M. Hawley, R. H. Heffner, Q. X. Jia, J. J. Neumeier, J. Tesmer, J. D. Thompson, and X. D. Wu, Appl. Phys. Lett. **67**, 860 (1995).

[47] A. J. Millis, P. B. Littlewood, and B. I. Shraiman, Phys. Rev. Lett. 74, 5144 (1995).

[48] A. J. Millis, B. I. Shraiman, and R. Mueller, Phys. Rev. Lett. **77**, 175 (1996).

[49] P. E. Schiffer, A. P. Ramirez, W. Bao, and S. W. Cheong, Phys. Rev. Lett. 75, 3336 (1995).

[50] M. R. Ibarra, J. M. De Terasa, B. Garcma-Landa, Z. Arnold, C. Marquina,

11 C. H. Booth, F. Bridges, G. J. Snyder, and T. H. Geballe, Phys. Rev. B 54, 15 606 (1996).

[51] J. M. D. Coey, J. Appl. Phys. 85, 5576 (1999).

[52] H. Y. Hwang, T. T. M. Palstra, S. W. Cheong, and B. Batlogg, Phys. Rev. B 52, 15 046 (1995).

[53] J. Mira, A. Fondado, L. E. Hueso, F. Rivadulla, and M. A. Lo¨pez Quintela, Phys. Rev. B 61, 5857 (2000).

[54] G. Zhao, K. Conder, H. Keller, and K. A. Mueller, Nature 380, 676 (1996).

[55] L. V. Panina and K. Mohri. Appl. Phys. Lett. 65 (1994) 1189.

[56] R. S. Beach and A. E. Berkowitx, ibid, 64 (1994) 3652.

[57] F.L. Machado, B.L. Da Silva, S.M. Rezende and C.S. Martins, J. Appl. Phys. 75

(1994) 6563.

[58] R. S. Beach and A. E. Berkowitx, ibid, 76 (1994) 6209.

[59] D. Atkinson and P.T. Squirb, J. Appl. Phys. 83 (1998) 6569.

[60] M. Knobel and K.R.Pirota, J. Magn. Magn. Mater. 242-245 (2002) 33.

[61] R. Valenzuela, M. Knobel, M. Vazquez and A. Hernando, J. Appl. Phys. 78 (1995) 5189.

[62] C.F. Majkrzak, J.W. Cable, J. Kwo, M. Hong, D.B. McWhan, Y. Yafet, and J.V. Waszczak, and C. Vettier, , Phys. Rev. Lett. 56, 2700 (1986).

[63] P. Grünberg, R. Schreiber, Y. Pang, M.B. Brodsky, and H. Sowers. Phys. Rev. Lett. 57, 2442 (1986).

[64] J.E. Ortega, F.J. Himpsel, G.J. Mankey and R.F. Willis, Phys. Rev. B 47, 1540 (1993).

[65] M.B. Salamon, S. Sinha, J.E. Cunningham, R.E. Erwin, J. Borchers, and C.P. Flynn, Phys. Rev. Lett. 56, 259 (1986).

[66] A. Heinrich, Z. Celinski, J.F. Cochran, W.B. Muir, J. Rudd, Q. M. Zhong, A.S. Arrott, K. Myrtle and J. Kirschner, Phys. Rev. Lett. 64, 673 (1990).

[67] S.S.P. Parkin, N. More and K.P. Roche, Phys. Rev. Lett. 64, 2304 (1990).

[68] S.S.P. Parkin, Phys. Rev. Lett. 67, 3598 (1991).

[69] B. Dieny, V.S. Speriosu, S.S.P. Parkin and B.A. Gurney, Phys. Rev. B 43, 1297 (1991).

[70] A. Chaiken, C.J. Gutierrez, J.J. Krebs and G.A. Prinz, J. Magn. Magn. Mat. 125, 228 (1993).

[71] D.E. Heim, R.E. Fontana, C. Tsang and V.S. Speriosu, IEEE Trans. on Magn. 30, 316 (1994).

[72] M. Julliere, Phys. Lett. A 54, 225 (1975).

[73] S. Maekawa and U. Gäfvert, Magn. Magn. 18, 707 (1982).

[74] J.S. Moodera, L.R. Kinder, T.M. Wong and R. Meservey, Phys. Rev. Lett. 74, 3273 (1995). 14.

[75] J. Moodera and G. Mathon, J. Magn. Magn. Mater., 200, 248 (1999).

[76] T. Miyazaki and N. Tezuka, J. Magn. Magn. Mat. 139, L231 (1995).

[77] S. Yuasa, A. Fukushima, T. Nagahama, K. Ando and Y. Suzuki, Jpn. J. Appl. Phys. 43, L588 (2004).

[78] S. Yuasa, T. Nagahama, A. Fukushima, Y. Suzuki, and K. Ando, Nature Materials 3, 868 (2004).

[79] S.S.P. Parkin, C. Kaiser, A. Panchula, P.M. Rice, B. Hughes, M. Samant, and S.-H. Yang, Nature Mat. 3, 862 (2004).

[80] N. F. Mott, J. Non-Cryst. Solids 1 (1968), 1.

[81] R. Jonathan, Friedman, Youzhu Zhang, Peihua Dai and M. P. Sarachik. Phys.Rev.B 53 (1996) 9528.

[82] A Hartstein and A B Fowler, J. Phys. C: Solid State Phys., Vol. 8, 1975.

[83] R. M. Rubinger, H. A. Albuquerque, R. L. da Silva, A. G. de Oliveira, G. M. Ribeiro, W. N. Rodrigues, C. P. L Rubinger, and M. V. B. Moreira Brazilian J. Phys., vol.

[84] 12 J.G. Bednorz, K.A. Müller, Z. Phys. B 64 (1986) 189.

[85] K K Singh, P Ganguly and Goodenough J B 1984 J. Solid State Chem. 52 254

[86] Buttrey D J, Honig J M and Rao C N R 1986 Mater. Res. Bull. 64 287

[87] Zhang Z, Greenblatt M and Goodenough J B 1994 J. Solid State Chem. 108 402

[88] F. Lichtenberg, Progress in Solid State Chemistry 30 (2002) 103

[89] H. K. Müller-Buschbaum, Journal of Alloys and Compounds 349 (2003) 49.

[90] D. Balz, K. Plieth, *Z.* Elektrochem. 59 (1955) 545.

[91] R. Scholder, D. Räde, Z. Anorg. Allg. Chem. 362 (1968) 149.

[92] Goodenough J B *1971 Progress in solid state chemistry,* H Reiss, ed. (Oxford: University Press) p. 145.

[93] L.O. Vasilechko, A.A. Fedorchuk, D.I. Savitskii, A.O. Matkovskii, S.B. Ubizskii*, Inorg. Mater*. USSR 31 (1995) 1128.

[94] J.E. Greedan, W. Gong, J. Alloys Comp. 180 (1992) 281.

[95] D. Grandjean, M.T. Weller*, Mater. Res. Bull.* 28 (1993) 685.

[96] H. Lou, Y.-P. Ge, P. Chen, M.H. Mei, F.T. Ma, G.L. Lu, *J. Mater. Chem.* 7 (1997) 2097.

[97] S.J. Skinner, J.A. Kilner, Solid State Ionics 135 (2000) 709.

[98] J.B. Smith, T. Norby, Journal of the Electrochemical Society 153 (2006) A233.

[99] E. Bohem, J.-M. Bassat, P. Dordor, F. Mauvy, J.-C. Grenier, Ph. Stevens, Solid State Ionics 176 (2005) 2717.

[100] B.C.H. Steele*, Solid State Ionics* 134 (2000) 3.

[101] C.N. Munnings , S.J. Skinner , G. Amow , P.S. Whitfield , I.J. Davidson, Solid State Ionics 176 (2005) 1895

[102] V.V. Kharton, A.A. Yaremchenko, E.N. Naumovich, Journal of Solid State Electrochemistry 3 (1999) 303.

[103] H. El Shinawi, C. Greaves, Journal of Solid State Chemistry 181 (2008) 2705, and references therein.

[104] X. Yang, L. Luo, H. Zhong, Applied Catalysis A: General 272 (1–2) (28 September 2004) 299–303.

[105] J.L. Soubeyroux, P. Courbin, D. Fournes, D. Fruchart, G. LeFlem, *J. Solid State Chem.* 31 (1980) 313.

[106] T. Omata, K. Ueda, N. Ueda, M. Katada, S. Fujitsu, T. Hashimoto, H. Kawazoe,

Solid State Commun. 88 (1993) 807.

[107] T. Omata, K. Ueda, H. Hosono, M. Katada, N. Ueda, H. Kawazoe, Phys. Rev. B 49 (1994) 10194.

[108] C. Autret, C. Martin, R. Retoux, A. Maignan, B. Raveau, G. André, F. Bourée, Z. Jirak, Journal of Magnetism and Magnetic Materials 284 (2004) 172.

[109] C. Bansal, H. Kawanak, H. Bando, A. Sasahara, R. Miyamoto, Y. Nishihara, Solid State Communications 128 (2003) 197.

[110] M. Imada, A. Fujimori, Y. Tokura, Rev. Mod. Phys. 70 (1998) 1039.

[111] J.M. Longo, P.H. Raccah, J. Solid State Chem. 6 (1973) 526.

[112] B. Grande, Hk. Müller-Buschbaum, M. Schweizer, Z. Anorg. Allg. Chem. 428 (1977) 120.

[113] Lichtenberg F. Dissertation, University of Zurich, 1991.

[114 Bouchard RJ, Gillson JL. *Mater. Res. Bull.* 7 (1972) 873.

[115] Allen PB, Berger H, Chauvet O, Forro L, Jarlborg T, Junod A, et al., *Phys. Rev. B* 53 (2001) 4393.

[116] Maeno Y, Hashimoto H, Yoshida K, Nishizaki S, Fujita T, Bednorz JG, et al. *Nature* 372(6506) (1994) 532.

[117] Mackenzie AP, Maeno Y. *Rev. Mod. Phys.* 75 (2003) 657.

[118] Maeno Y, Rice TM, Sigrist M. *Phys. Today* 54 (2001) 42.

[119] G. Cao, S. McCall, J.E. Crow, *Phys. Rev. B* 55 (1997) R672.

[120] S.I. Ikeda, Y. Maeno, *Physica B* 259-261 (1999) 947.

[121] K. Ishida, H. Mukuda, Y. Kitaoka, K. Asayama, Z.Q. Mao, Y. Mori, Y. Maeno, *Nature* 396 (1998) 6712.

[122] Z.Q. Mao, Y. Maeno, H. Fukasawa, *Mater. Res. Bull.* 35 (2000) 1813.

[123] A.P. Mackenzie, R.K.W. Haselwimmer, A.W. Tyler, G.G. Lonzarich, Y. Mori,

S. Nishizaki, Y. Maeno, *Phys. Rev. Lett.* 80 (1998) 151.

[124] K. Yamaura, D.P. Young, R.J. Cava, *Phys. Rev. B* 63 (2001) 064401.

[125] Y. Moritomo, A. Asamitsu, H. Kuwahara, Y. Tokura, *Nature* 380 (1996) 141.

[126] Tom Baikie, Zahara Ahmad, Madhavi Srinivasan, Antoine Maignan, Stevin S. Pramana, T.J. White, *Journal of Solid State Chemistry* 180 (2007) 1538

[127] H. Watanabe, T. Takeda, in: Y. Hashino, et al. (Eds.), *Ferrites: Proceedings of the International Conference, July 1970*, Tokyo University Press, Kyoto, Japan, 1971, p. 588.

[128] P. Bezdicka, A. Wattiaux, J.C. Grenier, M. Pouchard, P. Hagermuller, *Z. Anorg. Allg. Chem.* 619 (1993) 7.

[129] A. Nemudry, P. Rudolf, R. Schöllhorn, *Chem. Mater.* 8 (1996) 2232.

[130] R.L. Withers, M. James, D.J. Goossens, J. *Solid State Chem.* 174 (2003) 198.

[131] S.Y. Istomin, O.A. Drozhin, G. Svensson, E.V. Antipov, *Solid State Sci.* 6 (2004) 539.

[132] N.E. Trofinenko, J. Paulsen, H. Ullmann, R. Müller, *Solid State Ionics* 100 (1997) 183.

[133] M. James, K.S. Wallwork, R.L. Withers, D.J. Goossens, K.F. Wilson, J. Horval, X.L. Wang, M. Colella, *Mater. Res. Bull.* 40 (2005) 1415.

[134] S. Hébert, A. Maignan, V. Caignaert, V. Pralong, D. Pelloquin, B. Raveau, *Solid State Commun.* 134 (2005) 815.

[135] S.E. Dann, T.M. Weller, *J. Solid State Chem.* 115 (1995) 499.

[136] L. Viciu, H.W. Zandbergen, Q. Xu, Q. Huang, M. Lee, R.J. Cava, *J. Solid State Chem.* 179 (2006) 5010.

[137] J.M. Hill, B. Dabrowski, J.F. Mitchell, J.D. Jorgensen, *Phys. Rev. B* 74 (2006) 174417.

[138] D. Pelloquin, N. Barrier, A. Maignan, V. Caignaert, *Solid State Sci.* 7 (2005) 853.

[139] A. Demont, S. Hébert, D. Pelloquin, A. Maignan, *Journal of Solid State Chemistry* 181 (2008) 1314

[140] X. L. Wang, H. Sakurai and E. Takayama-Muromachi, J. Appl. Phys. 97, 10M519 (2005).

[141] Hideki Taguchi., Solid State Sciences 9 (2007) 869 – 873.

[142] Y.Y. Liu, X.M. Chen, X.Q. Liu, Solid State Communications 136 (2005) 576–579.

[143] Xu M, Balamurugan S, Takayama-Muromachi E. Progress of Theoretical Physics Supplement, no.159, 2005, pp. 349-54.

[144] F. Riza, Ch. Ftikos, J. European Ceramic Society 27 (2007) 571–573.

[145] C.S. Hong, E.O. Chi, W.S. Kim, N.H. Hur, K.W. Lee, C.H. Lee, Chem. Mater. 13 (2001) 945.

[146] J.C. Bouloux, J.L. Soubeyroux, A. Daoudi, G. le Flem, Mater. Res. Bull. 16 (1981) 855.

[147] K. Sander, U. Lehmann, H. Mueller-Buschbaum, Z. Anorg. Allg. Chem. 480 (1981) 153.

[148] X.L. Chen, J.K. Liang, C. Wang, G.G. Rao, X..R. Xing, Z.H. Song, Z.Y. Qiao, J. Alloys Comp. 205 (1994) 101.

[149] Y. Takeda, R. Kanno, M. Sakano, O. Yamamoto, M. Takano, Y. Bando, H. Akinaga, K. Takita, J.B. Goodenough, Mater. Res. Bull. 25 (1990) 293.

[150] K. Sreedhar, C.N. Rao, Mater. Res. Bull. 25 (1990) 1235.

[06] B.W. Arbuckle, K.V. Ramanujachary, Z. Zhang, M. Greenblatt, J. Solid State Chem. 88 (1990) 278.

[151] Y. Takeda, M. Nishijima, N. Imanishi, R. Kanno, O. Yamamoto, M. Takano, J. Solid State Chem. 96 (1992) 72.

[152] K.K. Singh, P. Ganguly, J.B. Goodenough, J. Solid State Chem. 52 (1984) 254.

[153] A. Demourgues, A. Wattiaux, J.C. Grenier, M. Pouchard, J.L. Soubeyroux, J.M. Dance, P. Hagenmuller, J. Solid State Chem. 105 (1993) 458.

[154] M. James, J.P. Attfield, J. Rodriguez-Carvajal, Chem. Mater. 7 (1995) 1448.

[155] M. James, J.P. Attfield, Chem. Mater. 7 (1995) 2338.

[156] Y. Moritomo, K. Higashi, K. Matsuda, and A. Nakamura, Phys. Rev. B 55, R14725 (1997).

[157] C.N. Rao, P. Ganguly, K.K. Singh, R.A. Mohan Ram, J. Solid State Chem. 72 (1988) 14.

[158] G. Demazeau, P. Courbin, G. le Flem, M. Pouchard, P. Hagenmuller, J.L. Soubeyroux, I.G. Main, G.A. Robins, Nouveau J. Chim. 3 (1979) 171.

[159] T. Matsuura, J. Tabuchi, J. Mizusaki, S. Yamauchi, K. Fueki, J. Phys. Chem. Solids 49 (1988) 1403.

[160] J. Wang, Y.C. Tao, W. Zhang, D.Y. Xing, J. Phys.: Condens. Matter 12 (2000) 7425.

[161] D. Grandjean, M.T. Weller, Mater. Res. Bull. 28 (1993) 685.